High-pressure pool-boiling heat transfer enhancement and mechanism on engineered surfaces

By

Smreeti Dahariya

B.S. National Institute of Technology, Raipur, INDIA, 2007
M.Tech. Indian Institute of Technology, Kanpur, INDIA, 2010

AN ABSTRACT OF A DISSERTATION

Submitted in partial fulfillment of the requirements for the degree

DOCTOR OF PHILOSOPHY

Alan Levin Department of Mechanical and Nuclear Engineering
Carl R. Ice, College of Engineering

KANSAS STATE UNIVERSITY
Manhattan, Kansas

2020

Abstract

Boiling has received considerable attention in the technology advancement of electronics cooling for high-performance computing applications. Two-phase cooling has an advantage over a single-phase cooling in the high heat removal rate with a small thermal gradient due to the latent heat of vaporization. Many surface modifications have been done in the past including surface roughness, mixed wettability and, porous wick copper play a crucial role in the liquid-vapor phase change heat transfer. However, the mechanisms of high-pressure pool-boiling heat transfer enhancement due to surface modifications has not been well studied or understood. The properties of water, such as the latent heat of vaporization, surface tension, the difference in specific volume of liquid and vapor, decrease at high-pressure. High-pressure pool-boiling heat transfer enhancement is studied fundamentally on various engineered surfaces. The boiling tests are performed at a maximum pressure of 90 psig (620.5 kPa) and then compared to results at 0 psig (0 kPa). The results indicate that the pressure influences the boiling performance through changes in bubble dynamics. The bubble departure diameter, bubble departure frequency, and the active nucleation sites change with pressure.

The pool-boiling heat transfer enhancement of a Teflon© coated surface is also experimentally tested, using water as the working fluid. The boiling results are compared with a plain surface at two different pressures, 30 and 45 psig. The maximum heat transfer enhancement is found at low heat flux at high pressures. The primary reasons for the HTC enhancement at low heat flux are increased active nucleation sites at low wall superheat and decreased bubble departure size. A significant reduction in the wall superheat is also observed. The results suggest that Teflon© coated surface promotes nucleation because of the lower energy requirement.

The boiling results are also obtained for wick surfaces. The wick surfaces are fabricated using a sintering process. The boiling results are compared with a plain surface. The reasons for enhancements during pool-boiling heat transfer are primarily due to increased bubble generation, higher bubble release frequency, reduced thermal-hydraulic length modulation, and enhanced thermal conductivity due to the sintered wick layer. The analysis suggests that the Rayleigh-critical wavelength decreases by 4.67 % of varying pressure, which may cause the bubble pinning between the gaps of sintered particles and avoids the bubble coalescence. Changes in the pitch distance indicate that a liquid-vapor phase separation happens at the solid/liquid interface, which impacts the heat-transfer performance significantly.

Similarly, the role of the high-pressure over the wicking layer is further analyzed and studied. It is found that the critical flow length, λ_u reduces by three times with 200 μm particles. The results suggest that the porous wick layer provides a capillary-assist to liquid flow effect, and delays a surface dry out. The surface modification and the pressure amplify the boiling heat transfer performance. All these reasons may contribute to the CHF, and HTC enhancement in the wicking layer at high-pressure.

High-pressure pool-boiling heat transfer enhancement and mechanism on engineered surfaces

by

Smreeti Dahariya

B.S. National Institute of Technology, Raipur, INDIA, 2007
M.Tech. Indian Institute of Technology, Kanpur, INDIA, 2010

A DISSERTATION

submitted in partial fulfillment of the requirements for the degree

DOCTOR OF PHILOSOPHY

Alan Levin Department of Mechanical and Nuclear Engineering
Carl R. Ice, College of Engineering

KANSAS STATE UNIVERSITY
Manhattan, Kansas

2020

Approved by:

Major Professor
Dr. Amy Rachel Betz

Copyright

Abstract

Boiling has received considerable attention in the technology advancement of electronics cooling for high-performance computing applications. Two-phase cooling has an advantage over a single-phase cooling in the high heat removal rate with a small thermal gradient due to the latent heat of vaporization. Many surface modifications have been done in the past including surface roughness, mixed wettability and, porous wick copper play a crucial role in the liquid-vapor phase change heat transfer. However, the mechanisms of high-pressure pool-boiling heat transfer enhancement due to surface modifications has not been well studied or understood. The properties of water, such as the latent heat of vaporization, surface tension, the difference in specific volume of liquid and vapor, decrease at high-pressure. High-pressure pool-boiling heat transfer enhancement is studied fundamentally on various engineered surfaces. The boiling tests are performed at a maximum pressure of 90 psig (620.5 kPa) and then compared to results at 0 psig (0 kPa). The results indicate that the pressure influences the boiling performance through changes in bubble dynamics. The bubble departure diameter, bubble departure frequency, and the active nucleation sites change with pressure.

The pool-boiling heat transfer enhancement of a Teflon© coated surface is also experimentally tested, using water as the working fluid. The boiling results are compared with a plain surface at two different pressures, 30 and 45 psig. The maximum heat transfer enhancement is found at the low heat fluxes. At high heat fluxes, a negligible effect is observed in HTC. The primary reasons for the HTC enhancement at low heat fluxes are active nucleation sites at low wall superheat and bubble departure size. The Teflon© coated surface promotes nucleation because of the lower surface energy requirement.

The boiling results are also obtained for wick surfaces. The wick surfaces are fabricated using a sintering process. The boiling results are compared with a plain surface. The reasons for enhancements in the pool-boiling performance are primarily due to increased bubble generation, higher bubble release frequency, reduced thermal-hydraulic length modulation, and enhanced thermal conductivity due to the sintered wick layer. The analysis suggests that the Rayleigh-critical wavelength decreases by 4.67 % of varying pressure, which may cause the bubble pinning between the gaps of sintered particles and avoids the bubble coalescence. Changes in the pitch distance indicate that a liquid-vapor phase separation happens at the solid/liquid interface, which impacts the heat-transfer performance significantly.

Similarly, the role of the high-pressure over the wicking layer is further analyzed and studied. It is found that the critical flow length, λ_u reduces by three times with 200 μm particles. The results suggest that the porous wick layer provides a capillary-assist to liquid flow effect, and delays the surface dry out. The surface modification and the pressure amplify the boiling heat transfer performance. All these reasons may contribute to the CHF, and HTC enhancement in the wicking layer at high-pressure.

Table of Contents

List of Figures

List of Tables

Abbreviations

Greek Symbols:

α	thermal diffusivity of liquid
ε	porosity
δ	boundary layer thickness
η	nucleation site density
λ	wave length
μ	viscosity
ρ	density
Ø	contact angle
σ	surface tension
θ	superheat

Subscripts:

br	breakthrough
c	capillary
cu	copper
d	departure
max	maximum
min	minimum
l	liquid
l_v	liquid/vapor
RT	Rayleigh -Taylor
s	surface
sat	saturation
sf	wall/fluid
tef	teflon
tot	total
u	uniform
v	vapor phase
w	wall

Nomenclatures

a	particle size	m
A	total surface area	m^2
a_i	measured parameter	constant
Ac	capillary area	m^2
c_{pl}	specific heat of the liquid	J/kg K
C_{sf}	surface fluid combination	constant
CHF	Critical Heat Flux	W/cm^2
C_1, C_2, C_3	coefficients	constants
d_{br}	breakthrough bubble diameter	m
d_p	particle diameter	m
D_d	departure diameter	m
D_s	maximum cavity diameter	m
ΔP	pressure drop	Pa
ΔT	temperature difference	K
$\eta_a{}'$	active nucleation site density	(# units)/m^2
f	bubble departure frequency	1/sec
g	gravity	m/sec^2
h_{lv}	latent heat of vaporization	J/kg
HTC	heat Transfer Coefficient	W/cm^2 K
k	conductivity	W/mK
κ	permeability	constant
L	thickness	m
L_m	capillary length	m
λ_{RT}	rayleigh-taylor wavelength	m
λ_u	wavelength for the uniform porous coating	m
$\dot{m}$	mass flow rate	kg/sec
μ_l	fluid viscosity	N. sec/m^2
P	parameter	constant
P_c	capillary pressure	Pa
Pr_l	Prandtl number	constant

r_c	critical radius	m
ρ_l	density of liquid	kg/m^3
ρ_v	density of vapor	kg/m^3
T_s	surface temperature	K
T_{sat}	saturation temperature	K
T_j	junction temperature	K
ΔT	degree of wall superheat	K
U	Uncertainty	constant
v	velocity	m/sec
q''	heat flux	W/cm^2
q_o	required heat flux	W/cm^2
x	distance	m

Acknowledgement

I would like to express my special thanks and gratitude to my adviser, Dr. Amy Rachel Betz, who gave me an opportunity to work in her lab and had trust in my potential and skills. I would like to acknowledge her for her continuous guidance in writing journal articles and conference papers, providing multiple opportunities for presenting work in the conference at national and international level in various scientific societies, and for her constant help in my research work. I want to show my deepest gratitude to her for mentoring me personally and professionally. I would also want to thank and acknowledge my committee members, Dr. David Poole, Dr. Steven Eckels, Dr. Gurpreet Singh, and Dr. Ryan Hansen for their guidance and insight into my research work. I would also like to show my sincere gratitude to Dr. Hwang and his research team at Wichita State University with the entire NASA project team for their constant inputs in my research work. I want to thank Dr. Derby also for her continuous support and guidance in my course and Ph.D research work. I would also want to thank my senior Dr. Li, who graduated in 2017 from the lab, for teaching me the experimental setup. I want to thank the undergrads Nill Patel and Brady Brooks for assisting me in performing experiments and proofreading the journal articles. I want to thank my lab mates Emily Stallbaumer and Jordan Morrow for being in the lab during the last stage of my Ph.D research work. I would also want to acknowledge Eric Wagner and his team for allowing me to the machine shop at Kansas State University.

My sincere gratitude is for my parents and siblings for their constant support and bearing my frustration and fears through my journey. Thank you so much for being with me. Working in a foreign land was not only difficult but it was extremely challenging for me to excel.

The work is supported by the NASA Cooperative Agreement Notice, Grant Number 80NSSC18M0030, the United States of America.

Dedication

It is my deepest gratitude and warmest affection that I dedicate this work to my parents for their trust and constant belief in me. Without their love, care and blessings, I would never have achieved this much.

Chapter 1 - Introduction

1.1 Background and Motivation

Over the next 25 years, a dramatic shift in energy demand is expected, roughly increasing from 110 to 160 qBtu of energy [1]. The increasing degree of interconnectivity, continuing growth in data volume via personal electronic devices, advancing of embedded electronics system in transportation systems, and extensive usage of electricity by large scale data center systems have played a significant role in this energy demand shift [2]. The software companies such as Amazon, Microsoft, Google, Facebook and other companies are looking for passive cooling solutions to cool the processors and to reduce the electricity usage in large data centers.

Economical, reliable, and safe access to outer space is crucial to extend human presence in space and explore in-space resources [3]. Achieving this goal requires novel spacecraft technologies, including the next-generation thermal and water management systems for efficient and lightweight spacecraft and habitats [4, 5]. Novel spacecraft technologies require advanced passive cooling to transfer a large amount of heat in a small thermal resistance. The performance of the liquid-vapor phase-change heat transfer is limited due to a requirement of a robust and additional flow control system, which makes the system bulky, complicated, and increases the cost of spacecraft. Several techniques have been developed for cooling solutions, including heat sinks, cold plates, thermoelectric coolers, fans and blowers, heat pipes, vapor chambers, thermosiphons, and others. These cooling solutions can be categorized broadly in two areas: air cooling and liquid cooling. Liquid cooling can be further categorized into two areas: a single-phase and a two-phase cooling system are shown in Fig 1.1.

In electronic systems, an air-cooling system comprises a heat sink and a mechanical rotating device fan. The heat sink dissipates heat from the electronic system passively by a fluid medium using a series of fans. An air-cooled system provides the most reliable, simpler, and affordable cooling solution. However, an air cooling system makes the electronic system bulky, noisy, and less efficient. It also provides limited cooling because of the low specific heat of air. For extensive computing infrastructure like data centers, an air cooled system also requires a significant amount of power input for the air conditioning system.

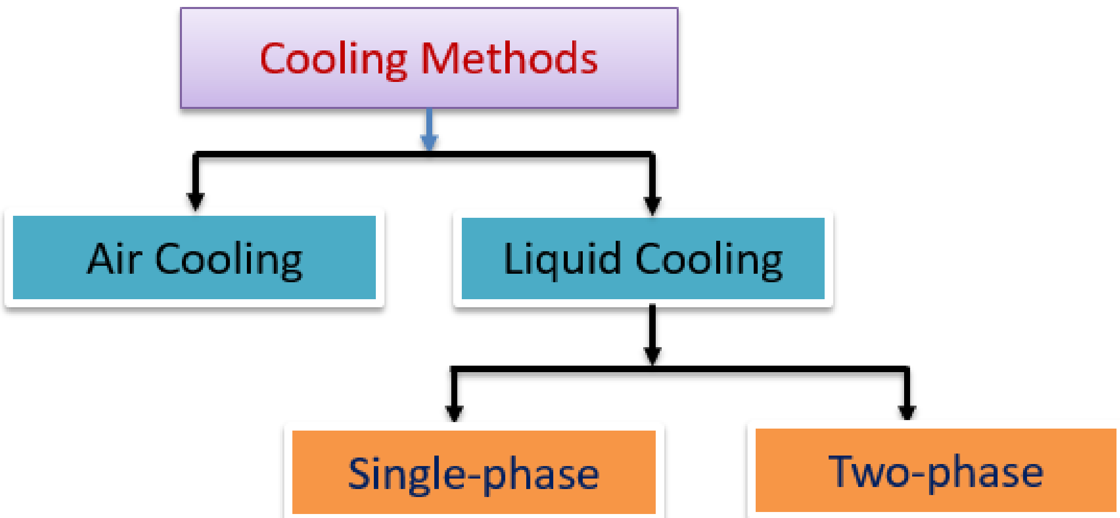

Figure 1.1 The most common electronic cooling methods

Liquid cooling has received significant interest in the new generation of electronic cooling systems over the last three decades. Heat can be removed using a single-phase liquid in microchannels [6]. A two-phase cooled system has an advantage in the high heat removal rate as compared to a single-phase cooled system due to the latent heat of vaporization. It can dissipate heat three times higher in comparison to air cooling. However, liquid cooling has several limitations in real-life applications. It requires a closed-loop system for heat dissipation. It also has the potential for coolant leaking.

Such cooling methods can be used in a wide range of applications, including miniature electronic cooling [7], renewable energy systems [8], electric vehicles [9][10], high power radars [11], and immersion cooling [12][13] for high performance of computing systems (HPC), etc. A two-phase cooling, i.e., pool-boiling, offers a passive heat flux cooling with a minimal temperature gradient. However, the main technical challenges are limited to the heat removal capacity due to the Critical Heat Flux (CHF) which is a transition to a low Heat Transfer Coefficient (HTC) due to surface dry out. In the past, many methods have been employed for boiling heat transfer enhancement, including surface modification, varying system pressure, and providing capillary driven flow using various wick structures which are discussed in the next sections.

1.2 Literature Survey

1.2.1 Enhancement with surface modifications

In pool-boiling heat transfer, bubble generation plays a crucial role in the heat transfer enhancement. Several approaches can enhance the performance of pool-boiling heat transfer either by modifying the surface morphology [14] or altering the properties of the working fluid by addition of nano-particles [15] [16]. The boiling heat transfer can be enhanced by varying the system pressure [17]. All these methods enhance the heat transfer performance passively and can be applied to single-phase or two-phase boiling heat transfer. These techniques promote higher bubble generation decreasing the thermal resistance of a heated surface with or without increasing surface area [15]. Today, there is a high demand for advanced thermal management to enhance the performance of overall systems [18]. The application of passive techniques in boiling heat transfer is of great interest because it offers a reliable and material savings solution with an advanced thermal control and compactness feature [19]. Many approaches have been shown effective heat transfer enhancement to pool-boiling heat transfer passively [20].

The surface engineering can be varied by introducing changes in the surface at micro and nanoscales. Surface engineering approaches include surface roughness [21-22], micro/nano structured surfaces [23-25], wettability [26-32], addition of nanoparticles [33], nanocoating [34], modulated wick surfaces [35] and micro porous surfaces [36], extended surfaces like pin-finned [37], swirl flow devices etc. Jones et.al [22] investigated the influence of surface roughness on the performance of nucleate pool-boiling heat transfer. They found 210% enhancement in the heat transfer coefficient for FC-77 (Fluorinert™ coolant) with a rough surface (surface roughness between 1.08 μm to 10 μm) compared to the polished surface with a surface range between 0.027

μm to 0.038 μm. The importance of using rough surfaces in the performance of boiling heat transfer lies in the increased number of nucleation sites and the size of cavities.

Honda and Wei [37] performed a series of pool-boiling experiments for the micro-pin-fin of 10-50 μm in thickness and 60-200 μm in height for cooling electronic components. The surface was fabricated by dry etching. They found a sharp increase in the slope of boiling curve with an enhancement for the CHF and the HTC. The maximum value of allowable heat flux was reported to be 84.5W/cm^2, which is 4.2 times larger compared to the smooth chip with a chip dimension h = 270 μm and t = 50 μm at ΔT_{sub} = 45 K.

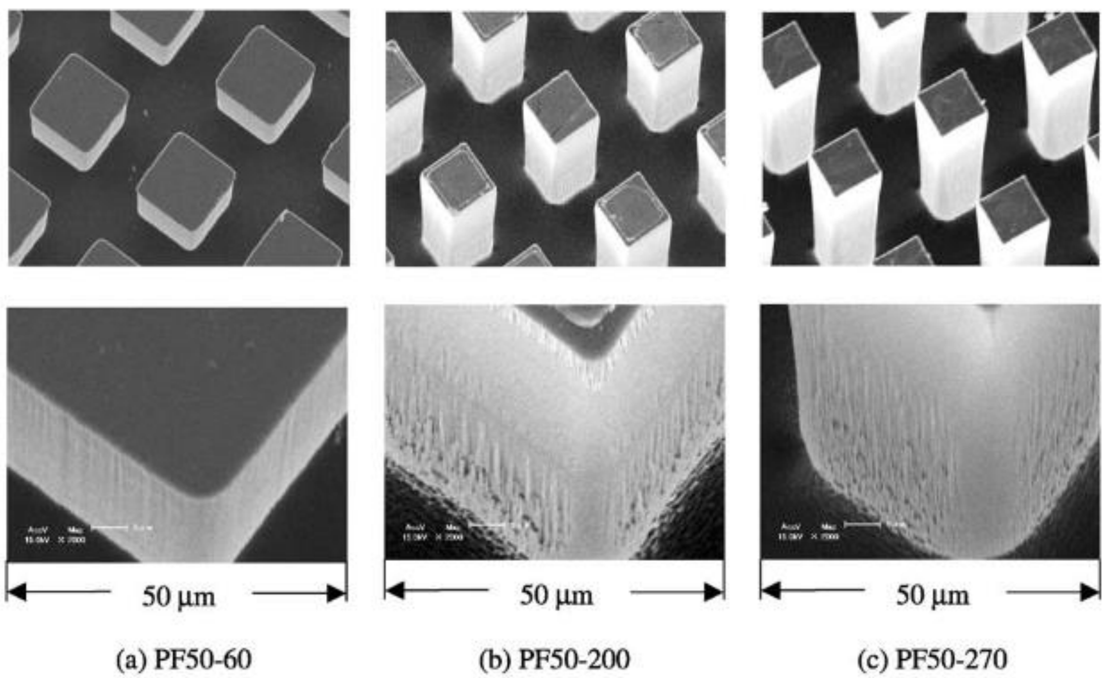

Figure 1.2 SEM image of fabricated silicon chips with micro pin fins [37]

On the other hand, Rahman et al [38], achieved a CHF of 257 W/cm^2 for water on the fabricated micro structured superhydrophilic surfaces with negligible contact angles. The research work demonstrated the role of wickabililty as the main factor in the CHF enhancement. The usage of biotemplated nanofabrication was featured with the *Tobacco mosaic virus* by varying length scales, morphologies, roughness factors, and wickabilities. A CHF model was also correlated to a dimensionless parameter for capillary action. The SEM images of microstructure geometries are shown in Fig 1.3.

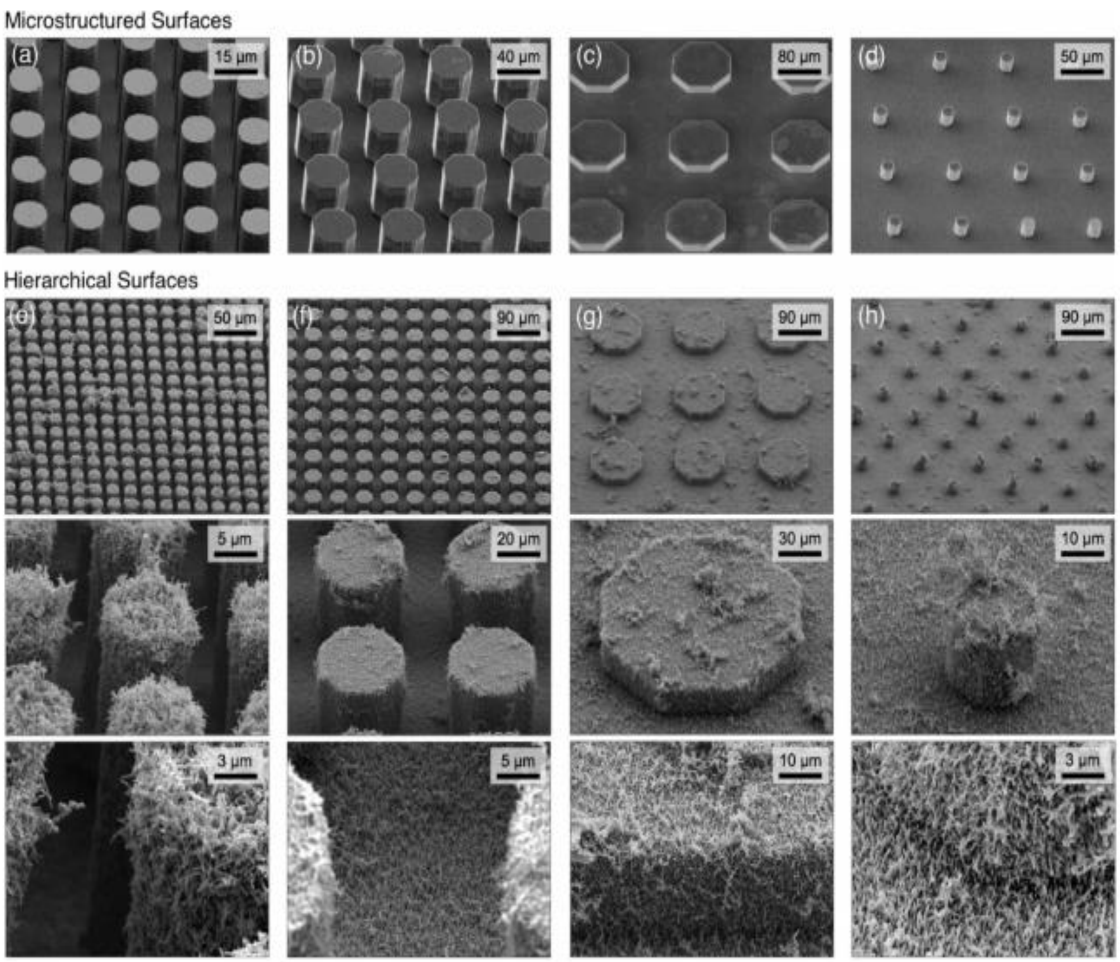

Figure 1.3 SEM images of micro, nano, and hierarchically structured silicon surfaces, and TMV coated micro/nano structures. All the geometries were fabricated using deep reactive ion etching. The image is taken from the reference [38]

Betz et.al [28] investigated and achieved 165% and 200% of enhancement in the CHF and the HTC respectively for the enhanced biphilic surfaces (combined hydrophilic and hydrophobic patterns). The surfaces were characterized with different networks of combined hydrophilic and hydrophobic regions. Varied wettability surface featured with hydrophilic surface over the hydrophobic surface gives an advantage in transporting liquid to the heated surface and the hydrophobic surface promotes bubble nucleation at lower wall superheat. A micrograph on hydrophilic and hydrophobic network is shown in Fig 1.4. The onset nucleate boiling at the onset point is also shown in Fig.1.4

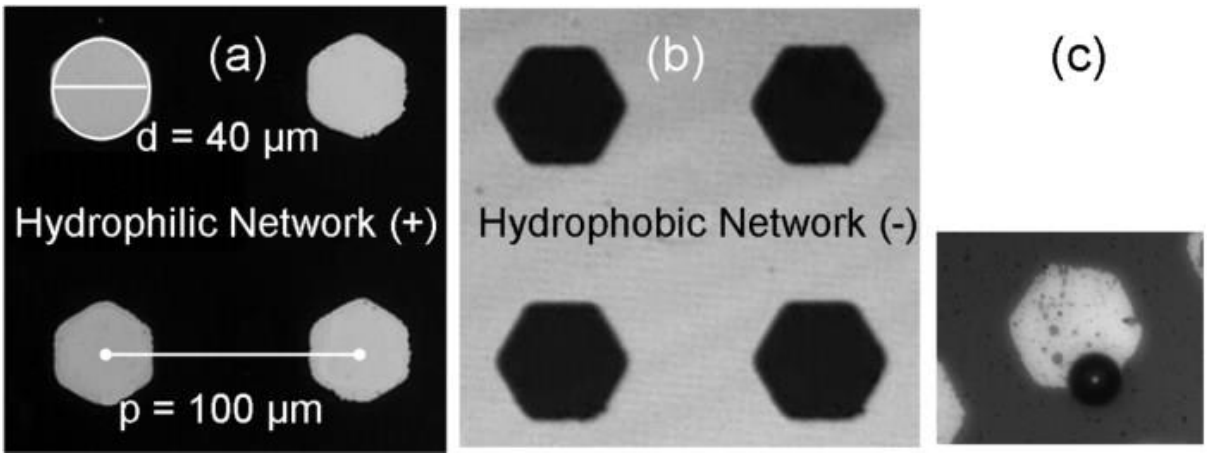

Figure 1.4 Topography of (a) hydrophilic and (b) hydrophobic surfaces with the patterned diameter d and the pitch length p (c) nucleating bubble at the interface area of different wettability [28].

Li and Betz [39], investigated pool-boiling heat transfer on the graphene oxide coated surface at high-pressures. The surface was fabricated using a spray coating method. The result showed a significant improvement in the HTC at high-pressure. The HTC was enhanced by a 126.8 % at 0 psig and 51.5 % at 45 psig for a heat flux of 30 W/cm^2. In regards to bubble dynamics, the bubble departure size at the graphene oxide surface was significantly smaller than the copper surface. The HTC enhancement was related to the bubble departure size due to a pinning mechanism on the micro and nanostructures in the graphene oxide coating surface and a higher thermal conductivity. The topography of the graphene coated surface is shown in Fig.1.5. The top and side view of the coated surface are shown in Fig 1.5.

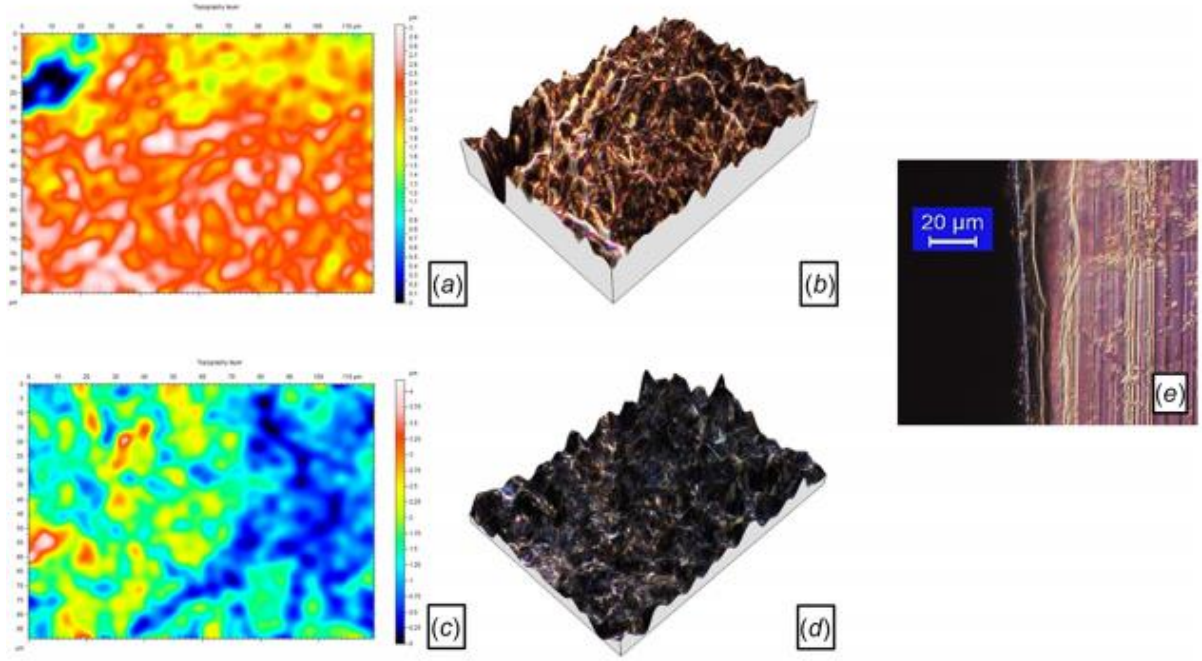

Figure 1.5 The SEM image of (a) the plain copper surface and (c) the GO coated surface. The 3D images are shown for (b) the plain copper and (d) the GO coated surface. The side view of the coated GO coated surface is shown in (e).

1.2.2 Enhancement with varying system pressure

In the literature, many experimental results have reported heat transfer enhancement with pressure. Sakashita et.al [17] studied the boiling behavior on a horizontal plate in saturated pool-boiling of water at high-pressures (up to 701 kPa). The effect of pressure was found on the s bubble departure size, but the bubble departure frequency of the coalesced bubbles showed negligible effect. A direct correlation was also highlighted for the nucleation site densities with the pressure [40]. A significant enhancement in the performance of low pressure pool-boiling has also been reported [41-44]. The summary of high-pressure pool-boiling data is tabulated in Table 1-1.

There is not enough data to explain the complexity involved in the high-pressure pool-boiling heat transfer [17]. There is a considerable need for experimental data to understand the physics involved in the high-pressure pool-boiling.

Table 1-1 Summary of high-pressure pool-boiling heat transfer

Authors	Pressure Range	Fluid	Surface	Remark
Sakashita and Ono 2009, [17]	atm. to 7 MPa	Water	Horizontal upward	Primary bubble size decreases, no change in the bubble departure frequency
Semeria, 1963 [45]	5 MPa to 10 MPa	Water	Horizontal cylinder	Size of departure diameter is inversely proportional to the pressure
Bobrovich and Mamontva, 1965 [46]	0.1 MPa to 5.35 MPa	Water	Upward facing rectangular surface	
Nisikawa et al., 1982 [47]	0.005 to 4 MPa	Water	Horizontal 0.3mm diameter wire	

1.2.3 Enhancement using wick structure

In pool-boiling heat transfer, the main challenges lie to a limited heat removal capacity due to a low Critical Heat Flux (CHF), because of premature surface dry out and poor Heat Transfer Coefficient (HTC) due to a premature surface dry out. To overcome these limitations, the application of a uniform thickness porous-layer coating to the surface, have been shown to passively provide effective heat transfer enhancement to boiling heat transfer [48][49]. Nasersharifi et.al [50] investigated saturated pool-boiling heat transfer performance on multilevel modulated wicks, i.e, monolayer, columnar, and mushroom post wicks structure. The schematic of the monolayer, columnar and mushroom post wicks structures are shown in Fig.1.6. They found 20% and 87% enhancement in the critical heat flux in monolayer wicks without and with the mushroom post structure, compared to the plain surface for n-pentane. The CHF enhancement of the mushroom wicks attributed to its pitch distance, 3.5 mm, which effectively reduce the hydrodynamic instability (Rayleigh-Taylor) wavelength. Further reduction of the pitch distance, 1 mm, and a 250% enhancement for CHF was found.

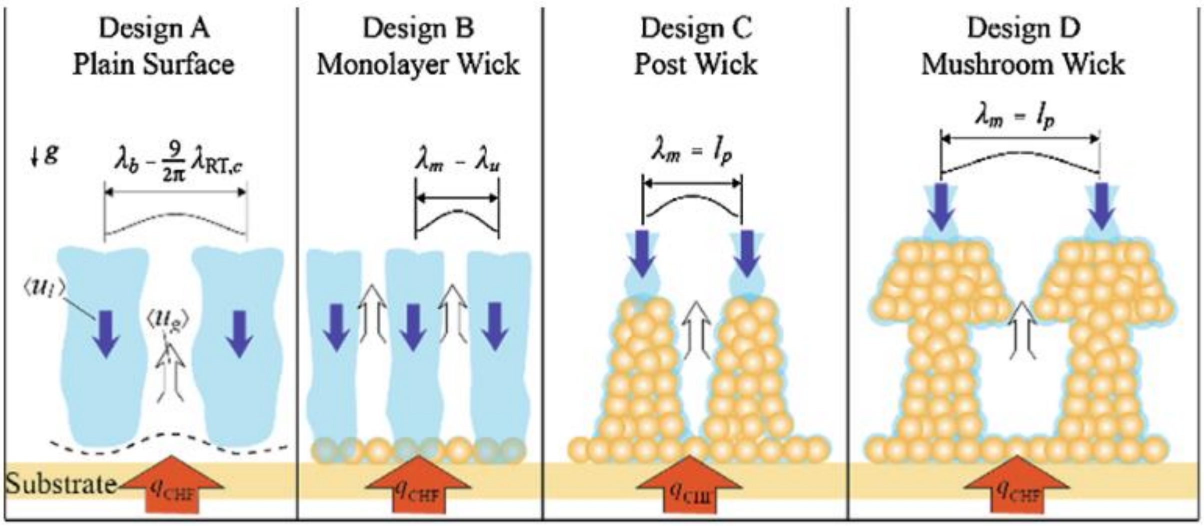

Figure 1.6 The schematic of multilevel modulate wick in pool-boiling including the plain surface (Design A), monolayer (Design B), columnar posts (Design C), and mushroom posts (Design D) wicks. The image is taken from reference [50].

Hwang and Kaviany [51] studied pool-boiling performance on thin uniform porous coatings for different copper particles diameters from 40 microns to 80 microns with coating thickness varying between 3 and 5 particles diameter. They found that a thin uniform coating significantly influences the hydrodynamic instabilities by decreasing the critical Rayleigh-Taylor wavelength. Jafari et.al [52] studied the performance of a two-phase heat transfer process on a free foam porous structure fabricated by 3D metal printing technology. They examined the capillary performance of 3D printed wick structures with the sintered powder, screen mesh, and composite wick structures. Kandilkar [53] emphasized the dominating effect of evaporation momentum force in the pool-boiling performance for microstructure surfaces through the bubble dynamics of nucleating bubbles. Chang and You [54] reported the enhancement in both the CHF and HTC of the microporous coating and found that the enhancements are due to the increased nucleation site density. Kim et. al [55] found that the microporous coating augments nucleate boiling performance through increased latent heat transfer in the low heat flux region and through increased convection heat transfer in the high heat flux region.

Table 1-2 Summary of the predicted critical heat flux correlations of plain and micro structured surfaces during pool-boiling

Type of Surfaces	Predicted Correlations
Plain Surface (Zuber, 1959) [56]	$q_{CHF,Z} = \frac{\Pi}{24} h_{lg} {\rho_g}^{1/2} \left[g\sigma(\rho_l - \rho_g\right]^{1/4}$
Bi-porous sintered coatings (Byon et.al, 2013) [57]	$q_{CHF} = C_b q_{CHF,Z}$ $C_b = 1.84 + 1.75 \left(\frac{d}{D}\right)^{-1} exp \left[-4.51 \left\{1.71 + ln\left(\frac{d}{D}\right)\right\}^2\right]$
Modulated Porous Layer (Liter and Kaviany, 2001) [58]	$q_{CHF} = \Delta h_{lg} \left(\frac{2\Pi^3 a^3 \sigma \rho_g}{9\lambda_{RT}}\right)^{1/2}$ $\lambda_{RT} = 9\left[\frac{\sigma}{g(\rho_l - \rho_g)}\right]^{1/2}$
Uniform porous layer coating (Polezhaev and Kovalev, 1990) [59]	$q_{CHF,u} = 0.52\varepsilon^{2.28} \boldsymbol{\Delta} h_{lg} \left[\frac{2\sigma\rho_l\rho_g}{(\rho_l + \rho_g)\, d_{br})}\right]^{1/2}$ where d_{br} is the diameter of the breakthrough bubble

Liter and Kaviany [58] investigated the modulated porous-layer coatings and found an enhancement in the pool-boiling critical flux nearly three times over that of a plain surface. They demonstrated the two independent mechanisms in a critical heat flux delay: decreased modulation wavelength and the capillary pumping force. Byon et.al [57] investigated the pool-boiling critical heat flux of bi-porous sintered copper coatings in FC-72 and found the enhancement is primarily a function of the particle size to cluster size ratio (d/D) and independent of the coating thickness. Many correlations have been developed for the CHF of micro-structured surfaces. A summary of the predicted correlations is shown in Table 1-2.

1.3 Pool-Boiling Heat Transfer Theory

Pool-boiling heat transfer is an efficient way to transfer a large amount of heat in a small thermal gradient because of high latent heat of vaporization. It is a complex, two-phase, and transient heat transfer mechanism. It transfers heat through vapor bubbles from a heated surface in a superheated liquid layer. A complete boiling process is generally described through a boiling curve. A typical boiling curve for pool-boiling heat transfer is shown in Fig 1.7. It is basically drawn for the rate of heat transfer versus degree of superheat. The rate of heat transferred through a unit area of a heated surface is determined using Fourier's law of heat conduction. The wall of superheat can be determined as the temperature difference between the surface temperature T_s and the saturated bulk fluid temperature T_{sat}.

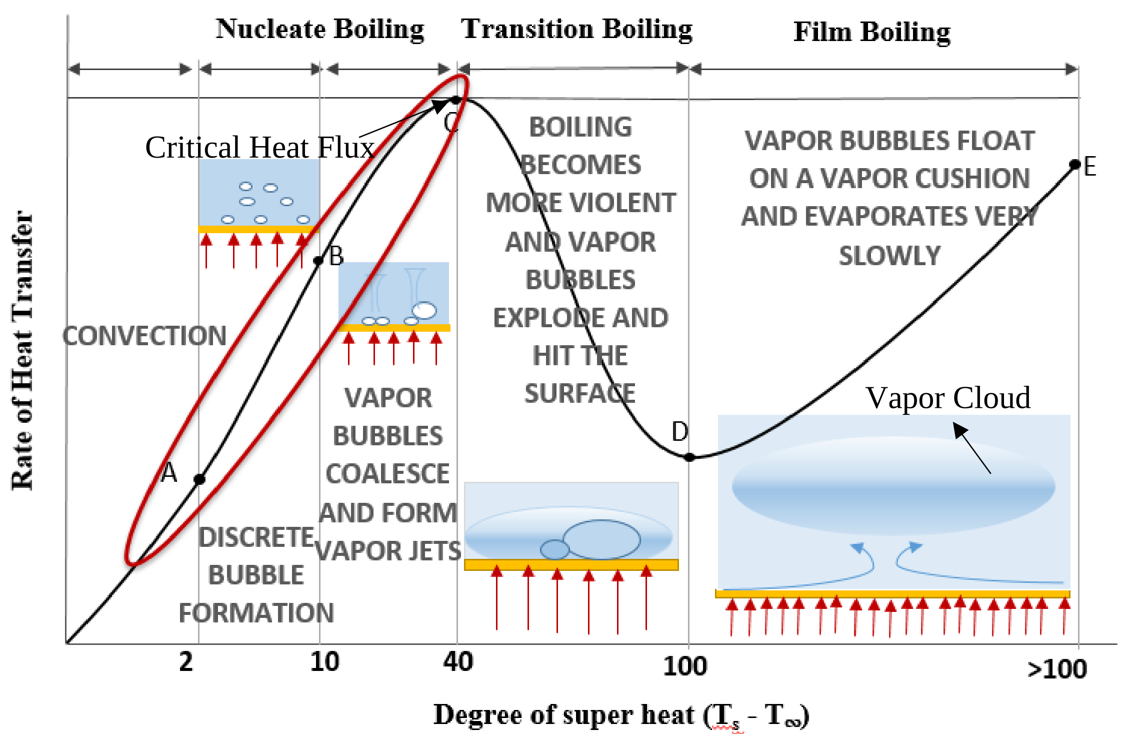

Figure 1.7 A typical boiling curve for pool-boiling heat transfer. C indicates the Critical Heat Flux (CHF)

A typical pool-boiling curve consists of four different boiling regimes based on the wall superheat i.e $\Delta T = T - T_{sat}$.

1. **Regime O-A**: Natural convection boiling - $\Delta T < 5°C$
2. **Regime A-B**: Discrete vapor bubble formation - $5°C < \Delta T < 10°C$
3. **Regime B-C**: Nucleate boiling - $10°C < \Delta T < 30°C$
4. **Regime CD**: Transition boiling - $30°C < \Delta T < 200°C$
5. **Regime D-E**: Film boiling - $200°C < \Delta T <$ beyond

These boiling regimes are shown in the boiling curve in Fig 1.7. A pool-boiling process starts at an onset point when the first bubble nucleates to the surface. When the wall superheat increases to 10°C, the heat is transferred through a number of small bubbles through the surface followed by a large number of vapor bubbles formation so called nucleate boiling. In pool-boiling heat transfer, nucleate boiling plays an important role because the maximum heat is transferred in this regime from the surface though vapor bubbles in the working fluid. As the wall superheat increases further, the vapor bubbles start merging with the adjacent bubbles and form vapor jets [56]. In nucleate pool-boiling, the heat flux cannot be increased indefinitely. The maximum heat is transferred at a certain point C, called the Critical Heat Flux (CHF) for a certain value of wall superheat. Beyond the CHF, the steam produced over the surface forms an insulating layer, which impacts the heat transfer coefficient by decreasing the heat transfer rate. It occurs because a large portion of the surface is covered by a vapor film, which acts as thermal insulation due to the low thermal conductivity of vapor relative to the liquid. Immediately after CHF, the boiling becomes unstable and vapor bubbles start exploding. At this point transition boiling occurs. As the heat flux increases further, a film boiling starts at a very high wall superheat about 30K, beyond 200°C. The vapor bubbles drift on a vapor cushion and evaporate very slowly.

1.3.1 Nucleate Boiling

In 1950s, it was recognized that the boiling initiates from the nucleation of bubbles from the surface imperfections/cavities present on the heated surface [34].

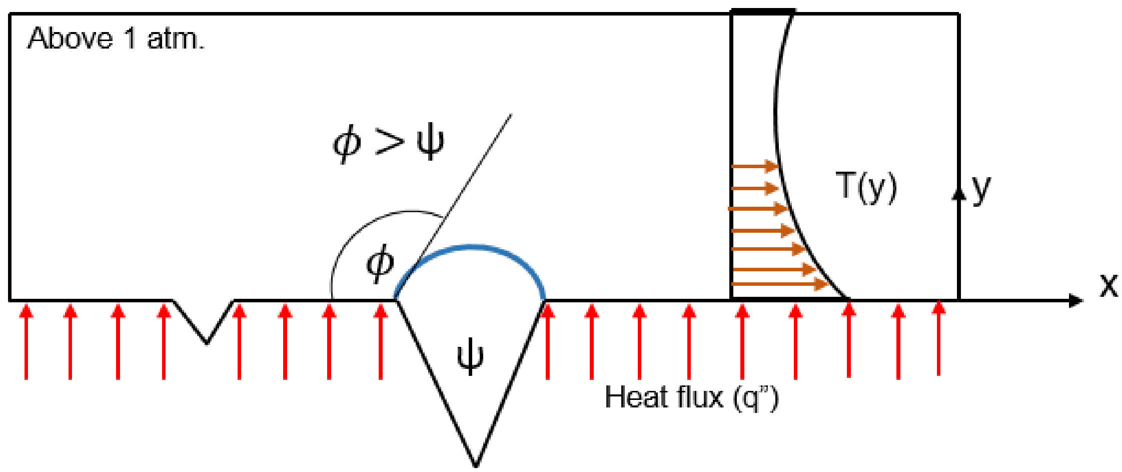

Figure 1.8 A schematic of cavity that entraps gas/vapor on the surface. The angle ϕ and ψ represent the contact angle and cavity angle respectively [34].

The gas/vapor present in the working fluid entraps in the cavities and act as a nuclei for bubble nucleation as shown in Fig 1.8.

1.3.2 Active Nucleation Sites

According to the theory presented by Hsu [60], the size of active nucleation sites depends on the wall superheats, pressure of the system, surface morphology and boundary layer thickness of the superheated layer. The radius of active nucleation sites, r is expressed by:

$$\{r_{max}, r_{min}\} = \frac{\delta}{2C_1}\left[1 - \frac{\theta_{sat}}{\theta_w} \pm \sqrt{\left(1 - \frac{\theta_{sat}}{\theta_w}\right)^2 - \frac{4AC_2}{\delta\theta_w}}\right] \quad (1.1)$$

For the saturated boiling condition, the fluid temperature is the same as the saturation temperature of the liquid. θ_{sat} is defined by $T_s - T_{sat} = 0$.

$$\{r_{max}, r_{min}\} = \frac{\delta}{2C_1}\left[1 \pm \sqrt{1 - \frac{4AC_2}{\delta\theta_w}}\right] \qquad (1.2)$$

where, δ is the boundary layer thickness, $C_1 = (1 + cos\,Ø)/sin\,Ø$, $C_2 = (1 + cos\,Ø)$, Ø is the wetting angle, $A = 2\sigma T_{sat}/\rho_v h_{lv}$ and, $\theta_w = T_w - T_{sat}$.

The cavity size depends on the properties of the working fluid and the surface wettability.

To study the effect of pressure on the cavity size, Eq. (1.1) is plotted at saturated conditions at different pressures. Fig. 1.9 demonstrates the effect of pressure on the active nucleation size at a micron level.

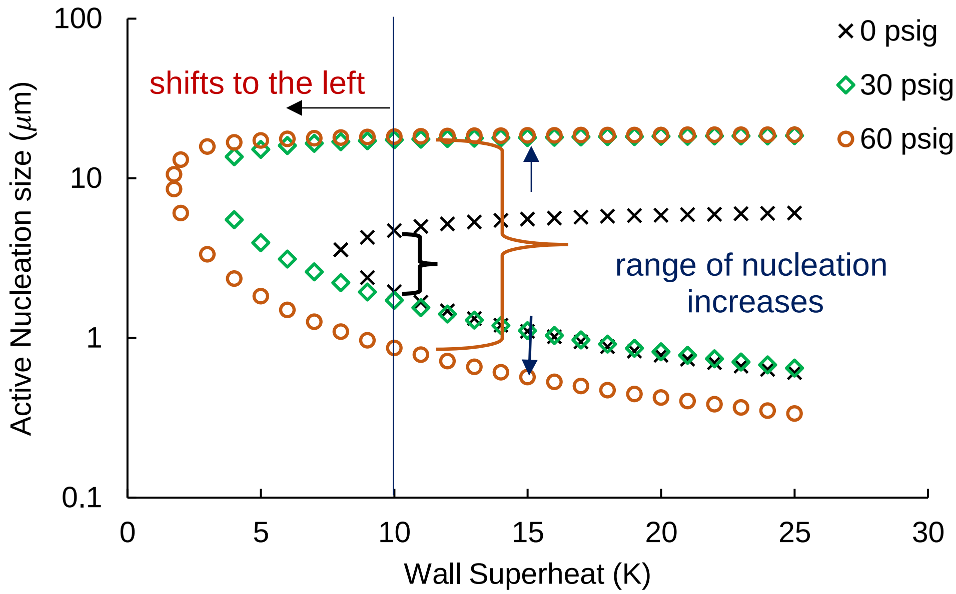

Figure 1.9 The impact of pressure on the nucleation sites at high-pressures

Pressure activates the nucleation sites at a micron level as shown in Fig 1.9. For example, at the same wall superheat of 10 K shown in Fig. 1.9, the size range of active nucleation sites is much larger for 60 psig than the atmospheric pressure. Henceforth, we get more nucleation points on the heated surface.

Thermophysical properties of water change with increasing pressure. The thermophysical properties of water are tabulated in Table 1-3 for different pressures.

Table 1-3 Thermophysical properties of water at high-pressures

Pressure (in psi)	h_{fg} (J/kg)	ρ_l (kg/m^3)	ρ_v (kg/m^3)	g (m/s^2)	σ (N/m)
15	2258000	958.5	0.591	9.81	0.0589
30	2203000	943.4	1.121	9.81	0.0546
45	2174000	934.6	1.496	9.81	0.0522
60	2133800	921.7	1.965	9.81	0.0505
75	2122500	918.4	2.010	9.81	0.0486

As pressure increases, the latent heat of vaporization and the specific volume of liquid decreases.

The active nucleation site size range can be determined from the equation (1.2) as a function of wall superheat, θ_w. If the required heat flux for the inception of boiling is known, the boundary layer thickness, δ can be predicted using equation (1.3),

$$\delta = \sqrt{\frac{4kAC_3}{q_0}} \quad (1.3)$$

where, k is the thermal conductivity of the liquid and q_0 is the required heat flux which can be obtained from the experiments.

1.3.3 Bubble Departure Size

Based on hydrodynamic theory, Fritz [61] predicted the bubble departure diameter depends on the surface tension of liquid, contact angle and the buoyant force, is shown in equation 1.4.

$$D_d = 0.0208\phi \left[\frac{\sigma}{g(\rho_l - \rho_g)}\right]^{1/2} \quad (1.4)$$

where, D_d is the bubble departure diameter, ϕ is the contact angle, σ is the surface tension of the liquid, ρ_l and ρ_g are the density of liquid and vapor.

1.3.4 Nucleation Site Density

The density of active nucleation sites plays a key role in the liquid- vapor phase change heat transfer. Mikic and Rohsenow [62] correlates the active nucleation site density and the size of the cavities present on the surface for the partial nucleate boiling regime. The expression is given by,

$$n_a' = \left[\frac{D_s}{\frac{4\sigma T_{sat}}{\rho_v h_{lg} \theta_w}}\right]^m \quad (1.5)$$

where, m is the empirical constant, D_s is the maximum cavity diameter of the surface, σ is the surface tension of the liquid, T_{sat} is the liquid saturation temperature, ρ_v is the vapor density, h_{lg} is latent heat of vaporization, and θ_w is the wall superheat.

1.3.5 Bubble Departure Frequency

The bubble release frequency can be estimated using Zuber's [56] correlation, expressed by:

$$f D_d = 0.59 \left[\frac{\sigma g(\rho_l - \rho_g)}{{\rho_l}^2}\right]^{1/4} \quad (1.6)$$

where, f is the bubble release frequency, D_d is the departure diameter, g is the gravity, σ is the surface tension and ρ_l and ρ_v are the liquid and vapor density respectively.

1.3.5 Heat Transfer Coefficient

The heat transfer coefficient is determined by the Forster and Grief [63] micro convection model:

$$HTC = 2(2\Pi k_l \rho_l c_{pl})^{1/2} {D_d}^2 f^{1/2} \eta_a' \quad (1.7)$$

Where, k_l is the conductivity of the liquid, ρ_l is the density of liquid, c_{pl} is the specific heat of liquid, D_d is the departure diameter, f is the bubble release frequency and $\eta_a{}'$ is the active nucleation site densities.

1.4 Outline and Objectives

1.4.1 Outline of the Thesis

The outline of the thesis is given in this section. The topics covered in the following sections are as follows:

In **Chapter 2**, the design fabrication of the copper sample is illustrated with the high-pressure pool-boiling test facility. The working principle of a back pressure regulator valve is also shown in the chapter. The test procedure of the experiment is explained with the uncertainty measurements in the experimental data. The objective of the work is to provide detailed information about the design set up of the pool-boiling experimental facility.

In **Chapter 3**, the high-pressure pool-boiling theory is discussed using Hsu's theory. The objective of the work is to develop a fundamental understanding of the pool-boiling behavior at high-pressure. The effect of high-pressure on the bubble dynamics is studied with the bubble departure size, bubble departure frequency, and the nucleation site densities. The experimental results are also validated with the existing models. The CHF enhancement is also discussed through bubble dynamics. The HTC is compared with existing correlations in the literature.

In **Chapter 4**, the combined effect of wettability and high-pressure are explored in the performance of pool-boiling heat transfer. The objective of this work is to explore the boiling behavior and mechanism of heat transfer enhancement for a Teflon coated surface. The surface preparation of a Teflon coating and characteristics are described in this section. The static contact angle measurement is also performed for the polished copper surface, and the Teflon coated copper surface. The bubble dynamic is studied analytically with the existing correlations for different wettability. The pool-boiling results at high-pressure is discussed for the Teflon coated surface and compared with the polished copper surface.

In **Chapter 5**, a key approach for fabricating a wick structure is explained in detail. The objective of this work is to understand the combined effect of wick structure and pressure in the heat transfer enhancement mechanism. The surface characteristics are studied with static contact angle measurements. The pool-boiling heat transfer enhancement and its mechanism are discussed in this section. The results are compared and validated with the existing models for the enhanced heat transfer for the sintered wicks.

In **Chapter 6**, the mechanism for heat transfer enhancement on a wick structure is discussed in this chapter. The pool-boiling heat transfer enhancement using a porous wick structure depends on many factors such as the size of the sintered wick particles, packaging structure, and the thermal resistance provided by the layered wick. The objective of this chapter is to develop a theory which explains the heat transfer enhancement mechanisms with the packaging pattern of the wick particles. The pressure effect will further explain in the heat transfer enhancement mechanism. A parametric study has been performed for heat transfer enhancement for different sizes of sintered particles. We present a numerical model to optimize the size of sintered particles to enhance the performance of pool-boiling at high-pressures.

Finally, the concluding remarks and future work are presented in Chapter 7. The full list of the publications during the doctoral studies are listed at the end of the thesis with poster presentations and conference proceedings. Abbreviations and nomenclatures are presented at the start of the dissertation (page xvi and xvii).

Chapter 2 - Experimental Setup

2.1 Introduction

The high-pressure pool-boiling experimental facility is presented in this chapter. The experiments are performed on a plain copper surface at high-pressures. The pool-boiling performance is also investigated for the sintered wick structures. The fabrication process of the wick layer is also illustrated with the surface characterization. The experimental method, test procedures, data reduction, and measurement uncertainties are presented in this chapter.

2.2 Fabrication Procedure

2.2.1 Sample Fabrication: Plain copper

The high-pressure pool-boiling experiments are performed on a plain copper surface. Copper is chosen for pool-boiling tests because of its high thermal conductivity. The schematic of the copper substrate with the heater arrangement is shown in Fig 2.1. The height of the copper rod is 7.62 cm long. The top portion of the copper rod is 1 cm in diameter and 2.54 cm long. The bottom portion is 2.54 cm in diameter and 2.51 cm long. The total surface area of the top portion of the heating block is chosen as approximately 1 cm^2. The copper rod is insulated with a PTFE block. The copper rod is micro milled and cleaned by extra fine sand paper before the tests.

2.3 Experimental Setup, Test Procedure and Uncertainty

2.3.1 High-pressure Pool-boiling Test Facility

The schematic of the experimental setup is shown in Fig 2.2 including the heating block with the Teflon insulated surface, heater arrangement, and data acquisition system. A similar test setup was used in Dahariya and Betz [42]. The experimental setup is built for the maximum rated pressure of 900 psig. It consists of a boiling vessel (17.94 cm long and 10.16 cm in diameter with a wall thickness of 0.95 cm) made from 304 stainless steel. The end walls of the boiling vessel are tightly sealed with the Poly Tetra Fluro Ethylene (PTFE) gaskets and flanged with 18 stainless steel ¾ in. threaded nuts. A copper helical tube is used to condense the steam inside the boiling vessel. A pressure transducer is mounted on the top of the vessel to monitor the pressure inside the boiling vessel during the experiments at high-pressures using the Data Acquisition system. The copper block assembly with the insulated surfaces and heating rod is shown in Fig 2.1.

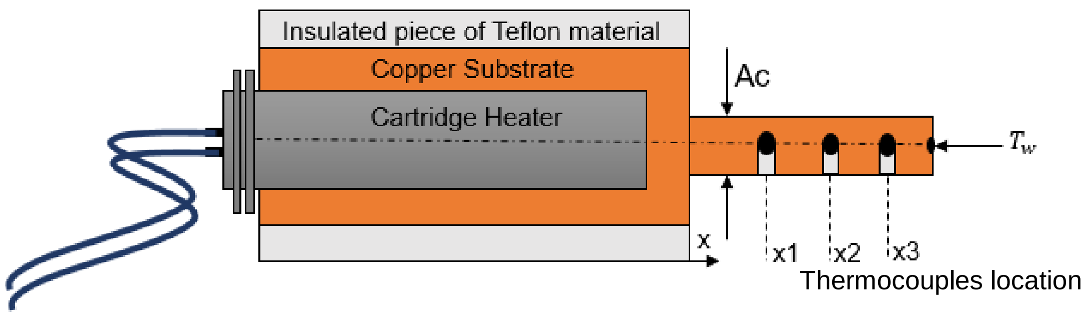

Figure 2.1 The heater assembly with the copper substrate and the Teflon block.

The copper block is insulated with the PTFE surface. The gap is filled with a high temperature copper sealant to avoid any water leakage and heat loss through the gap. Three thermocouple holes are drilled through the vessel, the Teflon block, and the center of the copper rod to measure the surface temperature. The three thermocouples were placed at x1 = 3 mm, x2 = 9 mm and x3 = 15 mm from the top surface of copper substrate. The surface temperature is extrapolated from the measured temperatures from the thermocouple readings. High conductive thermal paste is applied to the thermocouples to maintain a low resistance between the thermocouples and copper surface. A K-type of thermocouple is placed inside the boiling vessel to measure the bulk temperature of saturated water. The heat input is generated by a 500 W, 0.496´´ Watlow fire rod cartridge heater. The heater is inserted from the back end of the copper block of 2.54 cm diameter. The heat flux is provided using the AC-DC power controller manufactured by TDK-Lambda. The power input of the cartridge heater is controlled by a relay controller with a duty cycle of 1-10 V analog input over a period of 1s.

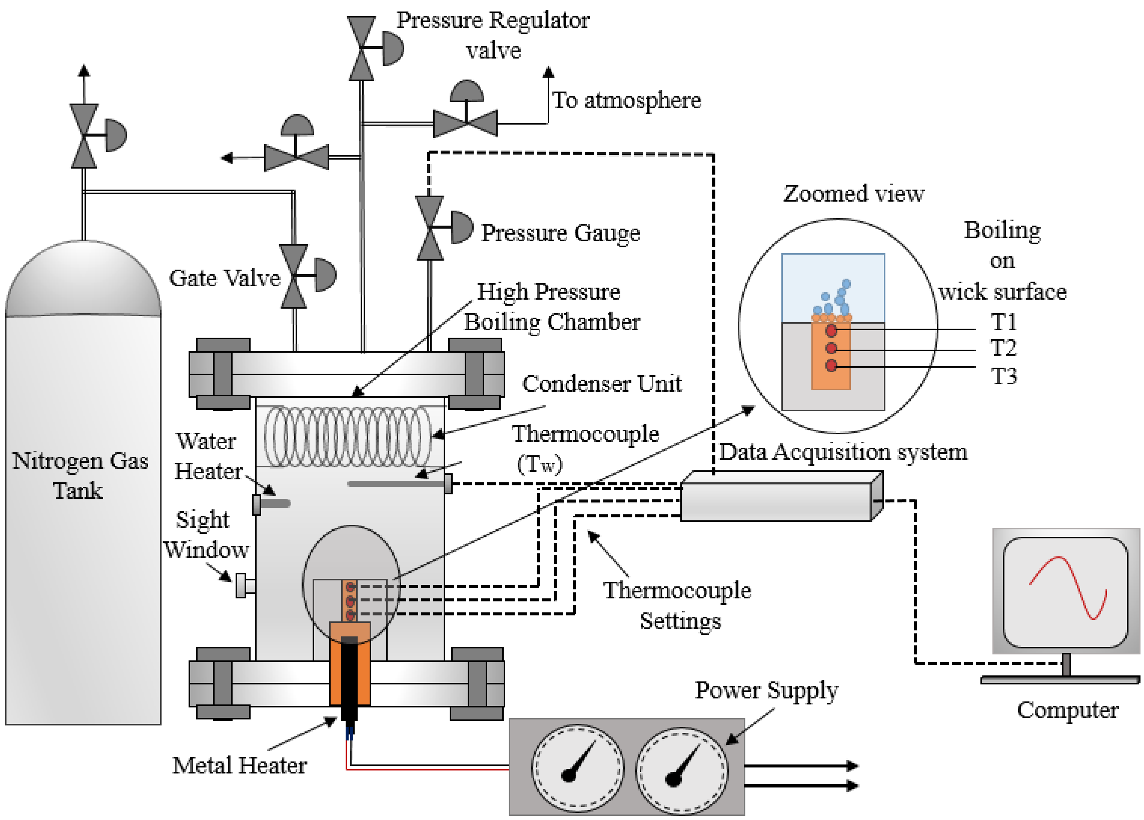

Figure 2.2 The schematic of the pool-boiling experimental setup with the boiling vessel, back pressure regulator, nitrogen gas, data acquisition system, thermocouples setting, sight window, and heater assembly.

A 250 W, 120 V water heater is inserted from the side of the boiling vessel to maintain the water saturation temperature during the experiments. The level of the water and the boiling behavior are visualized through the 1 in. NPT Sapphire Bonded (maximum rated pressure 1000 PSI) window. A 1/8 in. NPT glass window is mounted on the top of the boiling vessel to allow a lighting system to illuminate the inside of the vessel. The boiling process is recorded by a high speed camera (Sony RX100 VI).

Two ports of 1/8 in. are used on the top flange for nitrogen gas inlet and water vapor outlet. Nitrogen gas is used to pressurize the boiling vessel due to its inert property of Nitrogen gas. The desired system pressure is maintained by regulating the nitrogen gas flow rate using a high-pressure regulator gate valve of maximum rated pressure 1500 psi manufactured by Harris Products Group. A butterfly gate valve is used between the boiling vessel and pressure regulator valve to avoid back pressure flow of water vapor. To ensure a high level of safety, the entire system is insulated and designed with metal piping.

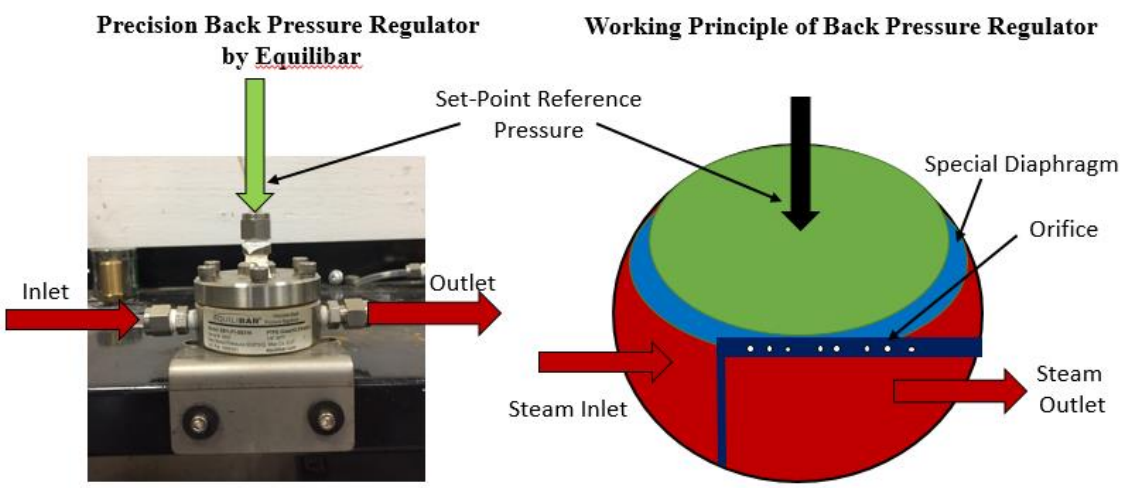

Figure 2.3 The working principle of precision back pressure valve of stainless steel body. It controls the pressure by balancing three-way force where the diaphragm touches to the outlet orifice.

A back pressure regulator valve (1/4 in port, maximum pressure 0 - 750 psi, maximum CV 1.2) made of stainless steel 316/316 is used to release the extra pressure due to the formation of steam inside the boiling vessel. It is purchased by Equilibar, Precision Pressure Control. The Equilibar pressure regulator valve works differently from a traditional back pressure regulator valve. It controls the inlet pressure by controlling three-way force from inlet, reference point and ambient. The working principle of the back pressure regulating valve is shown in Fig. 2.3 with a picture of the regulator valve.

2.3.2 Test Procedure

The pool-boiling experiment was performed in deionized water to avoid any contaminants being deposited on the surface. The high-pressure pool-boiling test is performed in a pressurized boiling chamber. The boiling vessel is first pressurized with compressed nitrogen gas. The nitrogen gas is drawn from the nitrogen gas tank into the boiling vessel through a high-pressure regulator valve. The system pressure is monitored for 5-6 minutes until the pressure stabilizes through the pressure transducer. The bubble test is performed to ensure any gas leakage. As the pressure stabilizes, the water is heated for an hour to remove the non-condensable gases from the boiling vessel. Once degasification is performed, the heater rod is turned on to heat the copper surface. The surface temperature, water temperature and pressure are monitored using the DAQ system in the computer monitor. The boiling data is collected for an interval of 10 minutes after the system reaches steady state. Steady state is defined as in the temperature measurement, when the surface temperature reading changes at a rate of less than 1°C/min time averaged over a period of 10 min. Measurements are taken for a minute for each heat flux at a scan rate of 60 data points. The water level is constantly monitored to avoid water heater burn out. The surface temperature is determined using an extrapolation technique. The measurements are taken at different heat fluxes to construct a boiling curve.

2.3.3 Data Reduction and Measurement Uncertainties

The recorded temperatures are averaged over the 60 data points for each heat flux. The surface temperature is extrapolated from the recorded temperature from the thermocouple readings with respect to the specified locations. The thermal gradient dT/dx is calculated using the three point backward difference Taylor's approximation expressed in Eq. (2.1).

$$\frac{dT}{dx} = \frac{3T_1 - 4T_2 + T_3}{2\Delta x} \tag{2.1}$$

The heat flux is calculated assuming one-dimensional heat conduction in the copper heat block using Fourier's law of heat conduction. The governing equation of 1D heat conduction for the heat flux is expressed in Eq (2.2),

$$q'' = -k_{cu}\frac{dT}{dx} \tag{2.2}$$

where, q'' is the heat flux per unit area, k_{cu} is the thermal conductivity of copper, and dT/dx is the thermal gradient.

A comprehensive uncertainty analysis is performed for the errors in the thermocouples, the pressure sensing device and losses in the heat flux measurements. All the reported results include these uncertainty estimates. The thermocouples are calibrated in the ice bath at 0° C and at saturated boiling water temperature of 98.8°C (low boiling temperature due to the pressure change) at 310m above sea level. The calibration is performed before the tests to reduce the bias errors in the test readings. The error in the thermocouple and data acquisition system is $\pm$1.1 K, which is a 0.75% error. The error in the pressure transducer is about 10.75 μV (0.08375 psig). The heat loss is determined from a difference of the calculated and the applied heat flux. The uncertainty is calculated in the measured heat flux using equation expressed in Eq. (2.3).

$$U = \sqrt{\sum_{i=1}^{n} \left(\frac{\partial P}{\partial a_i} U_{a_i}\right)} \qquad (2.3)$$

where, U is the uncertainty, P is the parameter, a_i is the measured parameter.

The error is estimated by evaluating uncertainty intervals for the thermal gradient and the intercept surface temperature from the heated surface. The boiling tests are performed under atmospheric condition for three times. The percentage of the error is calculated from the measured heat flux. The hysteresis curve is plotted and shown in Fig. 2.4 with an error bar.

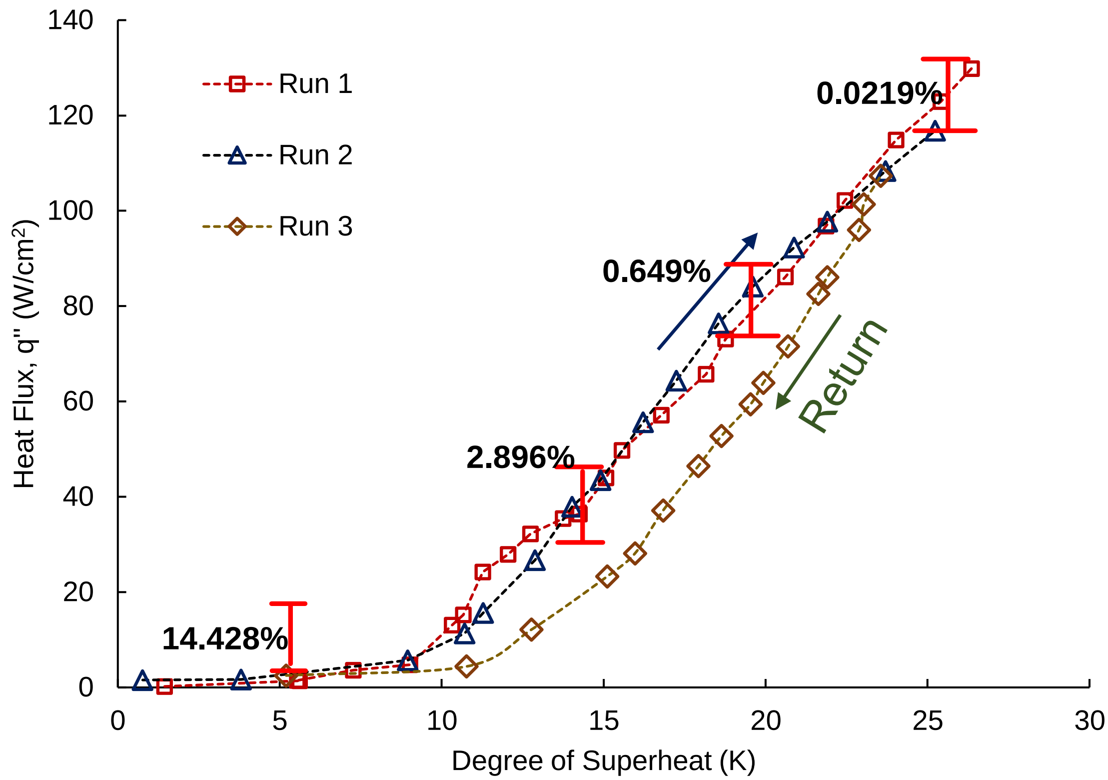

Figure 2.4 Uncertainty study in the hysteresis curve drawn from three sets of data points at 0 psig (0 kPa) with the averaged error.

At Onset, the average error is 14.428% and at 30 W/cm^2 the error is 2.896% at 0 psig (0kPa). The percentage of error is found to be higher at low heat flux than at high heat flux readings. A similar calculation is performed for high-pressure pool-boiling readings. The average error found at 45 W/cm^2 is 16.452%, 12.345%, and 15.632% for 2(30 psig) (206.8 kPa), 45 psig (310.2 kPa) and 60 psig (413.7 kPa) respectively.

Chapter 3 - High-pressure Pool-boiling Heat Transfer and Mechanism on a Copper Surface

3.1 Introduction

Boiling has been extensively studied for a decade [14]. Many correlations have been deduced and verified with the experimental data based on the bubble dynamics (bubble departure, departure frequency, bubble coalescence and nucleation site densities), and mechanisms of heat transfer (conduction, convection and evaporation). In order to understand the mechanism of pool-boiling heat transfer enhancement at high-pressure, the bubble dynamics at the solid-liquid interface are very important to study. The wettability affects the bubbles dynamic behavior, therefore it will impact the performance of heat transfer. Thermophysical properties of water such as the latent heat of vaporization, difference in specific densities of liquid and vapor, and surface tension decrease at high-pressure, change the bubble dynamics. The pool-boiling experiments have been performed at high-pressures. The results are discussed, critically analyzed with the previous work and compared to the existing models. The pool-boiling heat transfer enhancement is explained using an existing theoretical model at high-pressure. Later, the bubble dynamics (the bubble departure size, bubble release frequency and nucleation site densities) are analyzed from the boiling videos. The work presented in this section will draw attention to how the pressure will affect the performance of pool-boiling heat transfer and the bubble dynamics.

3.3 Results and Discussion

3.3.1 Bubble Dynamics

The pool-boiling heat transfer was investigated on the plain polished copper surface at different pressures. In order to demonstrate the nucleate boiling behavior at high-pressures in the low heat flux region, Fig. 3.1 shows the captured bubble images at 0 psig (0 kPa), 60 psig (413.7 kPa), and 90 psig (620.5 kPa).

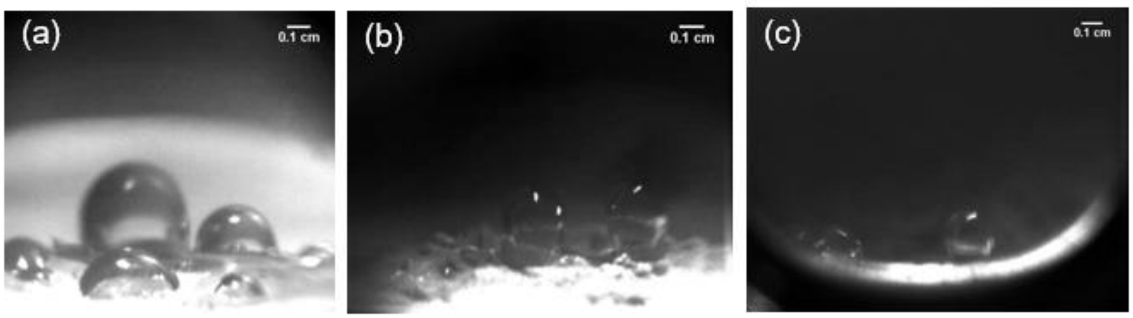

Figure 3.1 Images of bubble formation at onset for (a) 0 psig (0 kPa) and (b) 60 psig (413.7 kPa) (c) 90 psig (620.5 kPa) [64]

At 0 psig (0 kPa), the bubble starts nucleating at 1.857 W/cm^2. The effect of pressure can be seen on the size of nucleating bubbles from the heated surface. The bubble departure diameter was measured as approximately 4.58 mm, 2.42 mm, and 2.37 mm at 0 psig (0 kPa), 60 psig (413.7 kPa), and 90 psig respectively.

The size of the departing bubble was measured at different pressures as shown in Fig. 3.1, and the effect of heat flux in the bubble growth was also visualized in Fig. 3.2 at different heat fluxes for the 0 psig and 90 psig. Based on the image analysis, the bubble departure diameter was calculated. An error bar was added for the combined standard deviation and the measurement uncertainty is shown in Fig. 3.3.

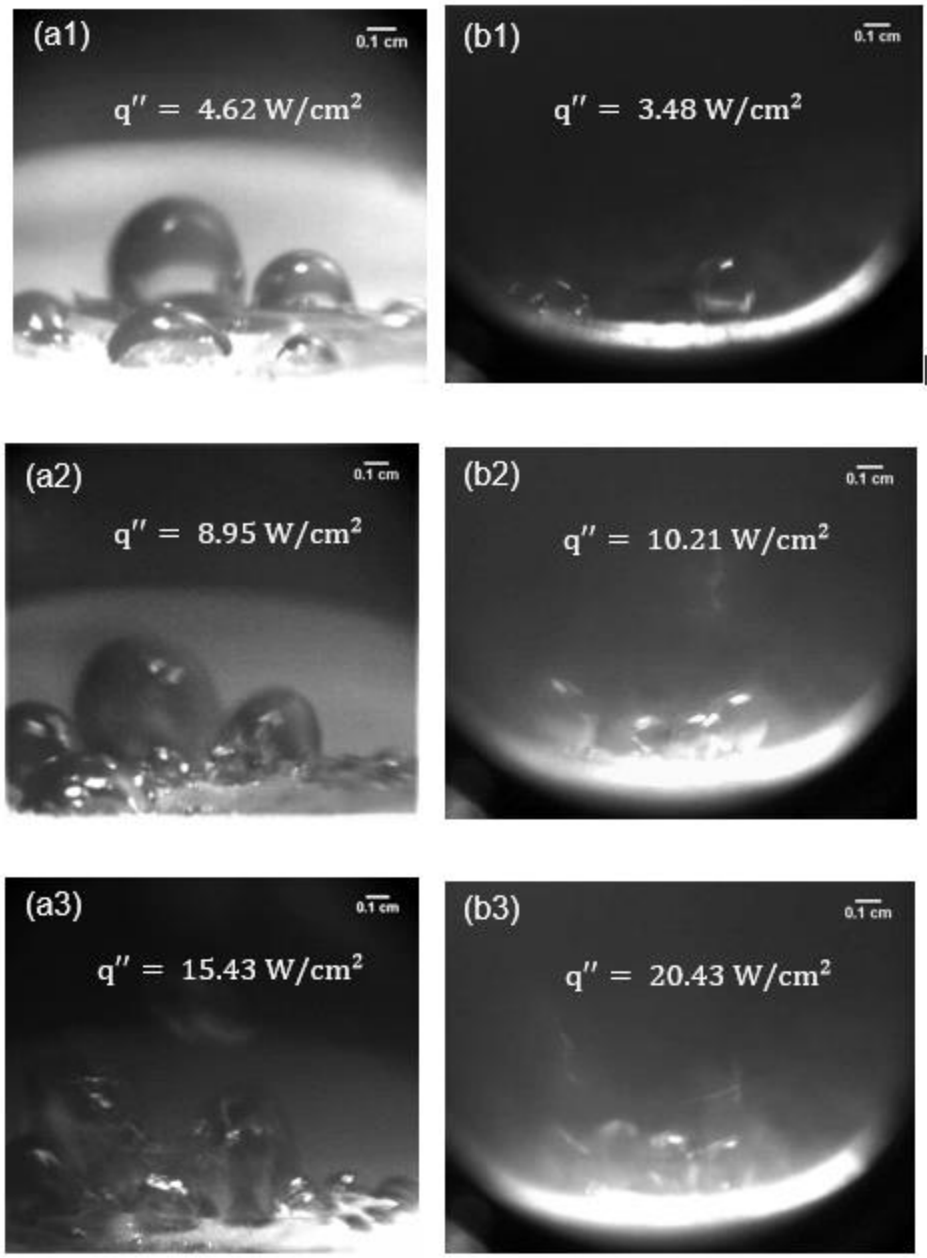

Figure 3.2 The image sequence for the nucleate pool-boiling behavior at different heat fluxes for pressures (a) 0 psig (0 kPa) and 90 psig (620.5 kPa) [64]

The effect of pressure can be seen on the primary departure bubble size as shown in Fig 3.2. The pressure reduces the size of nucleating bubbles significantly with increasing heat fluxes. As the heat flux is increased, the bubbles coalesce and form vapor. Approximately, 46% of the reduction is observed in the bubble size from the atmospheric condition to 90 psig (620.5 kPa). The results were also compared with the most widely used correlation by Fritz [39], based on a force balance.

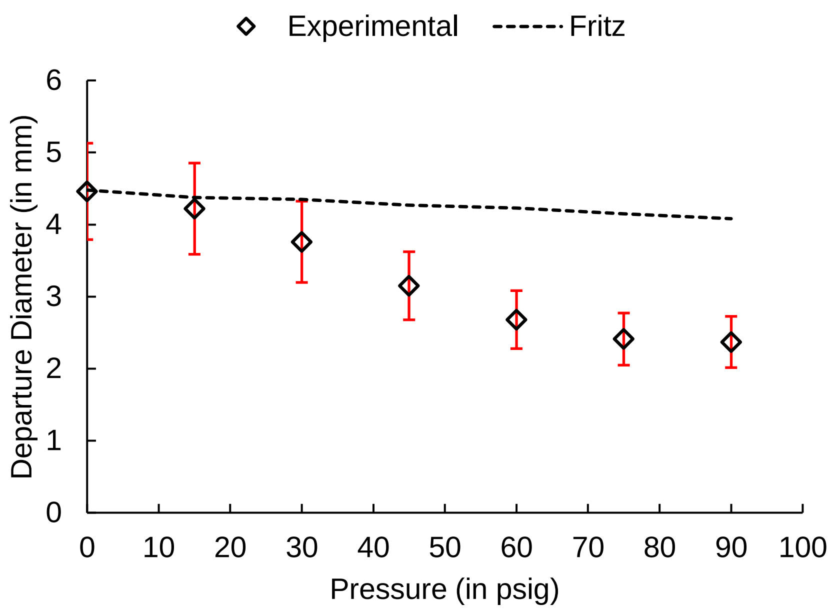

Figure 3.3 The primary bubble departure size on the horizontal surface with a standard error bar [64]

The results suggest that change in the specific volume of liquid-vapor may cause the change in bubble departure size. The experimental results are plotted against the Fritz's correlation and found to be a similar trend. Sakashita et al. observed that the diameter of coalesced bubbles increases with heat flux and pressure [17]. They found that the size of the departing bubble is inversely proportional to pressure and leads bubble to coalesce at very low heat flux of 0.0614 MW/m^2. Sakashita et al. analyzed in their experiments at 2.70 MPa on the horizontal heating surface [40]. The size and primary bubble growth rates become smaller at high-pressures, and surface tension forces dominate over buoyancy. Labuntsov et al. investigated the similar nature in the growth rates of departing bubbles at high-pressures [65]. They analyzed their studies based on the evaporation rate of liquid close to the bubble base.

At high-pressures, the excess rate of change of enthalpy of the bulk liquid surrounding the bubbles impacts the bubble size. The experiments were performed at high-pressures on horizontal and vertical surfaces, and revealed that the pressure slows down the bubble growth rate. The rate of departing bubbles was also measured. At 0 psig (0 kPa), the bubble takes approximately 17 seconds, and at 60 psig (413.7 kPa) it takes approximately 13 seconds. It shows that the bubble departure frequency increases with increasing pressure. With increasing pressure the surface tension of liquid decreases, which may affect the reaction forces on the departing bubbles.

3.3.2 The Bubble Departure Frequency

The bubble departure frequency was calculated from averaging the first sixty frames of the departed bubble videos for every second. The theoretical curve was approximated by Zuber's correlation expressed in Eq. (1.6).

The experimental results for the bubble departure frequency were compared with the predicted data as shown in Fig. 3.4. At high-pressure, the detachment frequency increases. A large variation from he predicted results is noticed. However, a similar trend (same slope) can be seen in the predicted and experimental data. The detachment frequency increases slightly with pressure which is seen in the experimental data. The pressure effect on the departure frequency is hardly noticed in the Zuber's predicted theory.

Boborovich and Mamontva performed experiments across a wide range of pressures about 0.1 to 5.35 MPa on a 2 mm wide rectangular horizontal heating surface and found that the detachment frequencies are unaffected by heat flux with little dependence on pressure [66]. However, they observed a slight increase in the averaged values with pressure.

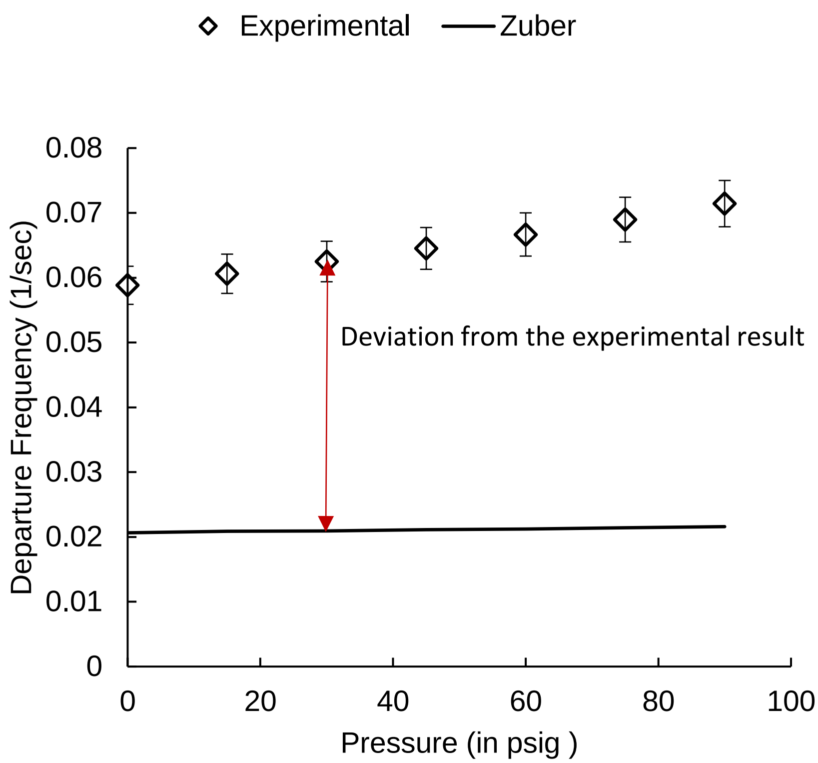

Figure 3.4 Bubble departure frequency at different high-pressures [64]

Sakashita et.al observed the boiling behaviors on a horizontal, upward facing plate from atmospheric pressure up to 7 MPa [17] and noticed a negligible effect in the detachment frequency at high heat flux and pressure.

The pressure effect can be observed on the nucleation site densities. A different nucleation behavior was measured at high-pressure. In Fig. 3.2, a higher number of active nucleating sites is observed at 60 psig (413.7 kPa) at the onset boiling point compared to the atmospheric result. Consequently, as the flux increases the bubble starts to coalesce with the neighboring bubbles which can be seen in Fig. 3.2. Sakashita et.al, made a similar observation on the number of active nucleation sites [40]. The effect of pressure was studied on the nucleation site densities at one heat flux condition and found that the nucleation density increases in proportion to 1.5^{th} of the pressure.

3.3.2 Heat Transfer Performance

3.3.2.1 Heat Transfer Coefficient

Fig 3.5 presents the heat transfer performance curves for different high-pressures.

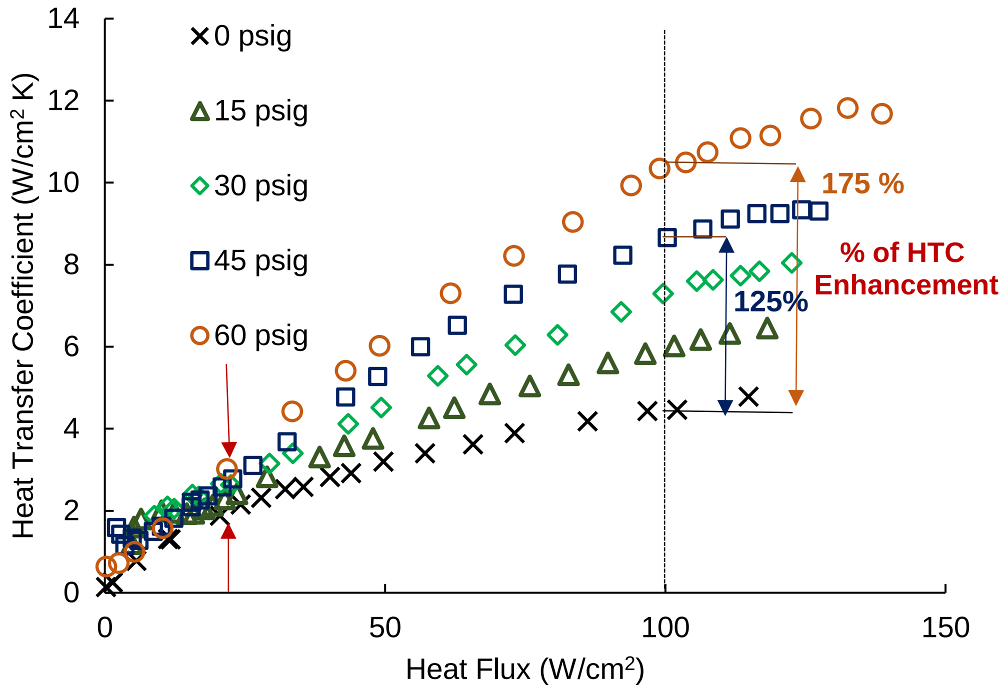

Figure 3.5 The heat transfer performance curve for different high-pressures [64]

For example, at 100 W/cm^2, 50%, 75%, 125%, and 175% of enhancement was measured for 0 psig (0 kPa) , 15 psig (103.4 kPa), 30 psig (206.6 kPa), 45 psig (310.2 kPa), and 60 psig (413. 7 kPa) respectively. At 25 W/cm^2 of heat flux, the HTC value varies from 2- 4 W/cm^2 K for the pressure value from 0 psig (0 kPa) to 60 psig (413.7 kPa). The results suggest that pressure has a significant impact on the heat transfer performance at high heat flux. Guan et al. [67] found similar results in saturated horizontal pool-boiling with chamber pressures of 150 kPa, 300 kPa, and 450 kPa on the brass heater surface for pentane, hexane and FC-72. In the natural convection regime they had noticed there was no significant change in the heat transfer coefficient with pressure. However, they noticed a remarkable effect of pressure in the heat transfer coefficients at high heat flux. Li and Betz [39], reported 126.8% enhancement in the HTC at atmospheric pressure and 51.5 % at 45 psig (308 kPa) on the Graphene Oxide (GO) coated surface at heat flux 30 W/cm^2. The change in the HTC for the GO coated surface was related to the excessive bubble generation from the surface and the enhanced thermal conductivity due to higher thermal conductivity of Graphene.

Figs. 3.6 – 3.10 compares the high-pressure data with the predicted values from different correlations. The data were plotted for the measured heat transfer coefficient values against the heat flux values. The most widely used correlation of the critical heat flux of Rohsenow [37] expressed in Eq. (3.5) was used to compare the result. The model is mostly dependent on the property of liquid and the surface property.

$$\frac{q}{A} = \mu_l h_{lg} \left[\frac{g(\rho_l - \rho_v)}{\sigma}\right]^{1/2} \left[\frac{c_{pl}(T_s - T_{sat})}{C_{sf} h_{lv} {Pr_l}^n}\right]^3 \quad (3.5)$$

The HTC is a function of the various fluid properties. The fluid properties were evaluated at the saturation temperature corresponding to the local pressure, and, C_{sf} is a function of the particular heating surface-fluid combination. In the modeling, the mass velocity of the vapor bubbles leaving from the surface was considered, and also the contact angle was determined by the values of $\sigma_{sl}, \sigma_{lv}, and\ \sigma_{vs}$, which was determined by the kind of fluid and the heating surface. From the boiling images, we observed the number of nucleation density increases at high-pressure, which can cause the higher rate of vapor formation. In the end, we suggest that the model considers the surface-fluid interaction which may be affected at high-pressure and the HTC best fits with the Rohsenow's predicted correlation.

The performance of the heat transfer coefficient was also determined by Foster's [68] micro convection model:

$$HTC = 2\,(2\Pi k_l \rho_l c_{pl})^{1/2} {D_d}^2 f^{1/2} {\eta'}_a \quad (3.6)$$

Where, ${\eta'}_a$ is the active nucleation site density.

The enhancement in the HTC was observed using the Forster's correlation because the heat transfer was attributed to the agitation of the liquid by the bubble motion, and it was determined by the boiling parameters.

Stephan and Abdelsalam's [69] considered pressure in the model is expressed in Eq. (3.7)

$$HTC_{nb} = 0.0546 \left(\frac{k_l}{D_d}\right) \left[\left(\frac{\rho_v}{\rho_l}\right)^{1/2} \left(\frac{qD_d}{k_l T_{sat}}\right)\right]^{0.67} \left(\frac{\rho_l - \rho_v}{\rho_l}\right)^{-4.33} \left(\frac{h_{lv} {D_d}^2}{{\alpha_l}^2}\right)^{0.246} \tag{3.7}$$

Stephan and Abdelsalam's correlation modeling was based on a mechanistic model. In the model, D_d represents the departure diameter and it was determined by Fritz's correlation. A dimensionless heat flux was modeled which was related to several dimensionless parameters that depended on the fluid and solid properties. The regression analysis was used to identify the important fluid property, and the values of exponents of the property group were obtained by matching predictions with data. In addition, the surface property was also considered in the modeling.

Fig. 3.6 compares the heat performance data with the predicted models [68] [69][70] at 0 psig (0 kPa). The experimental data agree well with Rohsenow's [70] model. 0.23 % of deviation was found with the experimental value at 0 psig (0 kPa). At high-pressure, 0.84%, 0.96%, 2.22 %, and 2.54 % deviation was found at 15 psig (103.4 kPa), 30 psig (206.6 kPa), 45 psig (310.2 kPa), and 60 psig (413.7 kPa) respectively. The high-pressure data has a pretty good agreement with the experimental values. Micro-convection theory considers bubble dynamics behavior in the performance of pool-boiling prediction. The micro-convection model considers all the parameters of bubble departure which are diameter, detachment frequency, and nucleation site density. It was observed previously that pressure has a huge effect on the boiling performance. Therefore, this could be the reason the model captured the experimental data well. The HTC value is under predicted at atmospheric pressure by 4.69%. However, the high-pressure data are over predicted from 1.16%, 6.41%, 10.83% and 10.94%, at 15 psig (103.4 kPa), 30 psig (206.6 kPa), 45 psig (310.2 kPa) and 60 psig (413.7 kPa), respectively. As the pressure increases, the percentage of deviation increases. A similar trend is found in the predicted correlation by Stephan and Abdelsalam's [69]. At 0 psig (0 kPa), the value is under predicted by 12.44%. In comparison to high-pressures, the range of deviation varies to 12.44% with the predicted model. However, at 15 psig (103.4 kPa), 3.21 % of deviation is found, capturing the high-pressure data is an acceptable range of $\pm$ 20%. As pressure increases, 18.23%, 21.36% and 23.72 % of differences are noticed at 30 psig (206.6 kPa), 45 psig (310.2 kPa) and 60 psig (413.7 kPa) respectively. A summary of the percentage deviation from the experiment in the heat transfer coefficient value at different pressures is tabulated in Table 3-2.

Table 3-1 Percentage of deviation from the experiment in the heat transfer coefficient at different pressures.

S. No.	Correlation	**Pressure (in psig)**				
		0	**15**	**30**	**45**	**60**
1.	Rohsenow (1951) [70]	0.23	0.84	0.96	2.22	2.54
2.	Foster & Greif (1959) [68]	4.69	1.16	6.41	10.83	10.94
3.	Stephan & Abdelsalam (1980) [69]	12.44	3.21	18.23	21.36	23.72

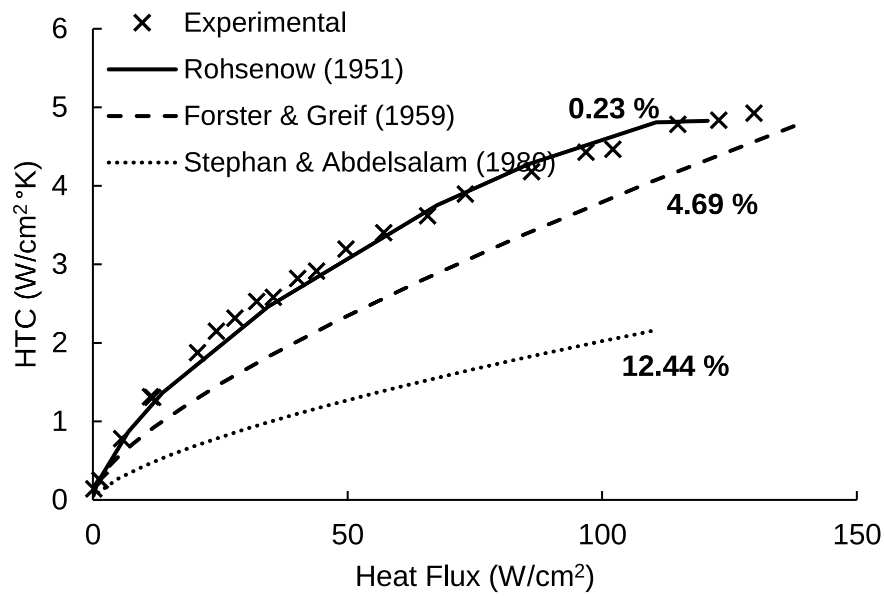

Figure 3.6 Comparison of heat transfer data at pressure 0 psig (0 kPa) with the predicted data using different models from the literature [64]

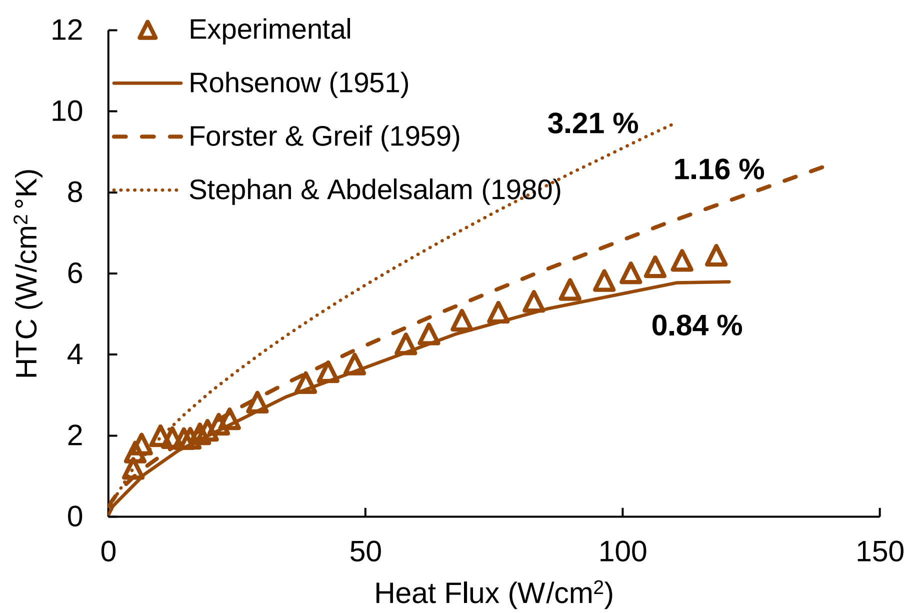

Figure 3.7 Comparison of heat transfer performance at pressure 15 psig (103.4 kPa) with the predicted data using different models from the literature [64]

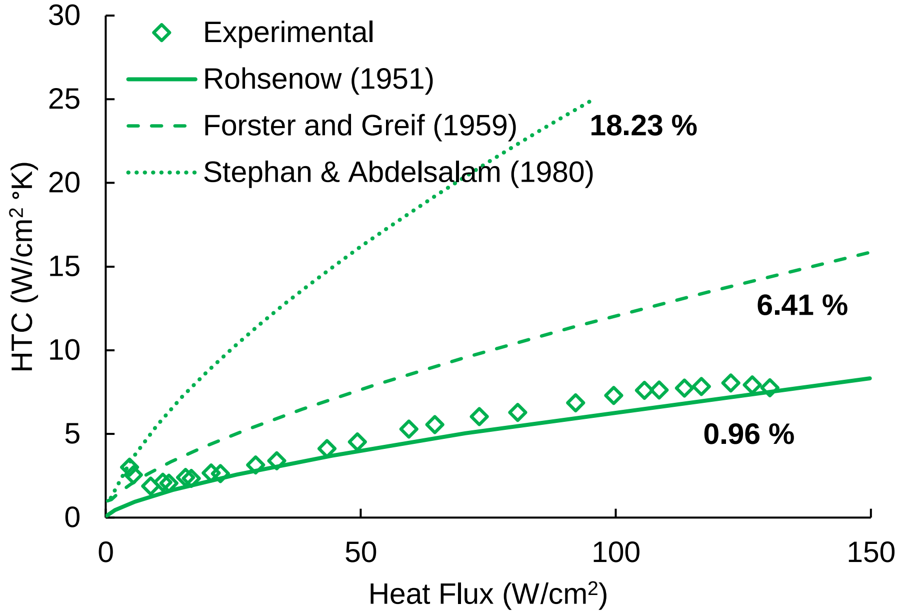

Figure 3.8 Comparison of heat transfer performance at pressure 30 psig (206.6 kPa) with the predicted data using different models from the literature [64]

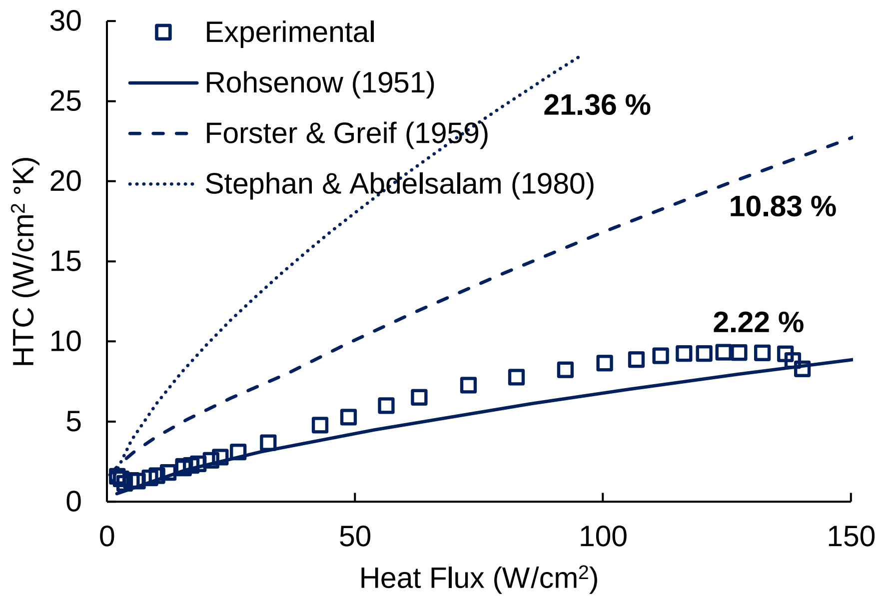

Figure 3.9 Comparison of heat transfer performance at pressure 45 psig (310.2 kPa) with the predicted data using different models from the literature [74]

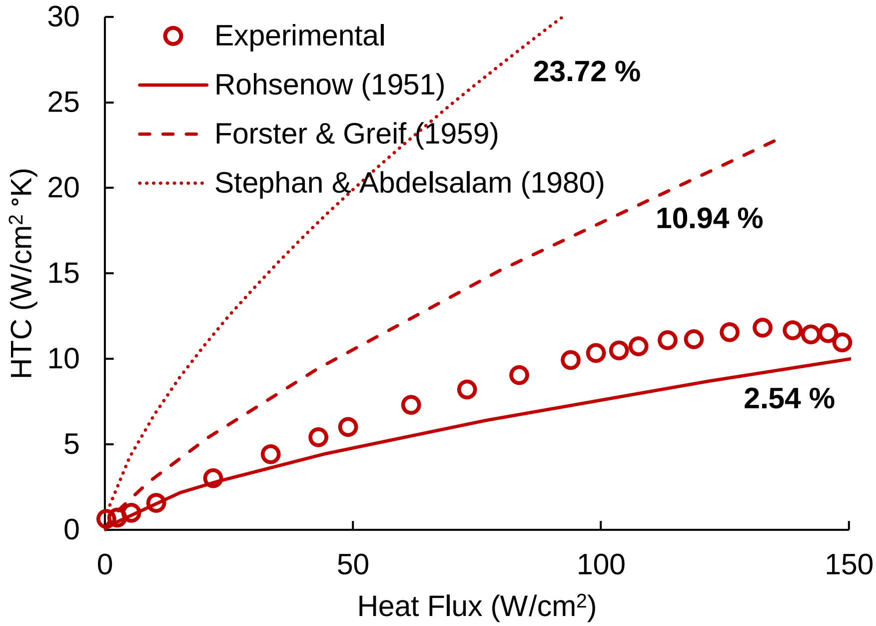

Figure 3.10 Comparison for heat transfer performance at pressure 60 psig (413.7 kPa) with the predicted data using different models from the literature [74]

3.3.2.2 Critical Heat Flux

The CHF is defined as the maximum thermal limit of the nucleate boiling and the lowest limit of film boiling of a vapor cloud formation on the surface where the heat transfer performance starts decreasing. The mechanism of Critical Heat Flux (CHF) for high-pressure pool-boiling is explained in this section. In the experiment, the CHF is determined from the last stable observed surface temperature. The CHF value is also compared with the different models as shown in Fig 3.11 to validate the experimental results.

The effect of pressure on the CHF is observed and analyzed. With the heat transfer performance, the CHF increases with varying pressure. Zuber [56] was the first to explain the CHF mechanism based on the hydrodynamic instabilities.

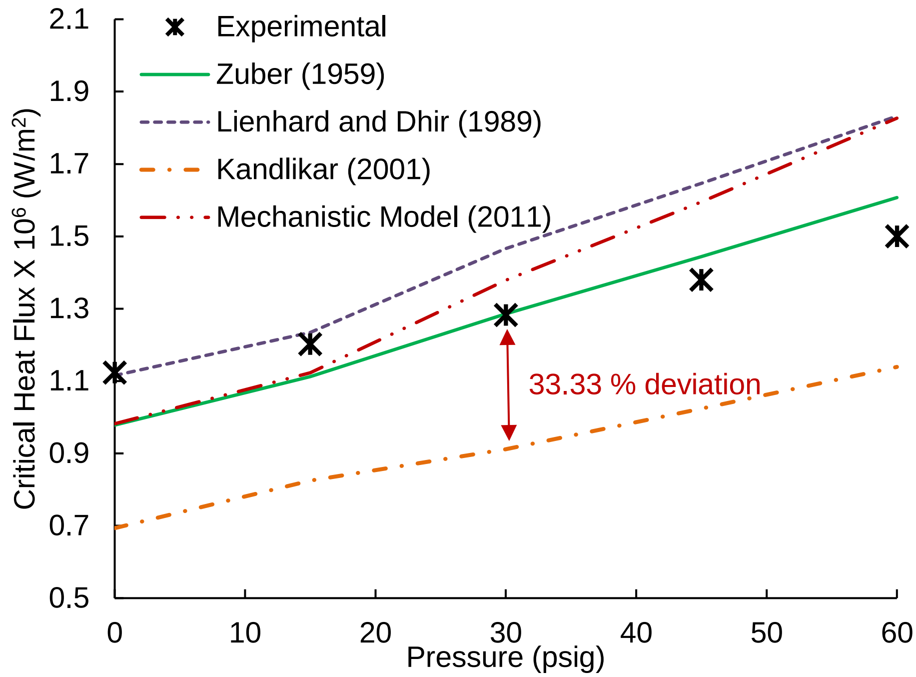

Figure 3.11 Compared CHF values from the different models at high-pressures [64]

The most widely used correlation for the CHF by Zuber [56] is expressed in Eq. (3.8) and is used to analyze the data.

$$q''_{CHF} = \Pi/24\, \rho_v{}^{1/2} h_{lv} [g\sigma(\rho_l - \rho_v)]^{1/4} \tag{3.8}$$

where, ρ_l and ρ_v are the densities of liquid and vapor respectively, h_{lv} is the latent heat of vaporization, g is the gravity, σ is the surface tension.

The CHF depends on the properties of water. The Zuber hypothesis is based on the high flux densities when excessive bubbles release from the heated surface in the form of vapor patch, leading to vapor explosions. At the interface, the surface experiences a rapid evaporation and forces the vapor upward to the fluid in the form of explosive jets. At this point, the boiling becomes unstable and reaches to a transition point from nucleate boiling to film boiling. The predicted CHF was 1.4 times higher than Zuber's predicted theory. Lienhard and Dhir [71] predicted that the critical flux value was 1.4 times of Zuber's value. Kandilkar [72] obtained the critical flux value considering the contact angle of liquid and the surface orientation is expressed in Eq. (3.9).

$$q''_{CHF} = 7.5 \left(\frac{1 + cos\,\phi}{16}\right)\left[\frac{2}{\Pi} + \frac{\Pi}{4}(1 + cos\,\phi)\,cos\,\theta\right]^{5} q''_{Zuber} \tag{3.9}$$

where, ϕ is the contact angle and θ is the surface orientation.

In recent studies, Guan et al [67] hypothesized a new mechanistic model based on how the vapor momentum flux at the macro-layer of the liquid, that lifts up from the heating surface, dries out the surface. Based on the theory, the critical heat flux for the horizontal surface is predicted as expressed in Eq. (3.10):

$$q''_{CHF} = 0.2445\,\rho_v h_{lv}\left[\frac{\sigma(\rho_l - \rho_v)g}{{\rho_v}^2}\right]^{1/4}\left(\frac{\rho_v}{\rho_l}\right)^{1/10} \tag{3.10}$$

The measured CHF is compared to the above predicted theories is shown in Fig 3.11.

The CHF is enhanced with increasing pressure. On the plain copper surface 110 W/cm^2, 120 W/cm^2, 122 W/cm^2, 130 W/cm^2 and 142 W/cm^2 of CHF was found at 0 psig (0 kPa), 15 psig (103. 4 kPa) , 30 psig (206. 6 kPa), 45 psig (310.2 kPa), and 60 psig (413.7 kPa) respectively. 85 W/cm^2 $\pm$ 15 W/cm^2 as reported by Li and Betz [73] at 0 psig (0 kPa). The CHF for high-pressure, best fits with the predicted CHF by Kandlikar [72]. Whereas, the estimated CHF by Zuber is under predicted for pressures less than 30 psig and over predicted for pressures greater than 30 psig. The Zuber's predicted CHF deviates at high-pressure with the experimental data. The CHF deviates by 33.33% from the Kandlikar model. The predicted CHF from Dhir's [71] theory exceeds with the experimental value.

At low pressure from 0 psig (0 kPa) to 30 psig (206.6 kPa), the lift off model deduced by Guan [67] is under predicted. As pressure increases, the lift off model over predicts the experimental data. All these variations can be justified with the predicted theory because the pressure has a huge impact on bubble dynamics. Zuber's model under predicts the experimental data because the model was applicable for a 40 degree contact angle. Previously, it was discussed in the bubble dynamics section, how the pressure effects the size of primary bubbles and frequencies.

At high heat flux it is hard to visualize the number of bubbles and their coalescing behavior, as different bubble dynamics may occur at high heat flux. The evaporation rate might be affected due to the decreasing size of bubbles and increasing number of nucleation sites. The heat could be deported to the liquid in the form of a vapor train or vapor patch. The formation of the thermal boundary layer and merging of vapor trains to the neighboring vapor trains may propagate a vapor explosion, resulting in the enhancement of CHF. At high-pressure the surface tension of the liquid also changes. None of the models captured the critical heat flux value at high-pressures. The study suggests the need for a new model which can capture the physics of the dynamic behavior of contact angle at high-pressure during pool-boiling.

Chapter 4 - A Theoretical Study of the Performance of High-pressure Pool-boiling with Increasing Contact Angles

4.1 Introduction

Despite extensive studies, the combined effect of high-pressure and surface wettability has not been well studied and understood. This chapter discusses a fundamental understanding of the critical role of dynamic surface wettability on bubble dynamics and boiling performance. The theoretical results of high-pressure pool-boiling performance on hydrophobic surfaces at high-pressures have been presented in this chapter.

4.2 Surface Preparation and Characteristics

The steps for Teflon solution preparation are based on [73]. Teflon© solution is prepared in proportion of 1 part of the Teflon AF solution with 24 part of refrigerant FC-40. A polished copper surface is coated with the Teflon© solution using dip coating. The thickness of the Teflon© coating depends on the number of dips and the ratio of the solution.

Before the surface treatment, the copper surface is cleaned with an Isopropanol solution and kept in an ultrasonic cleaner for 20 minutes. After the cleaning is performed, the copper surface is dipped in the solution, and dried at ambient condition. The Teflon© coated surface is baked in the oven for 165°C for 24 hours.

The static contact angle for the Teflon© coated copper surface is measured using a goniometer. The contact angle for the plain copper surface is 68.34° and for the Teflon© coated surface is 114.85° as shown in Fig 4.1. The Teflon© coated surface exhibits a higher contact angle due to the low adhesive force.

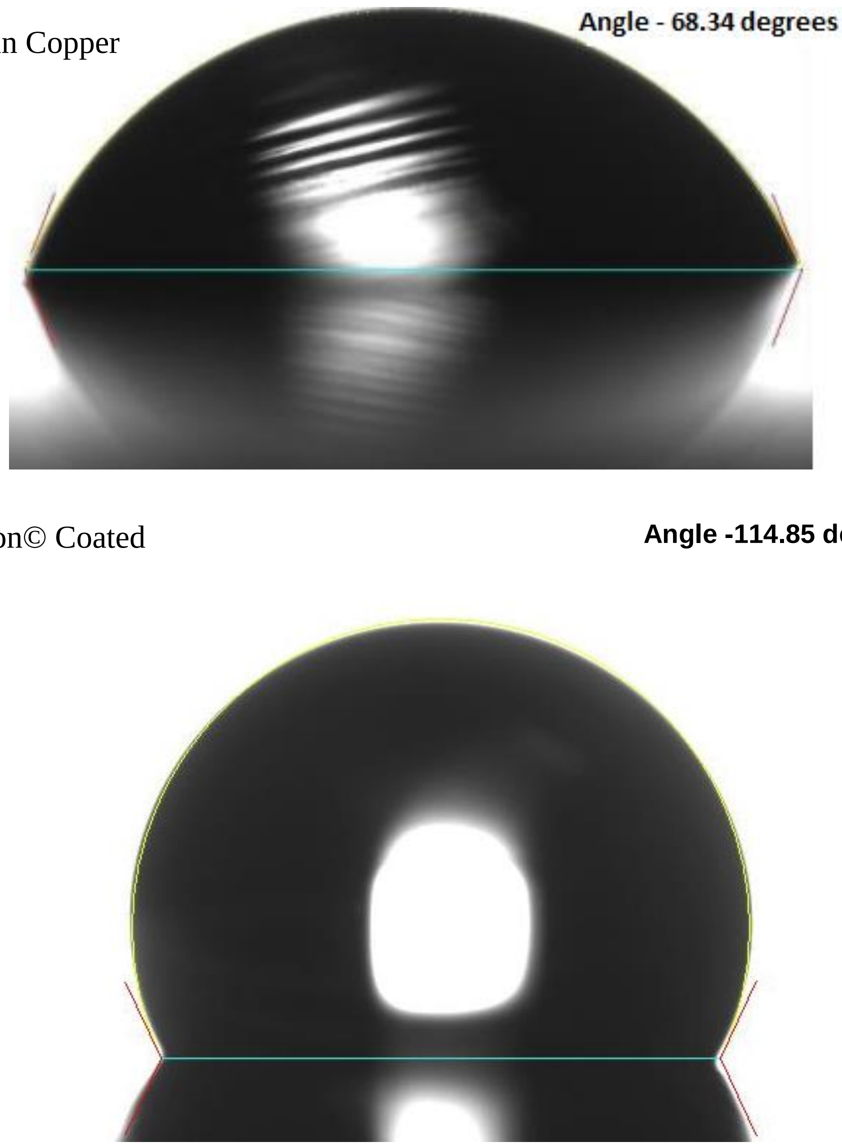

Figure 4.1 The static contact angle of water on the plain copper surface and the Teflon coated surface.

The Teflon© coating layer adds a layer of thermal resistance to the surface. Due to the thermal resistance, the temperature is lowered. At 50 W/cm^{2,} the temperature drop was measured to be 0.657 K using the heat conduction equation expressed in Eq (4.1).

$$\Delta T = \frac{q''L}{k\,A} \tag{4.1}$$

where, ΔT is the temperature difference, q'' is the heat flux, L is the thickness of the Teflon© coating, k is the thermal conductivity of the coating, and A is the total coated surface area.

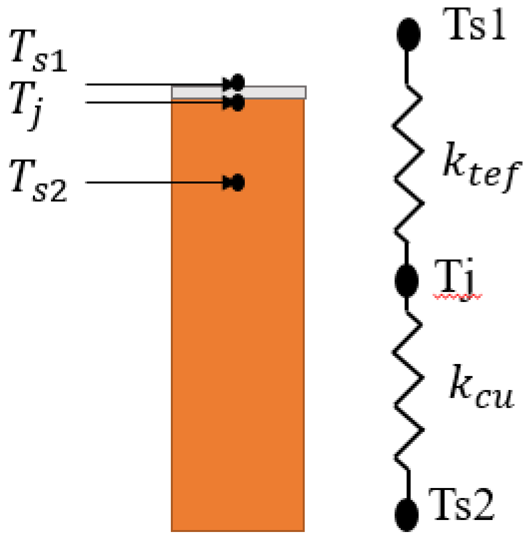

Figure 4.2 The configuration of Teflon coated copper surface with nomenclatures. T_{s1}, T_j, and T_{s2} are the surface temperatures. k_{tef} and k_{cu} are the thermal conductivity of the Teflon© coating and the copper surface respectively.

The total heat flux is determined using the conduction heat transfer equation with total effective thermal conductivity, given by Eq (4.2). The schematic of the thermal network is shown in Fig 4.2.

$$\frac{1}{k_{tot}} = \frac{1}{k_{cu}} + \frac{1}{k_{tef}} \tag{4.2}$$

where, k_{tot} is the total thermal conductivity, k_{cu} is the thermal conductivity of copper and k_{tef} is the thermal conductivity of Teflon©.

$$k_{tot} = \frac{k_{cu}k_{tef}}{k_{cu} + k_{tef}} \tag{4.3}$$

4.3 Results and Discussion

This section presents the analytical results for the bubble dynamics and the performance of pool-boiling heat transfer at high pressure for the Teflon© coated surface. The experimental results are also compared with the analytical results in the later section.

4.3.1 Bubble Dynamics: Bubble Departure Diameter

The bubble departure diameter and departure frequency were determined using the Fritz correlation, expressed in Eq. (1.4) and (1.6) respectively. Fig 4.3 shows the bubble departure diameter in mm for three different pressures. The bubble departure diameter was calculated based on the Fritz model by balancing surface tension and buoyancy forces. The departure diameter of a bubble is plotted as a function of varying contact angle for three different pressures as shown in Fig 4.3. The result shows that the departure diameter decreases with pressure. At 100° of contact angle, the departure diameter decreases by 3-4%.

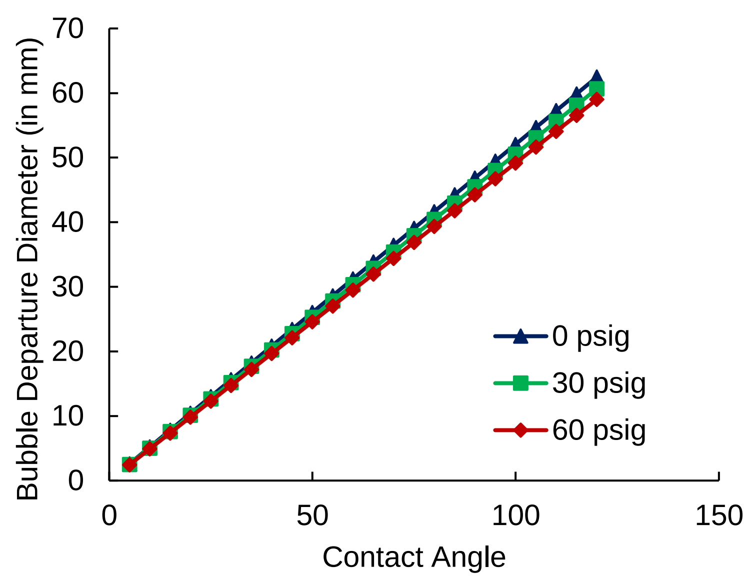

Figure 4.3 The departure diameter as function of contact angle for a plain surface at high-pressures.

At lower wetting angle the changes are negligible. In comparison to higher contact angles, the bubble departure diameter is larger than the lower contact angle surface. For example, for 0 psig (0kPa) the bubble departure diameter is 22 mm at 50°. On the other hand, for the contact angle 100°, the departure dimeter is 48 mm. The difference in the bubble departure diameter can be related to the surface energy.

4.3.2 Bubble Release Frequency

Based on Zuber's model, the departure frequency is inversely proportional to the departure diameter. The departure frequency is calculated based on the equation expressed in Eq. 1.6. The equation was derived from the critical velocity required to obtain Kelvin-Helmholtz instabilities as discussed in Chapter 1. The bubble departure frequency is drawn as a function of contact angle. The results show that the bubble release frequency decreases with varying contact angle. This can be related to the change in surface tension associated with the surface properties of the Teflon coating.

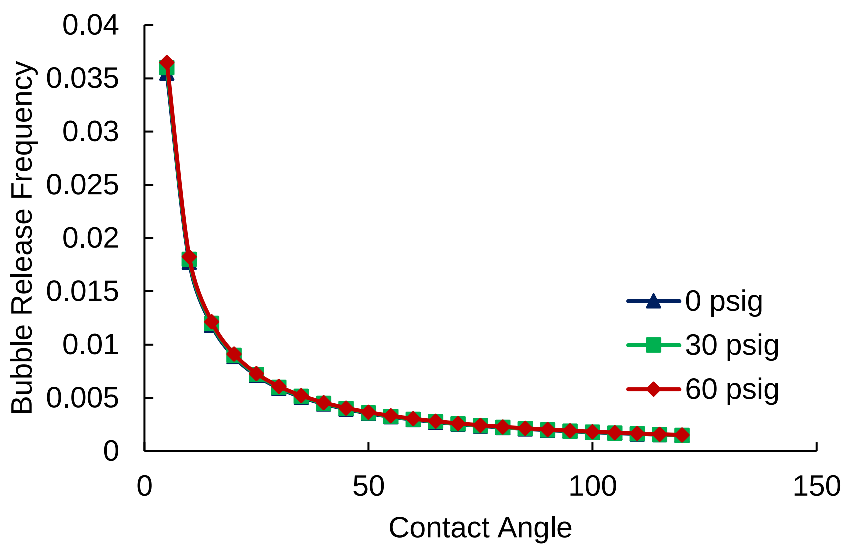

Figure 4.4 The departure frequency as function of contact angle for a plain surface at high-pressures.

The low surface energy promotes nucleation due to the less energy requirement, which helps in increasing active nucleation sites. Also, the pressure increases the bubble departure frequency that can be related to change in the thermodynamic properties of the water at high-pressure.

4.3.3 Nucleation Site Density

The active nucleation site density is determined based on Hsu's theory. The range of active nucleation sites was drawn as a function of superheat using the Hsu' correlation. Using the plots, the size range of active nucleation sites can be estimated. The results were plotted for three wetting angles at different pressures. The effect of wettability on the size range of active nucleation site can be seen in Fig 4.5. The size range of active nucleation sites shifts from 8 μm – 1 μm at 0 psig (0kPa). It also decreases the wall superheat. The bubble nucleates at a lower wall superheat, which shows that nucleation requires less energy. The results suggest that the changes in the wetting angle significantly affect the number of active nucleation sites with wall superheat. The high-pressure results also exhibits that pressure decreases the wall superheat by three folds and the range of nucleation size by two orders of magnitude.

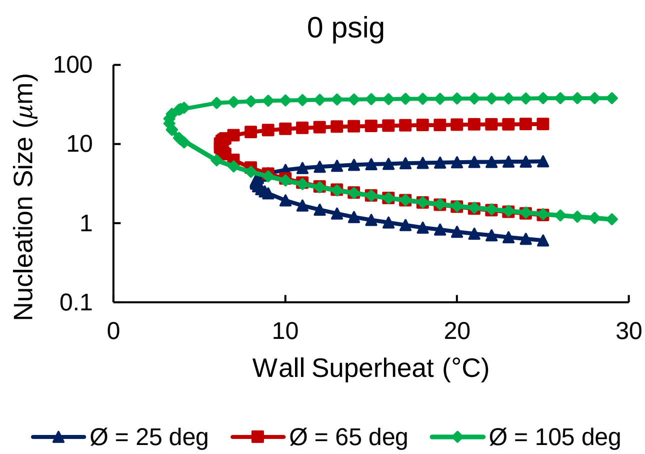

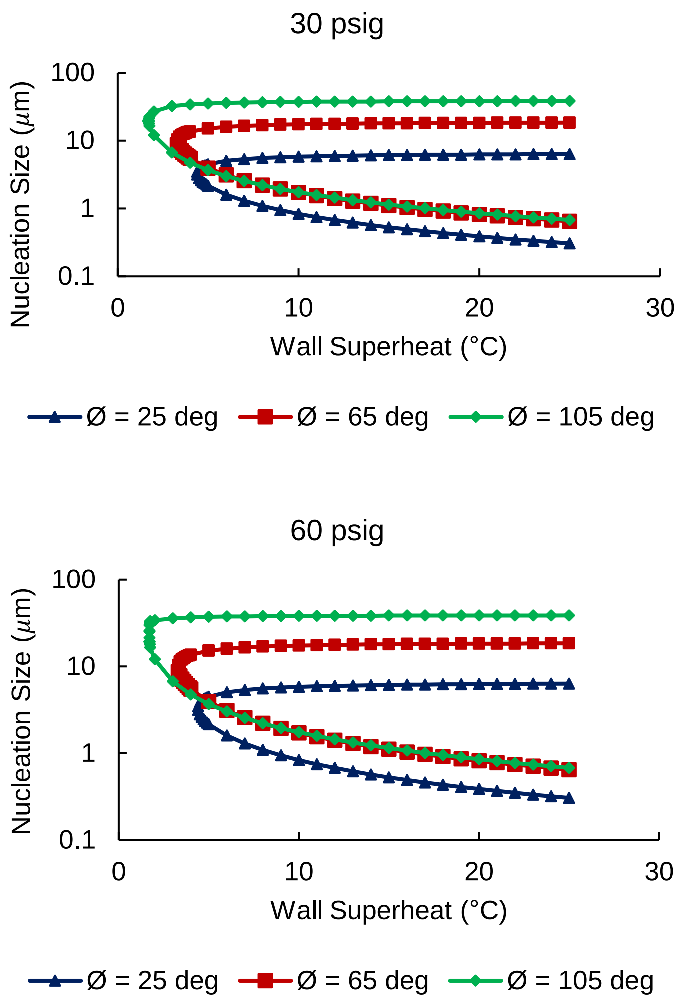

Figure 4.5 The size range of active nucleation sites for three wetting angles at three different pressures

4.3.4 Heat Transfer Performance

The heat transfer performance is determined using the equation expressed in Eq. (1.7). The HTC depends on departure diameter, bubble release frequency and the active nucleation site densities. As it is discussed in the previous section, the pressure and the contact angle both influence the boiling parameters. The HTC results shown in Fig 4.6, suggest that the surface modification induced by changing the wetting property enhances the boiling performance from 0.001 to 100 in three orders of magnitude.

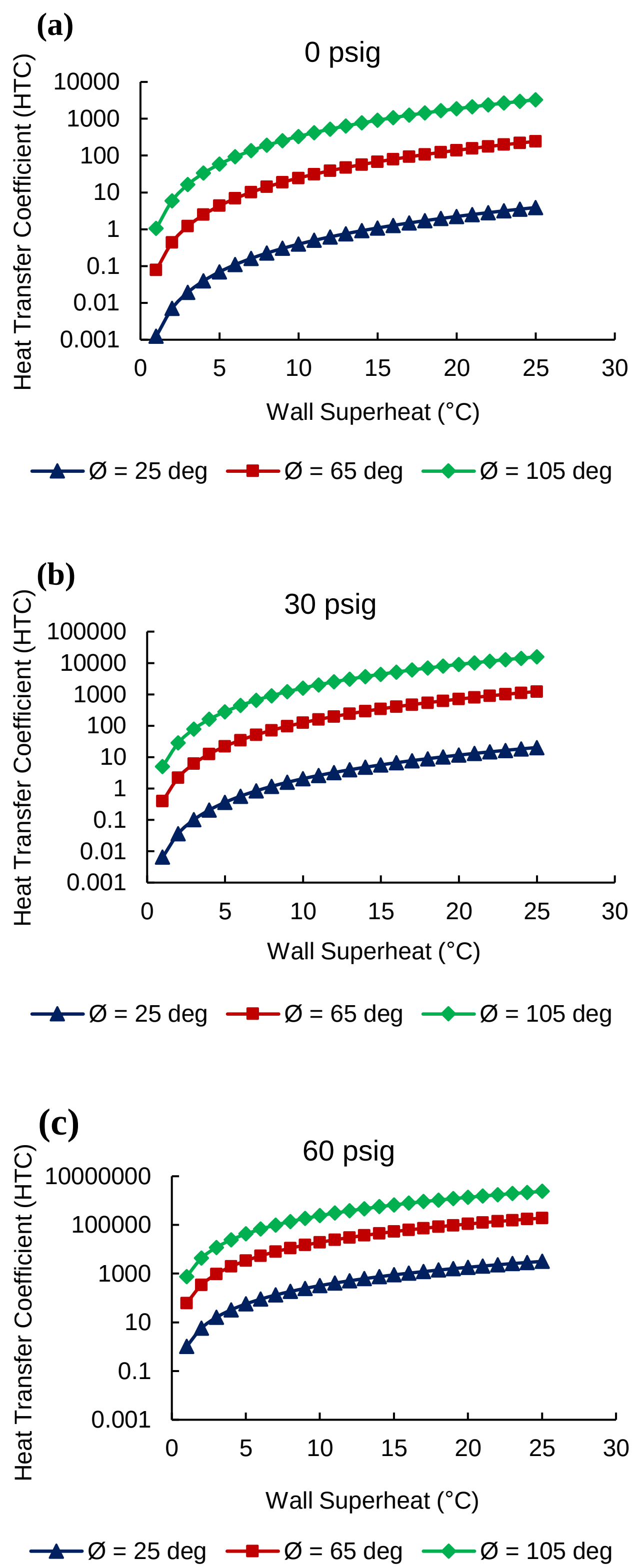

Figure 4.6 The high-pressure pool-boiling HTC results for different wetting angles (a) 0 psig (b) 30 psig and (c) 60 psig

The pressure further amplifies the performance of pool-boiling heat transfer that can be related to the lower wall of superheat and the number of bubble nucleates at the low heat flux.

4.4 Experimental Results

The high-pressure pool-boiling test results on a hydrophobic Teflon© coated surface is shown in Fig. 4.7. The results are compared with a plain surface for water. The boiling curves for 30 and 45 psig are shown in Fig.4.7. The CHF was not reached in these tests. The high-pressure pool-boiling test results show an enhancement for the plain surface which was already discussed in Chapter 3. The boiling curves for the Teflon coated surface shift to the left with the pressure. The trend lines for both surfaces indicate that the heat transfer improves with the pressure. The slope of the Teflon coated surface for high-pressure is higher than the plain copper surface. At 10 K of wall superheat, the heat flux is two times higher than the plain surface for 30 psig. The heat transfer enhances further at high-pressure, 45 psig. The heat transfer improvement with the pressure can be related to the increased number of bubble nucleation, decreased bubble departure size and the increased departure frequency.

The pressure also affects the wall superheat. The boiling onset for high-pressure data is significantly smaller than the plain copper surface. For example, at a heat flux of 50 W/cm^2 the wall superheat reduces by 35% and 45% for 30 psig and 45 psig, respectively. The changes in the wall superheat can be related to the size of the departure bubbles and the thermal conductivity of the Teflon coating. It is observed from the boiling videos, the Teflon© coated surface promotes nucleation at a low wall superheat and transfer heat through a larger bubble.

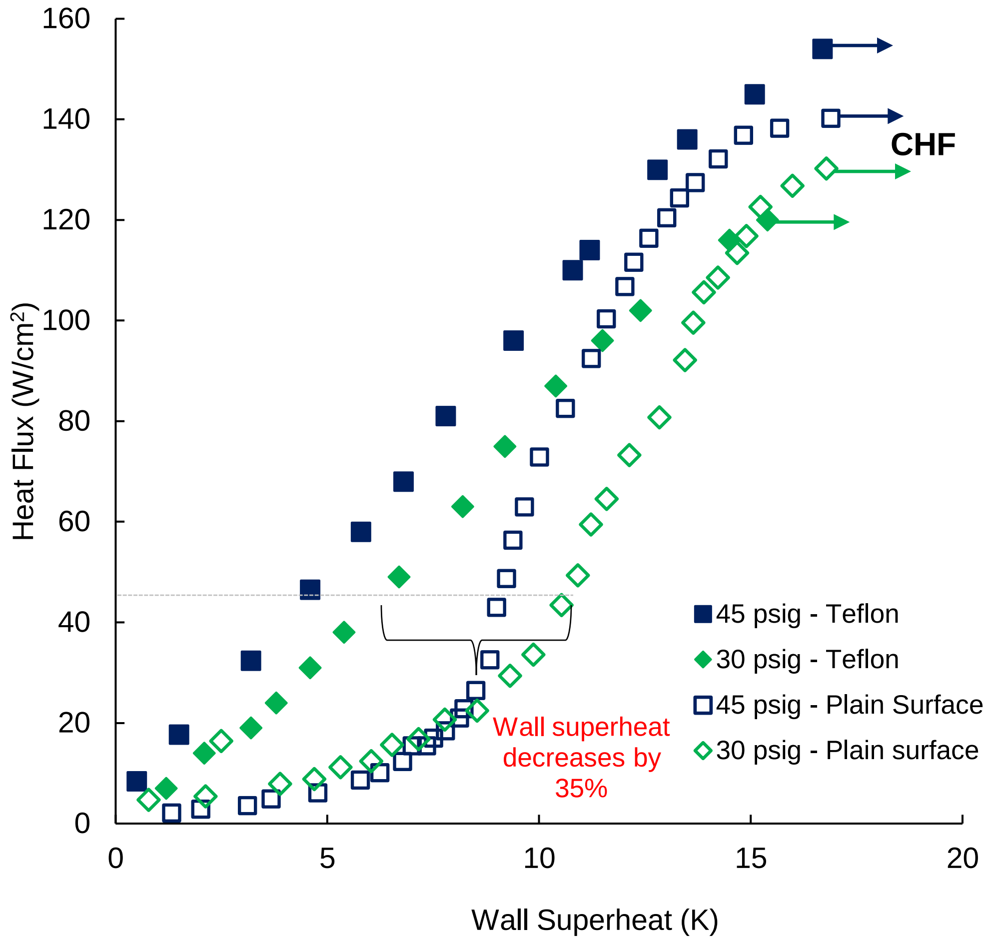

Figure 4.7 High-pressure pool-boiling curves of Teflon© coated surface and Plain surface

The heat transfer performance is compared for both the surfaces using the HTC curves as shown in Fig 4.8. The performance curve is shown as a function of the heat flux. For the Teflon© coated surface, the maximum heat transfer coefficient is found to be 10 W/cm^2.K for 45 psig at 50 W/cm^2. Further increase of heat flux, a negligible effect is noticed in the HTC curve. The reason could be the saturated bubble departure size due to the pressure and surface wettability effect. In comparison to the plain surface, the HTC for the Teflon© coated surface is 100% higher for 45 psig. The results indicate that the surface wettability has a higher impact than the fluid property change due to pressure effect at low heat fluxes. On the Teflon coated surface the bubble departure size was found 1.4 times larger than the plain copper surface, which can be related to the decreased wettability of the hydrophobic surface. In conclusion, the enhanced HTC for the Teflon© can be related to the bubble departure size and number of active nucleation sites.

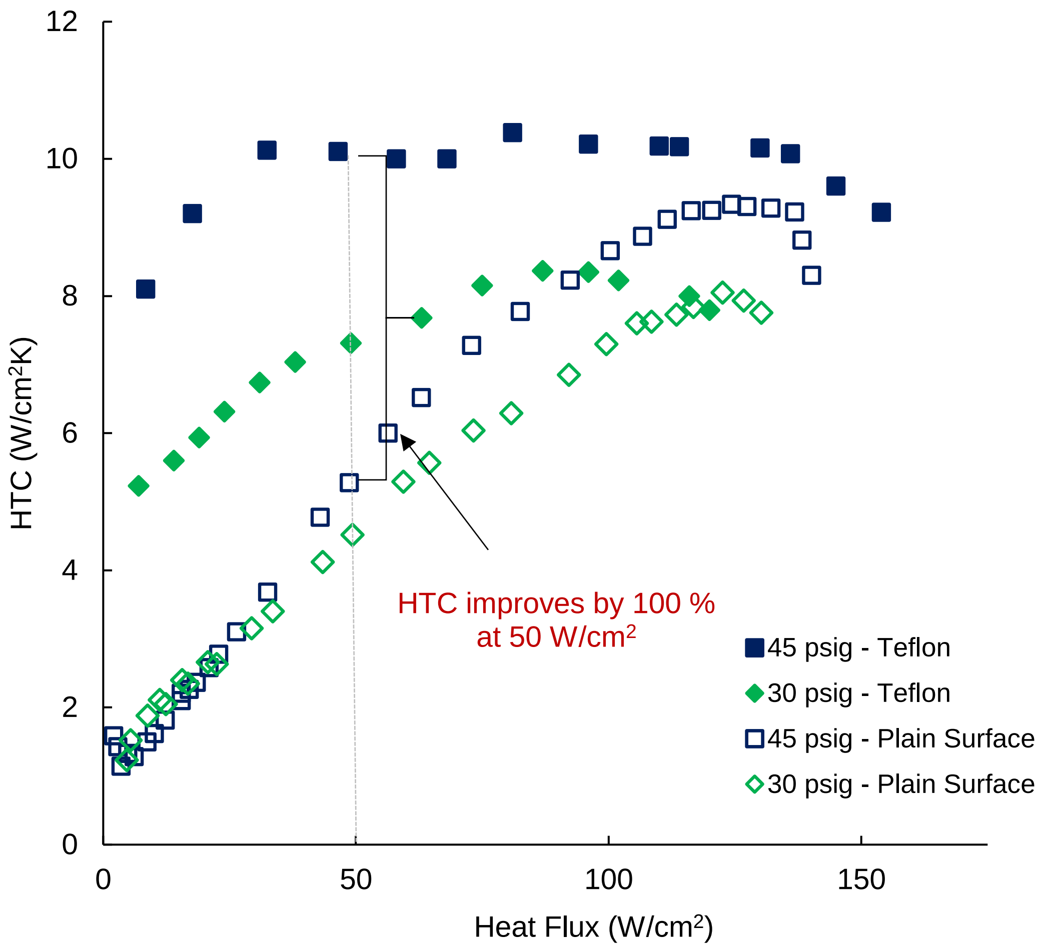

Figure 4.8 Heat transfer performance of Teflon© coated surface and Plain surface

Chapter 5 - High-pressure Pool-boiling Performance on Sintered Wicks

5.1 Introduction

In this chapter, we explore the impact of pressure on the performance of pool-boiling heat transfer using 200 μm copper sintered particle wick structures. The objective of this chapter is to understand the boiling behavior associated with the high-pressure due to the wick structure. The bubble dynamics have been studied at varying pressure forthe wick structure. The mechanism for the enhancement is explained in the results and discussion in the later sections.

5.2 Materials and Methods: Sintered Particle Wick Structure

5.2.1 Fabrication Method

The wick structures are provided by Wichita State University. A detailed key approach for the sintering process is illustrated in Fig 5.1 [35]. The wick structure is fabricated by using commercially available copper powder. A 2.54 cm long copper rod is machined for the wick fabrication. The copper rod is finished smoothly using sand paper and cleaned using isopropanol solution before sintering. A layer of copper powder of a desired thickness is sintered on the commercially available copper rod of 1 cm in diameter and 2.54 cm long. A stainless steel based inverted mold is designed for the wick layer with a $\pm$25 μm tolerance limit. Before the sintering, a thin layer of carbon powder is applied to avoid any copper particles sticking to the mold surface. The copper rod is perfectly inserted into the mold. The copper power is spread uniformly on the top of the polished copper rod. The entirely assembly of the inverted mold and the copper powder is kept in a furnace filled with Argon gas flow with 50 sccm (standard cubic centimetre per minute) for two hours at 950°C. The fabricated wick is allowed to cool down naturally in the ambient temperature with a cooling rate of 5 -10 °C per minute. The same procedure is applied for the three layer wicks of different copper powder size. A different size of the copper powder is used in fabricating the wick. The top view of the fabricated wick of the 200 µm size of the copper particles is shown in Fig 5.1.

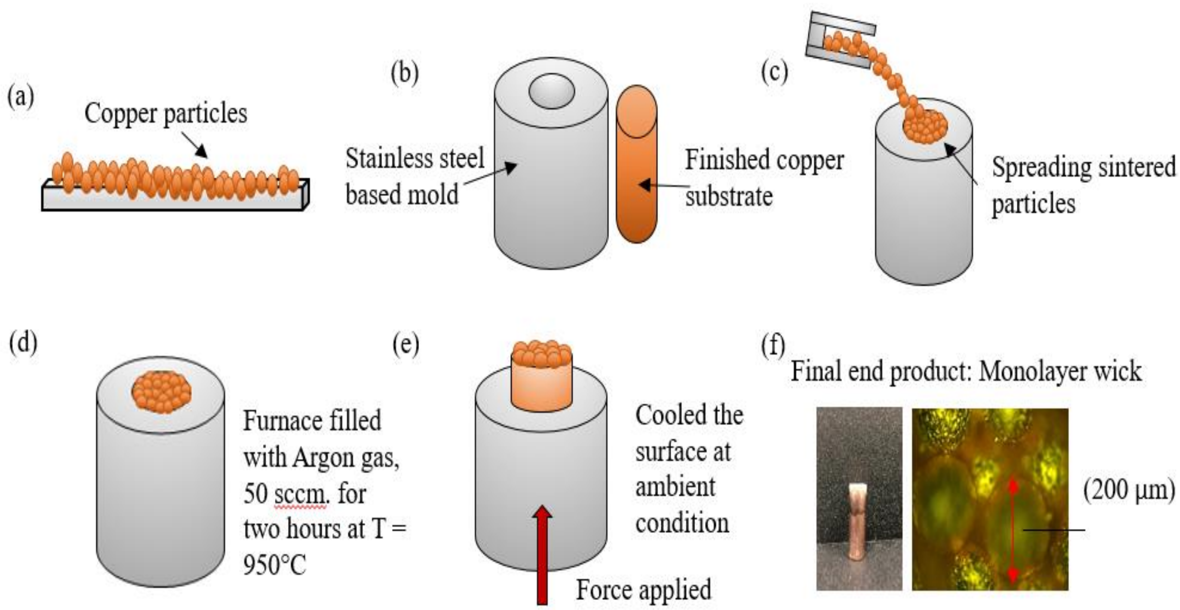

Figure 5.1 The schematic of the sintering process of the monolayer sintered wick surface. (a) 200 µm copper particles are used for the monolayer sintered wick surface (b) A cylindrical stainless steel based mold is machined to fabricate the sintered wick on the finished copper substrate (c) Particles are poured uniformly in the mold cavity (d) The poured particles are kept in the furnace filled with argon gas for two hours at 950°C. (e) The wick is cooled at ambient condition and released from the mold (f) The fabricated monolayer wick on the cylindrical copper substrate and the microscopic image of the wick are also shown.

The same fabrication process has been followed for fabricating the wick layers of layered wick structures. Table. 5-1 includes the properties of the wick layers featured with the particle size, number of layers, thickness and porosity. The porosity of all the wicks is maintained at 0.45. After the sintering process, samples are tested under a confocal microscope to inspect the particles arrangements.

Table 5-1 List of the sintered copper powder samples and their geometric properties

Sample	Particle diameter	No. of Layer	Thickness (in µm)
A	100	1	100
B	100	3	300
C	200	1	200
D	200	3	600
E	300	1	300
F	300	3	900
G	100/200	1	300
H	550	1	550
I	550	2	550

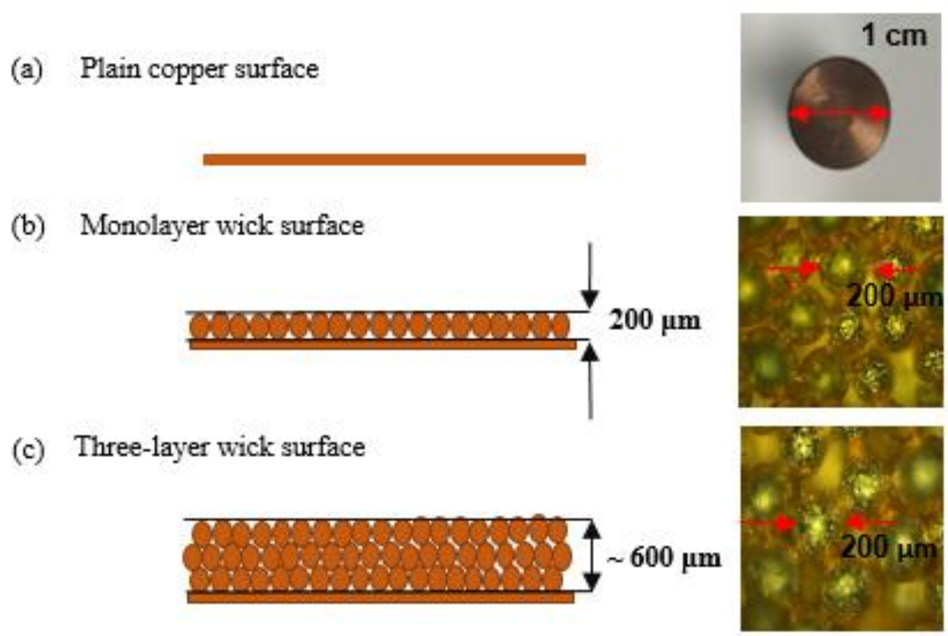

Figure 5.2 The side and top view of boiling test surfaces (a) Plain copper surface (b) Monolayer wick surface and (c) Three-layer wick surface. The top view is the microscopic view of the sintered particle wick surfaces at 350 X zoom.

5.3 Surface Characterization: Surface Features

The pool-boiling experiment is performed on the plain copper and wick structure of different particle sizes. The sintered wick structures are examined using a confocal microscope. The top view of the single-layer wicks of particle size 100 and 200 μm are shown in Fig 5.3. The images are investigated to examine the packing arrangements of sintered particles in the wick structure. The sintered particles are packed in a hexagonal arrangement as shown in Fig. 5.3 for the 100 μm sintered particle. The particles are well jointed with the neighboring particles.

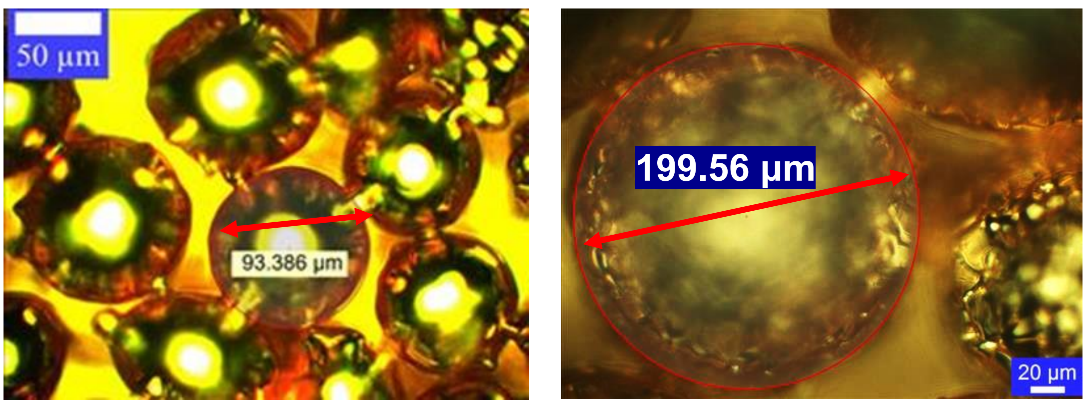

Figure 5.3 Top view of the sintered wick of particle size (a) 100 and (b) 200 μm.

5.3.1 Contact Angle Measurements

The static contact angle is measured using a goniometer. The contact angles of the wick of particle size, 200 μm and the plain surface are 100.96° and 80.52°, respectively as shown in Fig. 5.4, showing that the wick increases the contact angle by 25%. Wettability tests are also carried out for the other three surfaces. The measured contact angles are shown in Fig. 5.4(a). The plain copper surface shows a moderate contact angle change, 83.84° to 98.47° as the volume of water droplet increases from 1 μl to 5 μl. However, the wick surface significantly changes the contact angle as the volume of water increases. It indicates that the gravity/capillary-driven water imbibition in the wick surface plays an important role. The wick surface was kept at 125°C for 48 hours in the oven to oxidize the surface and the contact angle was measured again. After the surface treatment, the contact angle is found to be 98.53°.

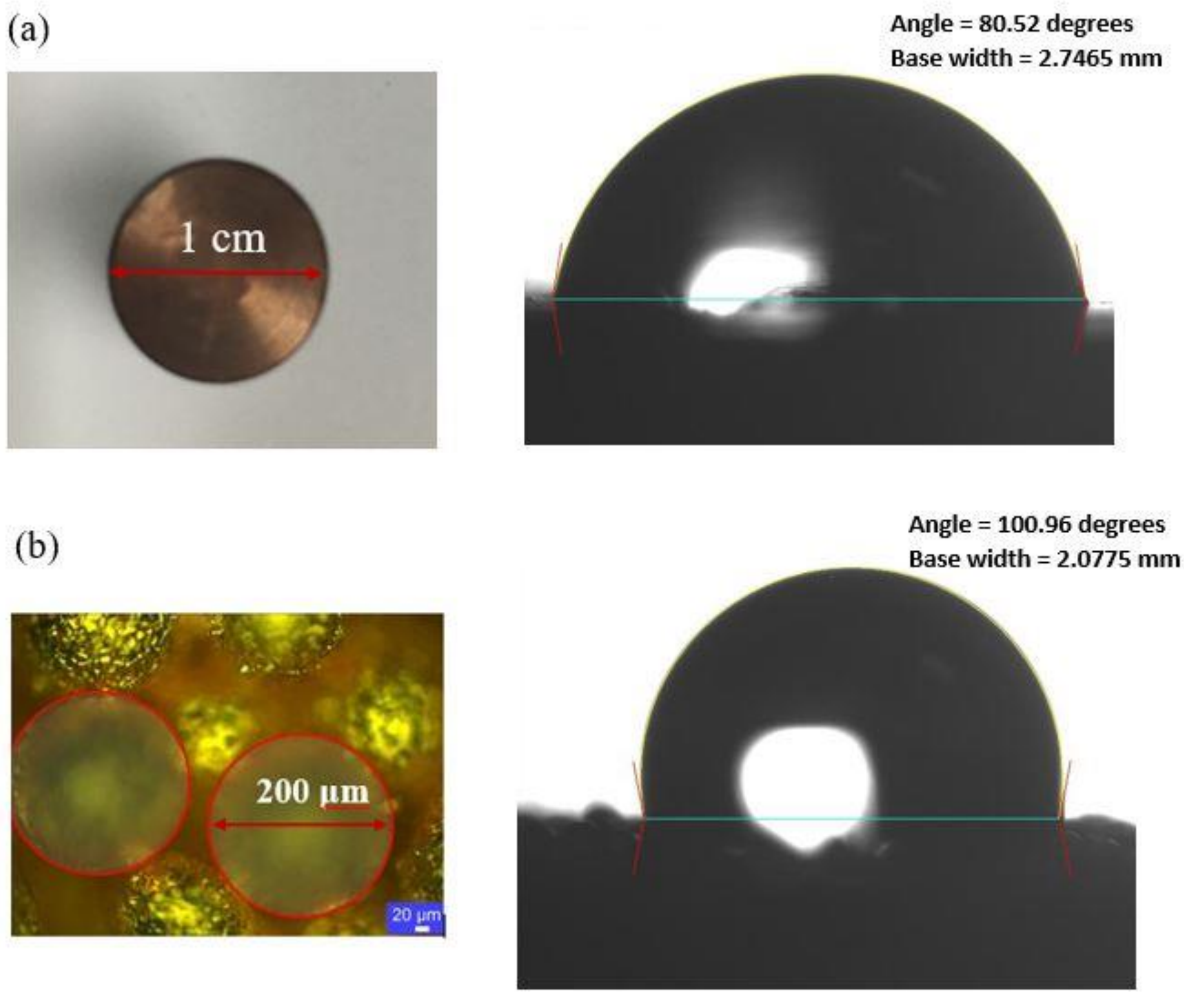

Figure 5.4 The zoomed top view of copper substrates and the contact angle measurement using the Goniometer. (a) The smoothed polished copper surface of diameter ~1 cm with contact angle 80.52 degree and (b) the mono layer wick structure of 200 µm sintered copper particles with contact angle 100.96 degrees. The base width of the bubble is also shown.

5.4 Results

The high-pressure pool-boiling results are shown in Fig. 5.5, which compares the boiling performance of the plain copper surface to the surface featuring with the sintered particles of 200 μm wick surface. The results are shown for the single-layer wick surface for three different high-pressures: 0 psig (0 kPa), 15 psig (103.4 kPa), and 30 psig (206.8 kPa). The boiling curve is drawn for the heat flux q´´, and degree of superheat $\Delta T = T_s - T_{sat}$ as shown in Fig. 5.5.

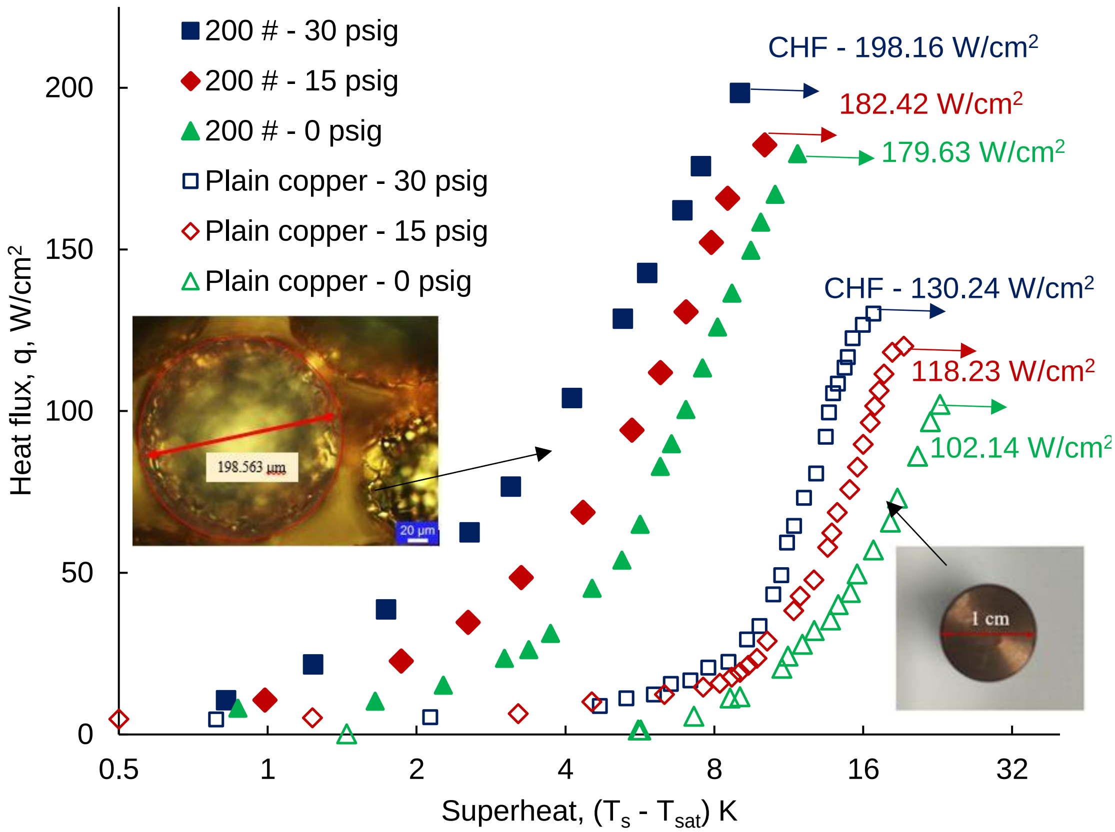

Figure 5.5 The high-pressure pool-boiling curves for plain copper surface and 200 micron monolayer wick surface for three different gauge pressures: 0 psig (0 kPa), 15 psig (103.4 kPa), and 30 psig (206.8 kPa). The critical heat flux is for each pressure is highlighted with a right headed arrow.

For the plain copper surface, a CHF 102.14 W/cm^2 is found at ΔT = 22.87K, which agrees with the previous work, found to be 85 W/cm^2 at 28 K, within the uncertainty, ±15 W/cm^2 [58]. The difference in the CHF can be related to the different surface roughness. For the plain copper surface, the critical flux values are 118.23 W/cm^2 and 130.24 W/cm^2 at 15 psig (103.4 kPa), and 30 psig (206.8 kPa) respectively. Li and Betz, 2017 reported pool-boiling results at high-pressure on the graphene oxide coated surface with critical heat flux values 80 W/cm^2, 90 W/cm^2, and 105 W/cm^2 at 0 kPa , 103.4 kPa, and 206.8 kPa respectively [39]. The enhanced CHF at high-pressure was reported due to the change in the bubble dynamics and pinning mechanisms at high-pressure pool-boiling. At high-pressure the properties of water i.e, the specific volume of liquid and the latent heat of vaporization decrease. The effect of change in the properties of water was observed in the bubble departure size and the bubble departure frequency, which influence the boiling performance [64]. A 46% reduction in the bubble size was found from the 0 psig (0 kPa) to 90 psig (620.5 kPa) with 10 - 12 % of an error margin. Further enhancement in the CHF and the degree of wall superheat are found in the monolayer wick structure. The boiling curves for the wick structure shown in Fig. 5.5 are steeper than the plain copper surface. The measured critical heat flux for the monolayer sintered wick structure is 179.63, 182.42, and 198.16 W/cm^2 at 0 psig (0 kPa), 15 psig (103.4 kPa), and 30 psig (206.8 kPa), respectively. For the monolayer wick, the maximum heat flux, 198.16 W/cm^2 is obtained at 9.89 K of superheat for 30 psig (206.8 kPa). At the gauge pressure of 0 psig (0 kPa), the CHF is 1.75 times higher for the wick surface as compared to the plain copper surface at 0 psig (0 kPa). A significant reduction in the degree of superheat is noticed in the monolayer wick at the given heat flux compared to the plain copper surface. For the wick surface, the maximum heat flux is obtained at ΔT = 9.87 K at 30 psig (206.8 kPa). Whereas, the maximum heat flux is obtained for the plain copper at 28.79 K. The degree of wall superheat is relatively smaller than the plain copper surface, which enhances the HTC. Twenty-percent enhancement in the CHF was reported in the CHF value for the wick structure (200 μm wick) for n-pentane [50]. The low wick superheat was related to the increased effective thermal conductivity. In the boiling curve, the boiling onset is as important as determining the CHF. The HTC is determined with a ratio of heat flux and the wick superheat. Fig. 5.6 and Fig. 5.7 show the HTC as a function of the superheat and the heat flux, respectively.

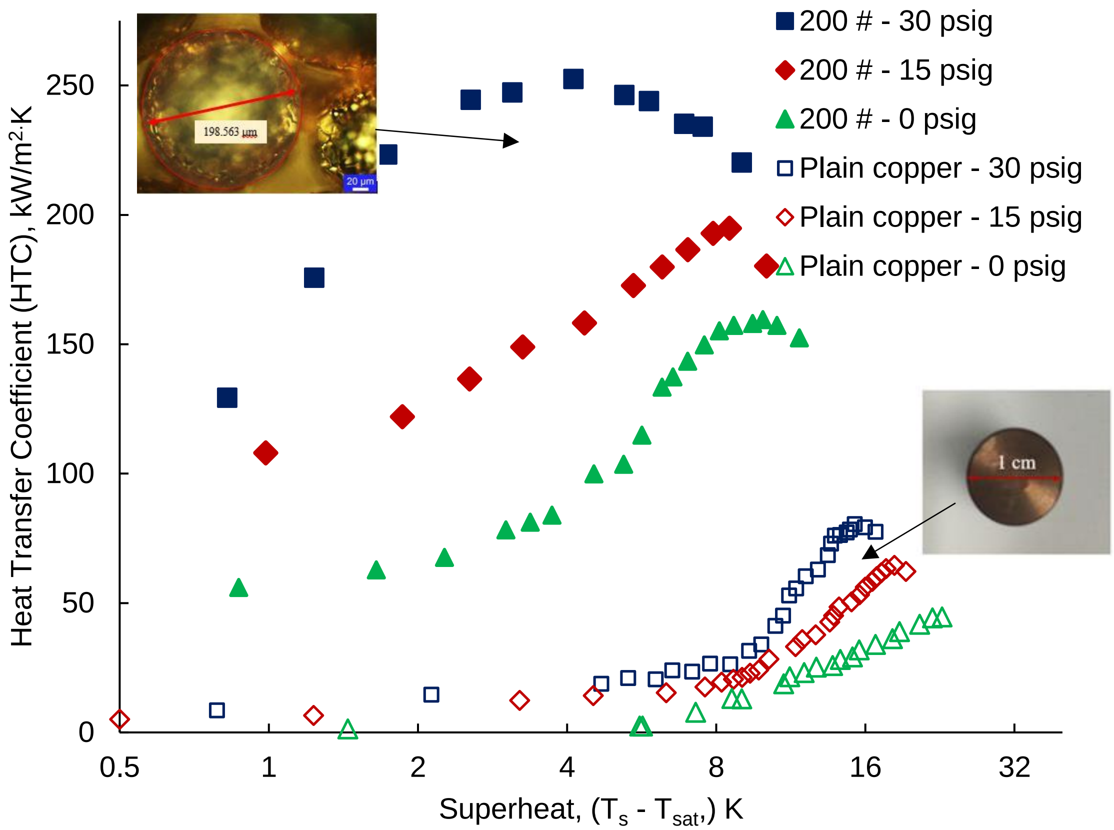

Figure 5.6 The heat transfer performance of high-pressure pool-boiling data for three different gauge pressures: 0 psig (0 kPa), 15 psig (103.4 kPa), and 30 psig (206.8 kPa).

The cumulative effect of the surface modification of the wicking layer and increasing pressure further enhances the HTC. For the plain copper surface, the heat transfer performance curve exhibits enhancement by 75 % at 30 psig (206.8 kPa) compared to 0 psig (0 kPa). The maximum HTC is observed at a degree of wall superheat around 6 K and 28 K for the wick surface and the plain surface, shown in Fig. 5.6. The wick layer reduces the degree of superheat significantly. The maximum HTC, 252.46 kW/m^{2}K is observed for the heat flux at 100 W/cm^2 at 30 psig (206.8 kPa) shown in Fig. 5.6. The heat transfer performance is enhanced by 100% at 30 psig (206.8 kPa) compared to 0 kPa.

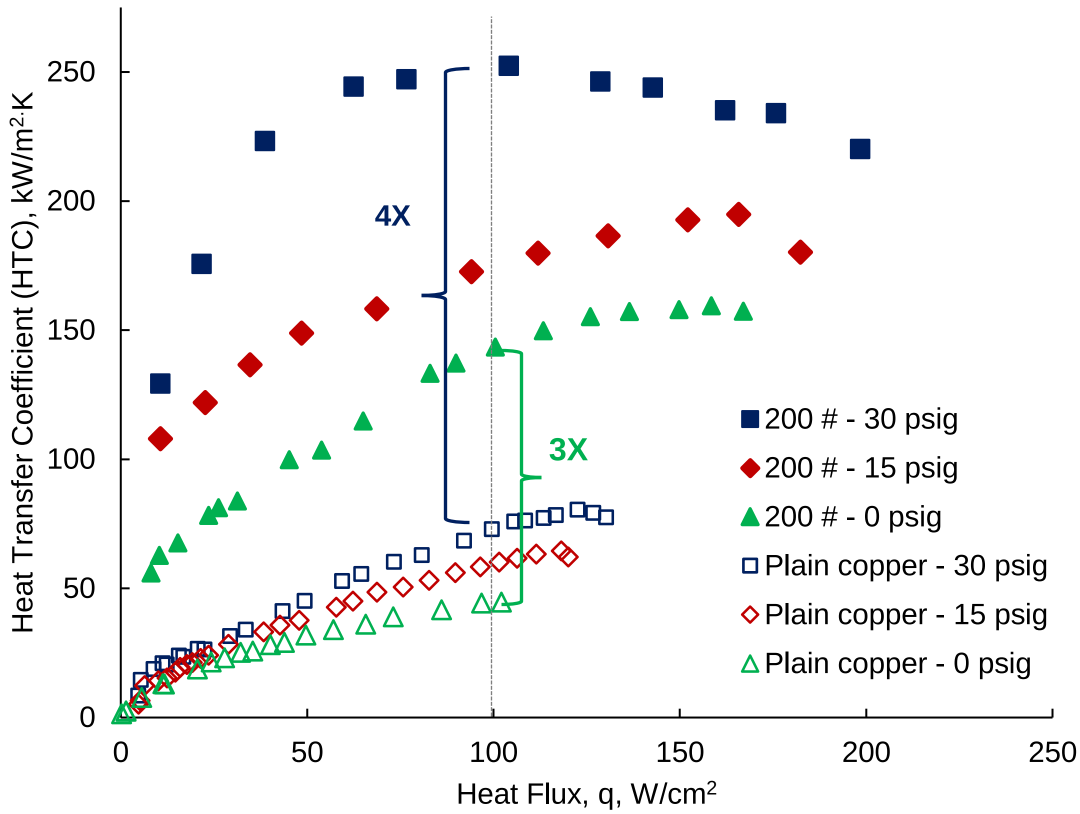

Figure 5.7 the heat transfer performance of high-pressure pool-boiling for three different gauge pressures: 0 psig (0 kPa), 15 psig (104.5 kPa), and 30 psig (206.8 kPa). Heat transfer coefficient in kW/m²K verses Heat flux (q'') in W/cm².

The enhancement is obtained due to the low superheat and a different boiling behavior which is explained in the next section. At high heat flux, the HTC further decreases. For the other two pressures 0 psig (0 kPa) and 15 psig (130.4 kPa), the maximum HTC is found approximately 145 kW/m² K and 195 kW/m² K at 150 W/cm² of heat flux shown in Fig. 5.7. It can be related to a change in the boiling behavior at higher pressure. Fig. 5.8 shows the boiling images of the wick surface at different heat fluxes for the two pressures. Fig. 5.8(1a) – (1f) show the recorded boiling images for 0 psig (0 kPa) and Fig. 5.8 (2a) – (2f) show the boiling images for 30 psig (206.8 kPa).

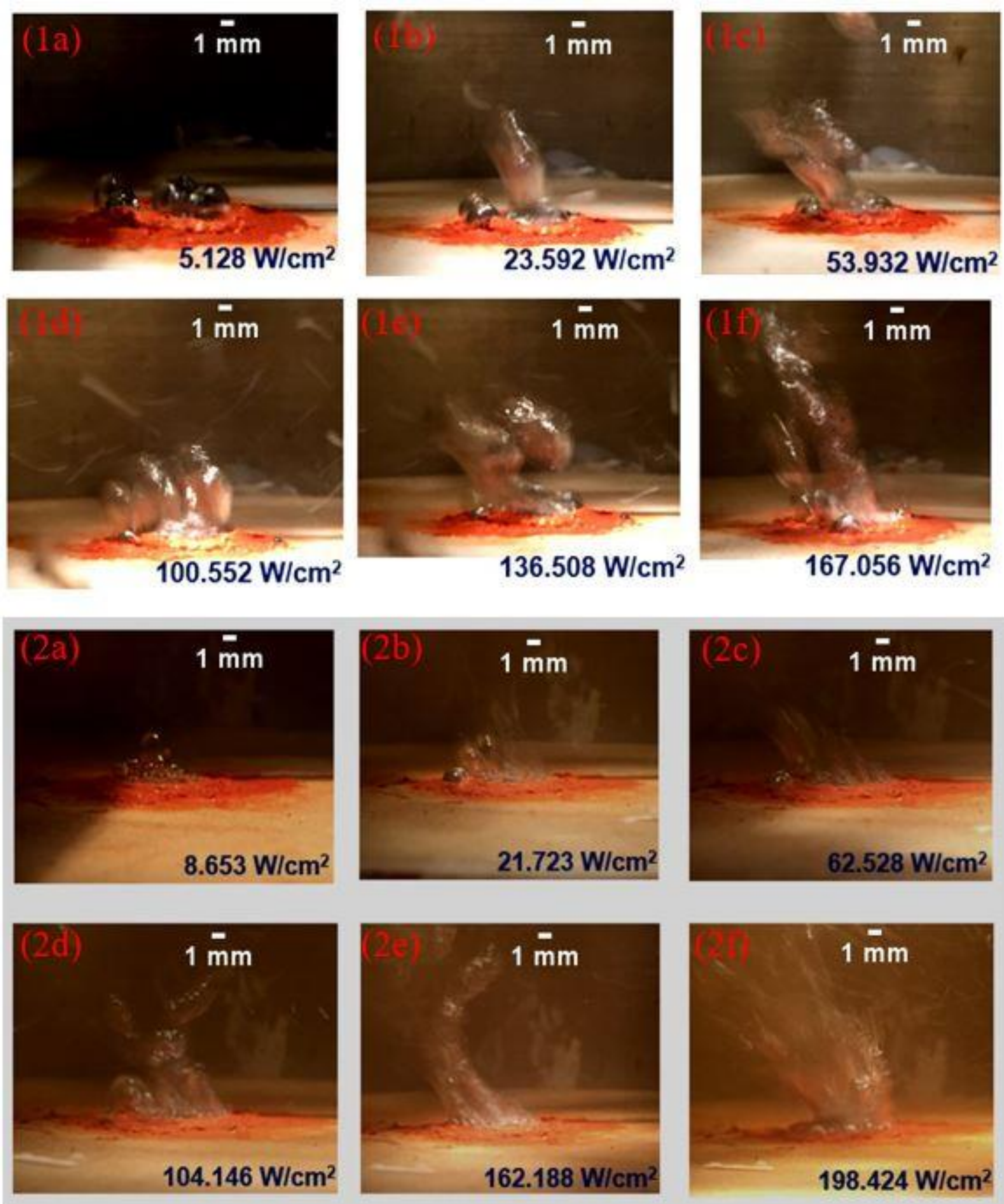

Figure 5.8 The recorded nucleate pool-boiling images for the 200 μm mono layer wick structure are shown in 1(a) – 1(f) at 0 psig (0 kPa) at different heat fluxes. The high-pressure boiling images at 30 psig (206.8 kPa) for the monolayer wick are shown in 2(a) – 2(f) for different heat fluxes

For the wick surface bubbles begin nucleating at heat fluxes of 5-10 W/cm^2 and a degree of superheat of 0.5-1.0 K, which is similar to the plain copper surface [58]. The bubble departure size is approximately 3 mm as shown in Fig 5.8(1a). The nucleate boiling is observed up to the heat flux value of 100 W/cm^2. The results suggest that the boiling on the wick stretches the nucleate boiling region for a longer duration. At heat flux greater than 100 W/cm^2, the nucleating bubble starts merging with the neighboring bubbles, leading to boiling in the form of slugs or columns, see Fig. 5.8. The effect of pressure on the bubble size is observed in the boiling images at 30 psig (206.8 kPa) as shown in Fig. 5.8 (2a) – (2f). The bubble size reduces significantly from 3 mm to 1 mm, which is 1.5 times lower than 0 psig (0 kPa). At higher heat fluxes, the bubbles start pinning on the wick surface, and the boiling starts in the form of a series of jets and generates excessive bubbles from the surface to the working fluid. The jets start forming at a low heat flux of 21.723 W/cm^2, which is captured in the boiling pictures. The results demonstrate that there is a series formation of the jet streams of liquid and vapor on the wick surface. At high heat flux, the jets start merging with the liquid and vapor streams which may lead to inter bubble-dynamic. The boiling becomes violent at higher heat fluxes and creates strong thermal stress on the surface and reaches a maximum limit of the nucleate boiling.

5.5 Discussion

During pool-boiling, nucleate boiling plays a vital role in the heat transfer process, and the cavity size behavior at saturation condition is important to study which was discussed in Chapter 2.

From the bubble visualization, it is noticed that pressure affects the bubble departure size. The size of the departing bubble decreases. The change in the bubble departure size can be quantified by the pressure effect using the Fritz correlation [61], expressed in Eq. (5.2),

$$D_d = 0.0208\phi \left[\frac{\sigma}{g(\rho_l - \rho_v)}\right]^{1/2} \quad (5.2)$$

where σ is the surface tension of the water, g is the acceleration of the gravity, ϕ is the wetting angle, ρ_l and ρ_v are the densities of the liquid and vapor, respectively.

For example, the bubble departure diameter decreases from 4.5 mm to 4.00 mm for the pressure ranging from 0 kPa to 620.5 kPa, respectively, using Fritz's correlation. Similarly, the bubble departure diameter for the wick surface at 0 psig, is relatively smaller than the plain copper surface that can be seen in the boiling pictures. The surface roughness and the space between the two sintered particles could be the main reasons for the small bubble departure size. At high-pressure, the bubble departure size reduces further due to the pressure effect which also affects the bubble departure frequency. The smaller bubbles moves faster from the surface and transport heat through excessive bubble generation to the fluid. The higher bubble frequency rate can be related to the change in the thermo-physical properties of water at high-pressure. For example, the surface tension of water is 0.0589 N/m and 0.052 N/m at 0 kPa and 206.8 kPa respectively. At high-pressure, 11.7% of change is noticed in the surface tension of the water. Similarly, a 2.6% change is seen in the difference in the density of water and vapor — the total percentage of change in the property of water results in the reduction of bubble departure size.

The performance of the heat transfer of the wick surface can be explained with the increased active nucleation site densities at higher pressure. The micro convection theory of Foster, 1959 postulates that the HTC linearly depends on the boiling parameters, i.e., bubble departure diameter, bubble departure frequency, and the bubble nucleation site density. The correlation for the HTC is expressed in Eq. (5.3),

$$HTC \; = \; 2\,(2\Pi k_l \rho_l c_{pl}\,)^{1/2} {D_d}^2 f^{1/2} {\eta'}_a \quad (5.3)$$

where k_l is the conductivity of the liquid, c_{pl} is the specific heat of the liquid, ρ_l is the density of the liquid, D_d is the bubble departure diameter, f is detachment frequency, and η_a' is the active nucleation site density.

The HTC is directly proportional to the nucleation site density. The results shown in Fig. 6, show that the high-pressure pool-boiling has a different boiling behavior. The onset point of wall superheat is smaller than at 0 kPa. It indicates that the boiling starts at a low wall superheat, ΔT = T_s - T_{sat}. As already discussed in the previous section; the pressure activates the nucleation sites at the micron size scale. The number of active nucleation sites on the wick surface at 206.8 kPa is significantly higher than at 0 kPa as shown in Fig 8. The enhanced heat transfer performance with the surface modifications, and the pressure is shown in Fig 7. The HTC is enhanced three times compared to the plain surface by the surface modification. We further increase the HTC four times compared to the plain surface by varying the system pressure and with the surface modification. This shows there is a coupled effect of surface modification and system pressure. The possible reasons for the boiling performance enhancement by pressure could be an increased number of active nucleation sites and available surface area for heat transfer due to the wick, which may support to bubble nucleation. Also, the sintered wick increases the effective thermal conductivity of the surface [35]. The increased effective thermal conductivity of the single-layer wick increases the heat flux per unit square of the heating surface. Therefore, the HTC is enhanced!

However, Zuber's model was the first to describe the dry out mechanism responsible for CHF for the infinite plain copper surface [56]. He emphasized the role of the area portion of covered evaporating vapor on the surface and the critical Rayleigh-Taylor wavelength in the CHF mechanisms. According to the Rayleigh-Taylor theory of instabilities, the critical heat flux depends on$(\lambda_{RT})^{-1/2}$, where λ_{RT} is the wavelength, which is a function of the property of water.

The wavelength at the onset of hydrodynamic instabilities can be reduced by varying two variables: changing the thermo-physical properties of the water with varying pressure and employing porous-layer coatings on the surface. The pool-boiling mechanisms on the plain copper surface and the wick surface are shown in Fig 5.9. For the plain copper surface, the CHF occurs at high heat flux densities when the bubbles start merging, and the vapor columns start generating in the form of vapor jets.

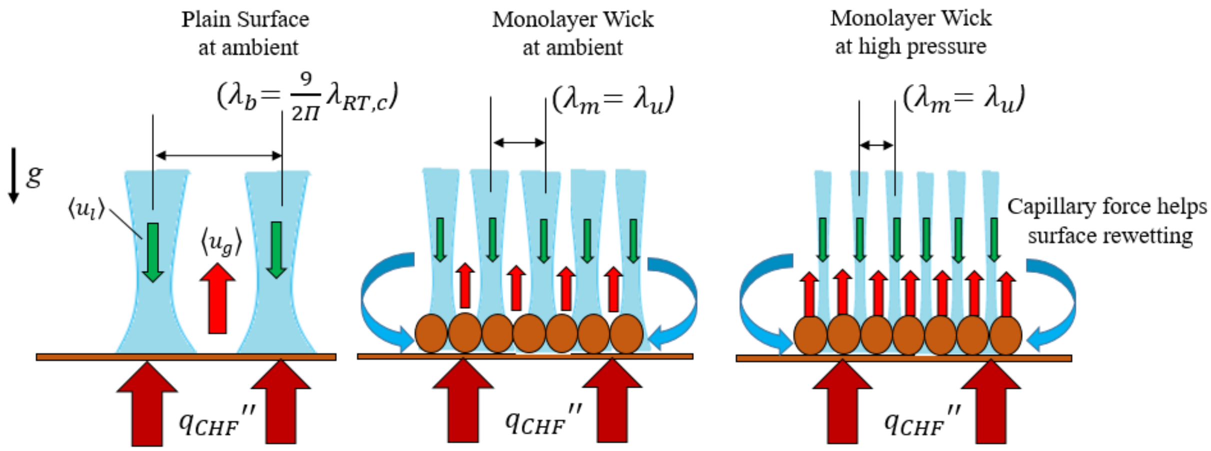

Figure 5.9 Comparison of high-pressure pool-boiling mechanism for the plain copper surface and the monolayer wick surface. The critical heat flux, wick geometries, counter current of liquid and vapor flow paths, hydrodynamic instability wavelength are also shown. The role of capillary force in rewetting the wick surface is illustrated.

Further, the increase of the heat flux density results in increasing the number of continuous jet columns. The process continues until the two neighboring vapor column jets start interacting and reaches the critical velocity of the vapor. When the system enters the critical stage, the system becomes unstable. However, on the wick surface at high heat flux density, a delay is observed in the adjacent column of vapor jets. Due to the porous structure, the bubbles start pinning between the wick and the nucleate boiling begins at a low superheat. The bubble pinning ceases the merging of the jet columns with the adjacent jets and controls the liquid-vapor phase separation.

Interestingly, pressure has more control in the liquid-vapor phase separation by decreasing the modulation wavelength λ_m and is shown in Fig 5.10.

Based on the classical theory of hydrodynamic liquid-choking limit, the modulation in the porous layer coating separates the liquid-vapor by pumping cold fluid through the capillary action from the surface to an evaporation sites [51]. The theory also hypothesized that the counter motion of the fluids causes a viscous-drag resistance in the liquid. Based on the assumptions, the CHF is determined as a function of the fluid properties, coating material properties, and the macro and pore-scale geometries of the coating is expressed in Eq (6). For a uniform thin porous-layer, the critical flux is,

$$\frac{q_{CHF,u}}{\frac{\Pi}{24}{\rho_g}^{1/2}\Delta h_{lv}\left[\sigma g(\rho_l - \rho_g)\right]^{1/4}} = \frac{3\left[\frac{\sigma}{g(\rho_l - \rho_g)}\right]^{1/4}}{{\lambda_u}^{1/2}} \qquad (5.4)$$

and,

$$\lambda_u = \left(\frac{\Pi}{5.88\varepsilon^n}\right)^2 d, \qquad (5.5)$$

where, $\boldsymbol{\varepsilon}$ is the porosity, and *d* is the diameter of the copper particle.

The given correlation depends on the constant empirical parameter *n* is shown in Eq. (7). The critical heat flux is calculated for the uniform thin porous-layer coating using Eq. (6), with $\boldsymbol{\varepsilon}$ = 0.4 and *n* = 1.2, and diameter *d* = 200 μm. The predicted critical heat flux for 0 psig (0.0 kPa), 15 psig (130.4 kPa), and 30 psig (206.8 kPa) is found 178.76, 230.05, and 255.94 kW/m^2, respectively. The predicted CHF is 1.5 times higher than the plain surface. The measured CHF 179.63 KW/m^2 at 0 psig agrees well with the predicted value. However, the values at higher pressure are over predicted with the measured CHF, 182.42 kW/m^2, and 198.16 kW/m^2 for 130.4 kPa, and 206.8 kPa, respectively. The enhanced CHF suggests that the pressure has a significant effect on the modulation wavelength. Calculating the modulation wavelength for pressure ranging from 0 kPa - 206.8 kPa, λ_m varies from 22.5 mm to 21.45 mm. It reduces the distance of the pinned liquid-vapor jet streams by 4.67%. The significant change in the pitch distance is observed in the boiling images. It indicates that there is a liquid-vapor phase separation that happens at the solid/liquid interface which impacts the heat-transfer performance significantly. If we calculate the flow critical length scale for a 200-μm particle diameter and the porosity $\boldsymbol{\varepsilon}$ ranging between 0.4-0.5, then λ_u lies between 8.6 – 2.5 mm. This reduces λ_u by three orders of magnitude. The analysis suggests that the porous structure plays a dominating role in the CHF enhancement by a factor of $\left(\frac{\lambda_m}{\lambda_u}\right)^{1/2}$. Finally, an optimized wick design is needed to maximize the critical heat flux by pore spacing and vapor departure sites using different sizes of sintered particles.

Chapter 6 - High-pressure Pool-boiling Heat Transfer Enhancement Mechanism of Different Particle Size Wicks

6.1 Introduction

In chapter 3, high-pressure pool-boiling performance was studied, and it is found that the pressure influences the boiling performance. The pressure has an impact on the bubble dynamics, resulting in the enhanced nucleate pool-boiling heat transfer. It is found that the surface modification with the wick structure also improves the boiling performance due to the vital role of the capillary driving force in liquid transport through the porous layer. The pressure effect is also studied in the heat transfer performance in chapter 5. However, the performance of pool-boiling heat transfer on porous structure relies on the capillary pressure i.e, capillary driving force, which is attributed to the particle size, packaging parameters, thermal resistance, and the number of wick layers. The boiling performance is explored on different sizes of sintered copper particle wicks at atmospheric pressure. This chapter will also explain how the particle size and the wicking layer influence the performance of pool-boiling heat transfer.

6.2 Sintered Wick Fabrication and Experimental Setup

The design method of wick fabrication is demonstrated in the previous chapter. A similar experimental setup explained in Chapter 2 is used to perform the boiling tests. The experimental procedure with the data uncertainty are elaborated in Chapter 2. The heat flux is calculated using Fourier's law of heat conduction with the measured temperatures using the three thermocouples. The configuration for the heater arrangement is also demonstrated in Chapter 2. Finally, HTC is calculated using the ratio of measured heat flux and the degree of wall superheats. The possible reasons for the heat transfer enhancement are explained in the results and discussion section.

.

6.3 Surface Characteristics

The wick images are taken using a confocal microscope, as shown in Table 6-1. The top views with the measured contact angles are shown in Table 6-1 and Table 6-2. The wicks are fabricated using three different particle sizes varying from 100 μm to 550 μm. The boiling performances are studied to investigate the effect of the particle size. The boiling tests are performed on all the surfaces shown in Table 6.1 and Table 6.2. The fabricated wicks, shown in Table 6-1, show that the particles are distributed uniformly in a closed hexagonal arrangement. Table 6-2 demonstrates the surface characteristics of the layered wick of the different particle sizes. Due to an additional layer on the base wick, a difference can be seen in the layered wicks in comparison to the monolayer wicks. A flat smoothed surface is seen in the monolayer wick images. However, a secondary layer of the particles is noticed underneath the top layer of the layered wicks. The wetting property has been also studied for all the wick surfaces. For the monolayer wick of 100, 200 and 550 μm particle size is 107.2 ± 2°, 108.84 ± 2°, and 97.12 ± 2° respectively. The wicking layer increases the contact angle due to high pore densities in the wick. The static contact angle on a smoothed polished copper surface is to be 80.52° [42]. The surface wettability is increased by 33.13%, 35.17%, and 20.62% for the 100, 200, and 550 μm wick, respectively. The maximum enhancement is found for the 200 μm particle wick compared to the plain surface. The 550 μm wick shows the lowest increment in the surface wettability. The differences in surface wettability can be possible due to the cavity size, particle spacing, and particle arrangement. The bigger particles may create more space between the particles. The large cavity size in the wick may provide a higher surface-volume ratio in the wick.

Table 6-1 The microscopic images of the single-layer wicks with the static contact angle measurements.

Single-layer Wick

100 µm	**200 µm**	**550 µm**

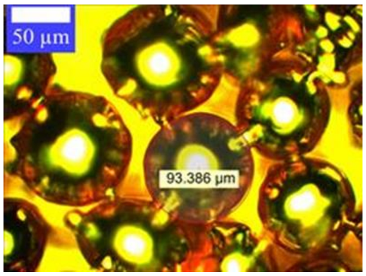

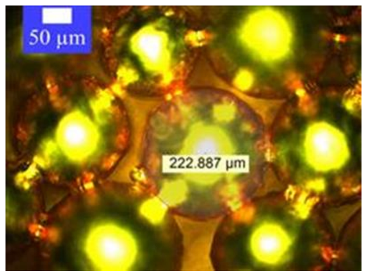

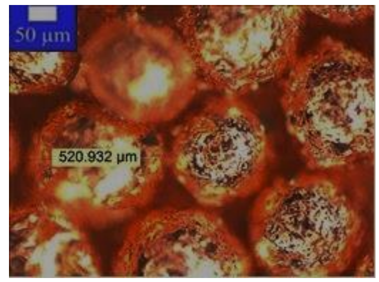

Surface Wettability

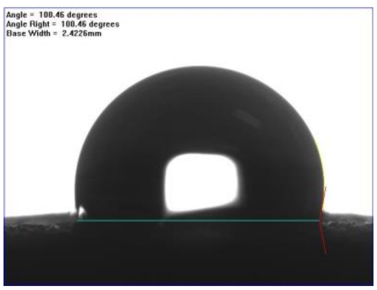

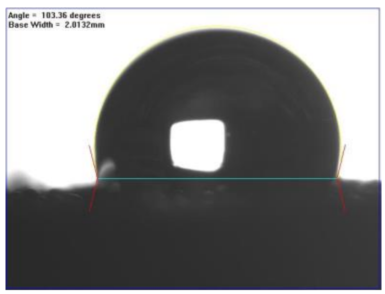

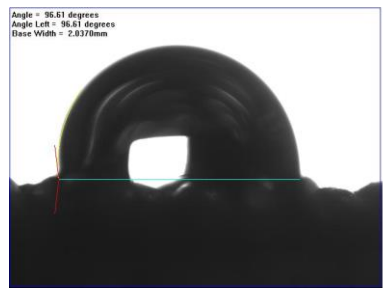

Averaged static contact angle

100 µm	200 µm	550 µm
$107.21 \pm 2°$	$108.84 \pm 2°$	$97.12 \pm 2°$

The surface characteristics for the layered wick were also studied. The maximum layer thickness for the 100, 200, and 550 µm wick is ~300, 600, and 1100 µm, respectively. The three layer 200 µm wick demonstrates the highest surface wettability among all the surfaces. The reason for the enhanced surface wettability may be due to the density of the air pockets in the wick. The contact angle for the 550 µm multilayer wick is improved by 5.16% compared to the monolayer wick. This enhancement can related to the number of layers despite of the thickness of the wick. The 100 µm multilayer wick shows a slight reduction in the wettability. The contact angle is reduced by

6.79% compared to the monolayer wick. The pore size and the compactness in the particle arrangement can be the possible reasons for the contact angle reduction.

Table 6-2 The microscopic images of the multilayer wicks and the static contact angle measurements

Multilayer Wick

100 µm

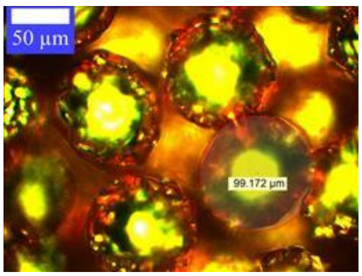

200 µm

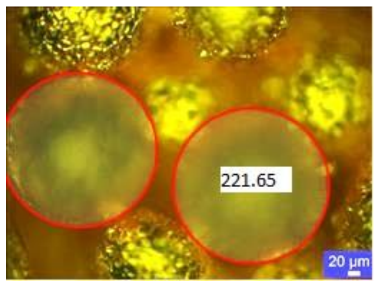

550 µm

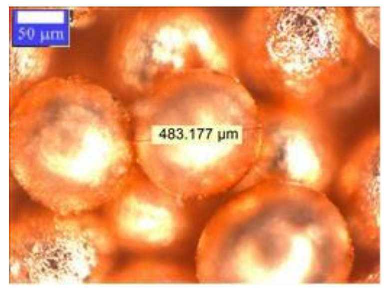

Surface Wettability

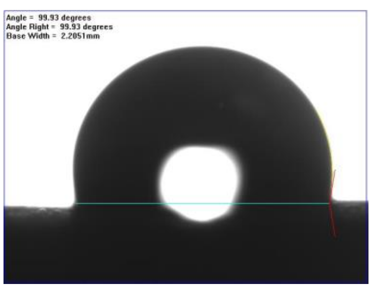

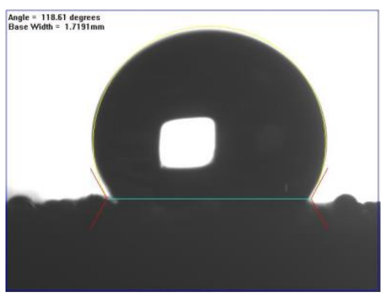

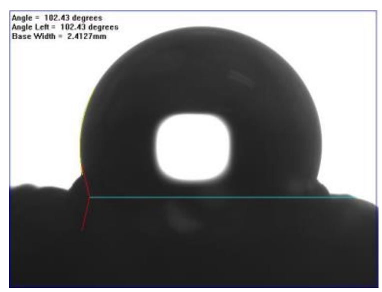

Averaged Static Contact Angle

100 µm	200 µm	550 µm
99.92 ± 2°	118.64 ± 2°	102.42 ± 2°

6.4 Results and Discussion

6.4.1 Effect of Particle size on the Boiling Performance

The parametric effects of particle size on pool-boiling performance are investigated with particle sizes ranging from 100 μm to 550 μm, and the results are compared with the polished copper surface. The particles are uniformly distributed with the same particle sizes and with varied particle sizes ranging 100 μm to 550 μm. For the single-layer wick, the thickness of the wick is similar to the particle diameter. The boiling curves for the single-layer wick of particle sizes ranging from 100 μm to 550 μm are shown in Fig 6.1. The heat flux is measured up to CHF which is displayed in the boiling curve. Each boiling test is performed three times and the heat flux is measured by averaging the measured heat flux. The boiling curve is plotted for the measured heat flux as a function of the wall superheat for all the surfaces. For the plain copper (polished, non-oxidized copper surface), the average measured CHF is 112.14 W/cm^2. The result agrees well with the predicted result of the past studies [39] [64] within ±15 W/cm^2 uncertainty. In comparison to the plain copper surface, the boiling performance is enhanced. The CHF for the 100, 200, 550, and 100/200 μm sintered wick is 184.33, 218.78, 142.68, and 134.54 W/cm^2, respectively. The CHF is enhanced by 64.37%, 95.09%, 27.23%, and 19.19% for the 100, 200, 550, and 100/200 μm sintered wick, respectively. However, for the largest particle size of 550 μm, the CHF is enhanced by 27.23%, which is relatively smaller than other smaller particle size wicks. For the largest particle size, 550 μm, the onset is 2K at 25 W/cm^2 of the heat flux, which is reduced by eight times as compared to the plain copper surface.

In comparison to the other wicks, the wall superheat is significantly smaller that can be due to the enhanced surface area with the large particle size, bubble departure size, and the cavity size. The heat dissipation is relatively higher compared to other wicks, which can be related to the density of active nucleation sites on the surface. A bigger bubble departure size and low departure frequency can cause a bubble coalescence near to the interface, which leads to more vapor formation at the surface compared to the smaller wicks. An excessive vapor formation can further lead to achieving the CHF sooner. The CHF mechanism is explained in detail in the discussion section. The HTC is enhanced at the low heat flux due to a low wall superheat and increased surface area, as shown in Fig 6.2. However, the HTC reduces with varying heat flux. The HTC curve for the 550 μm exhibits similar behavior to a hydrophobic surface.

For the smallest particle size 100 μm single-layer, the boiling curve shows a similar trend as the 200 μm sintered copper wick. At low heat flux less than 75 W/cm^2, the heat dissipation is higher for the 100 μm particle size wick. However, at low heat fluxes, the 200 μm particle wick dissipates less heat than the 100 μm wick due to the active nucleation site densities and the cavity size. The boiling curves of 100 and 200 μm particle intersect at a heat flux of 75W/cm^2. It may occur due to the difference in the capillary pressure supplied by different sizes of the pores with the phase change during boiling. For the 200 μm particle, the capillary pressure could be higher than the capillary provided by the smaller particle size at the intersection point. The difference in the capillary pressure may lead to a controlled liquid-vapor flow over the wick.

For the single-layer wick, the maximum CHF is achieved for the 200 μm particle diameter size wick. The CHF enhancement can relate to the higher number of nucleation sites available at any heat flux over the same area for the smaller particle sizes. The HTC is three times higher than the polished copper surface for a heat flux of 100 W/cm^2.

For the 100 μm single-layer wick, the HTC is enhanced further in comparison to the polished copper surface due to the number of active nucleation sites. At 100 W/cm^2, the HTC is 2.14 times higher than the plain copper surface. A possible reason for the reduced CHF could be related to the dominant effect of the heat transfer area rather than reduced hydraulic resistance with the addition of coating layers [75].

The HTC is further enhanced with the 100/200 µm particle wick over the polished copper surface. The particles are uniformly distributed with particle size ranging from 100 µm and 200 µm. The boiling curve for 100/200 µm shown in Fig 6.1 follows a similar trend as the plain copper surface. The heat transfer coefficient is enhanced with the CHF over the plain copper surface.

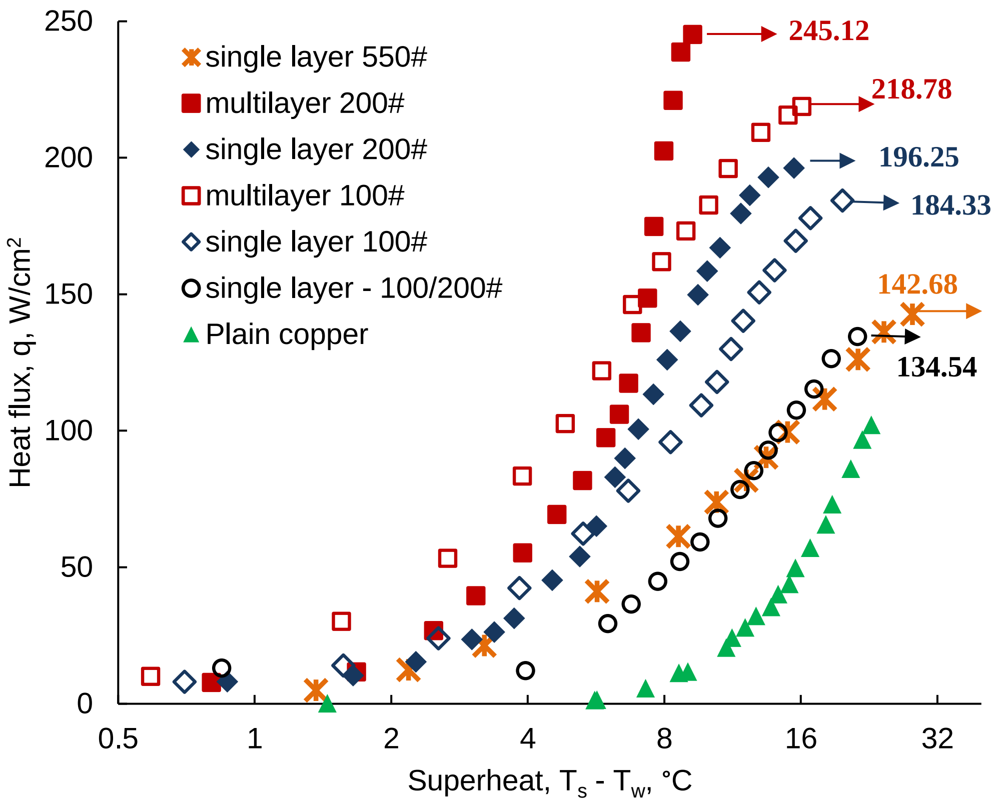

Figure 6.1 The boiling curves of averaged heat flux (q in W/cm^2) and wall superheat (°C) for the sintered copper particle size varying from 100 µm to 550 µm and the polished copper surface The CHF is also indicated for each surfaces with a right headed arrow.

The reason for the HTC enhancement can be related to the cavity size, higher number of active nucleation sites, and/or the capillary pressure supplied by the porous wick as discussed previously. However, the 100/200 µm wick underperforms among the uniformly distributed wick surfaces for the different particle sizes. The CHF and HTC are significantly smaller compared to the 100 µm and 200 μm single-layer wick. The difference in the CHF and HTC maybe due to the difference in the bubble dynamics.

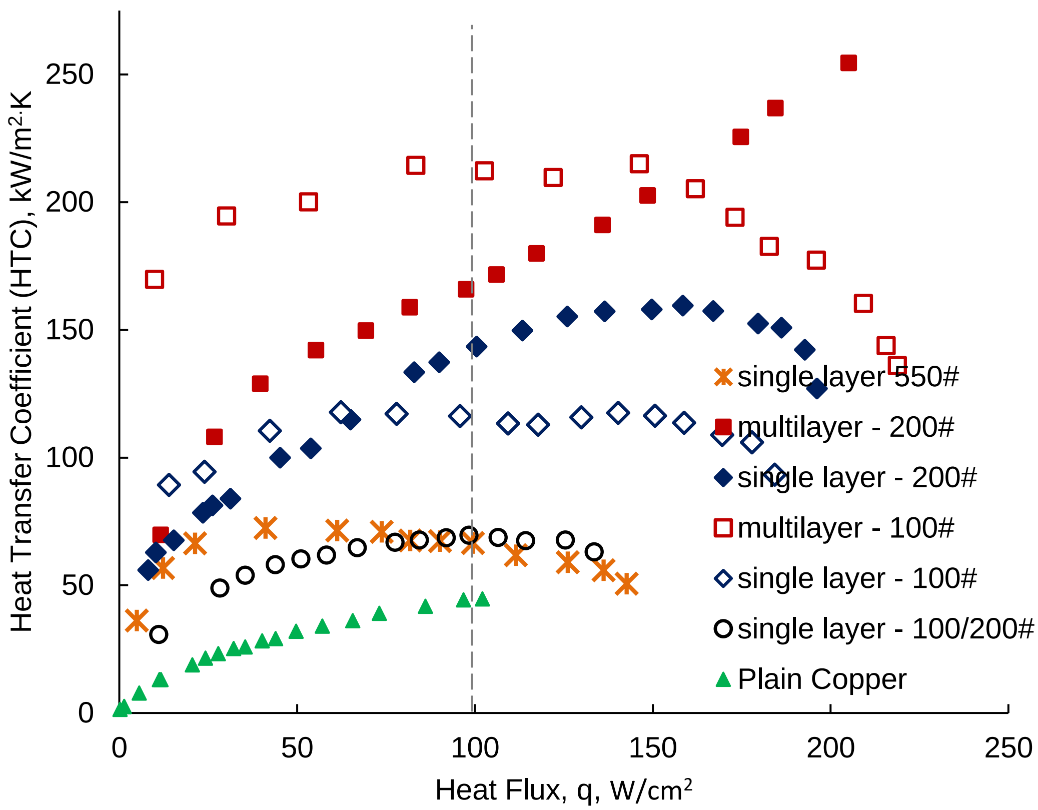

Figure 6.2 The boiling performance curves of heat transfer coefficient (HTC in kW/m^2.K) and heat flux, q in W/cm^2 for the sintered copper particle size varying from 100 μm to 550 μm. A comparison is done with the polished copper surface at a heat flux of 100 W/cm^2.

6.4.2 Effect of sintered wick layer on the boiling performance

The pool-boiling performance is further enhanced with the wick layers. The boiling performance is significantly improved with the number of wick layers, as shown in Fig 6.1. The results are compared with the plain copper and the single-layer wick. For the 200 μm wick, the CHF is found to be 245.12 W/cm^2, which is increased by 118% and 25% for the single-layer 200 μm wick and the polished copper surface respectively. The improvement can be related to the enhanced surface area due to the number of layers, enhanced effective thermal conductivity, improved capillary flow length by the porous layer, and the improved boiling parameters (increased active nucleation sites, reduced bubble departure size sue to the surface roughness, and the bubble pinning at the particle interface). The HTC is significantly improved for all the heat fluxes, as shown in Fig 6.2. At 50 W/cm^2 of heat flux, the wall superheat is reduced by 75% compared to the polished copper surface as shown in Fig 6.1. The superheat reduction can be related to the enhanced thermal conductivity and the increased evaporation surface area compared to the single-layer wick [50][51].

For the 100 μm multilayer wick, the HTC is further enhanced compared to the single-layer wick. The CHF is improved by 18% from the monolayer wick of the same particle size. The HTC is enhanced with the multilayer uniform wick due to the low wall superheat. At low heat flux, high heat dissipation is found as compared to the single-layer wick. However, at high heat flux, the heat transfer performance reduces. This enhancement may occur due to the bubble coalescence and vapor traping in the porous layer from the smaller pore sizes. In comparison to the 200 μm multilayer wick, the HTC is higher at the low heat flux because of high heat dissipation and the low superheat. The boiling curves intersect at a point of heat flux of 150W/cm^2. In comparison to the single-layer wick, the boiling curves intersect at a heat flux of 75W/cm^2, which is half of the heat flux. This can be related to the wicking rate supplied by the capillary-driven pressure by the wicks and the liquid flow resistance within the wicking layer.

6.4.3. Discussion

Similar studies in the literature have shown the same effect of particle size on boiling heat transfer enhancement with sintered coatings. Sarangi et al. [75] performed the boiling tests on sintered particles ranging from 45-53 μm to 850-1000 μm in size. The optimized particle was found to be ~100 μm for the boiling enhancement with a 95% reduction in the wall superheat and the maximum

CHF 121 kW/m^2 for FC-72. The least performance was reported for the bigger particles (850 – 1000 μm) due the increased number of nucleation sites formed by the porous surface with a higher rate of bubble coalescence at the wall interface and vapor clogging which hinders the bubble departure. Chang and You [77] performed boiling tests for the micro-porous enhanced surfaces using five different sizes of diamond particles for FC-72. The maximum heat transfer coefficient was reported for particle sizes ranging from 2 to 20 μm. Further increase in the particle sizes led to a reduction in the HTC. The effect of particle size on the boiling performance corresponded to the liquid layer thickness that was predicted to become superheated between successive bubble departures. The studies also emphasized that layer addition increase the hydraulic resistance without any effect benefit.

In the present study, a similar trade off in the CHF enhancement and the HTC improvement is found. The 200 μm particles achieved the maximum CHF among the particle sizes of 100 μm and 550 μm. The nucleate boiling behavior can be explained with the bubble dynamics at low heat fluxes. The bubble dynamics can be explained using the boiling images taken by a high speed camera at 2000 fps for (a) plain copper surface (b) 200 μm single-layer wick, and (c) 550 μm wick at onset and a higher heat flux shown in Fig 6.3. The bubble departure size significantly reduces with a surface modification by porous wick. At onset, the bubble departure size is 4 mm while the departure size significantly reduces to a smaller size for the 200 μm. This can be related to the pores size. However, the bubble departure increases for 550 μm which is expected because of a large pore size. At high heat fluxes, the boiling behavior differs from the plain copper surface. Excessive vapor formation is found due to the rapid bubble coalescence.

At Onset **High Heat Flux**

A. Plain Copper Surface

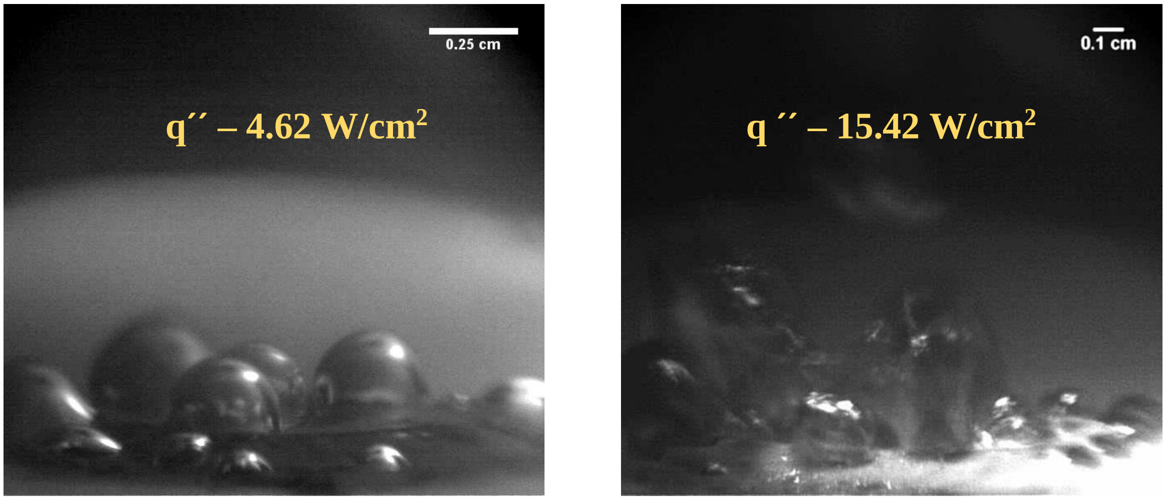

B. 200 µm wick – Single-layer

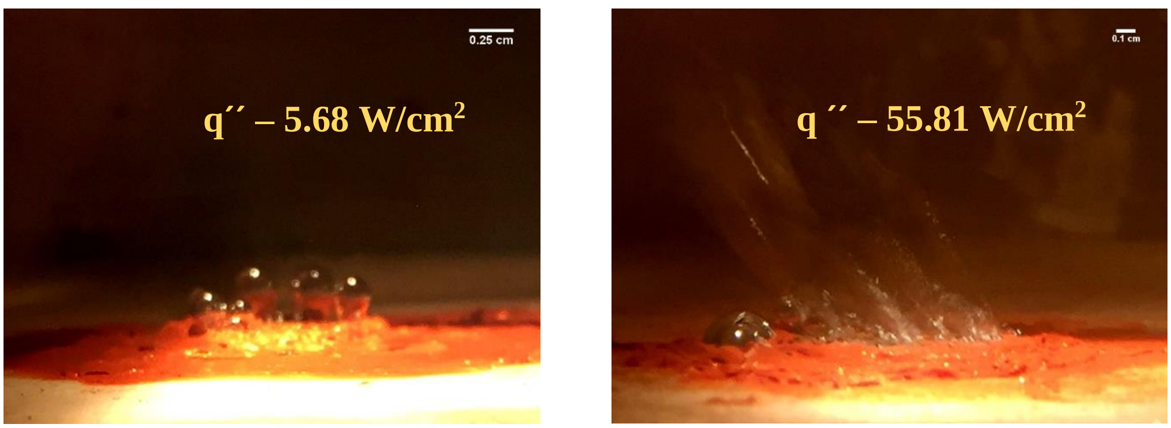

C. 550 µm Wick – Single-layer

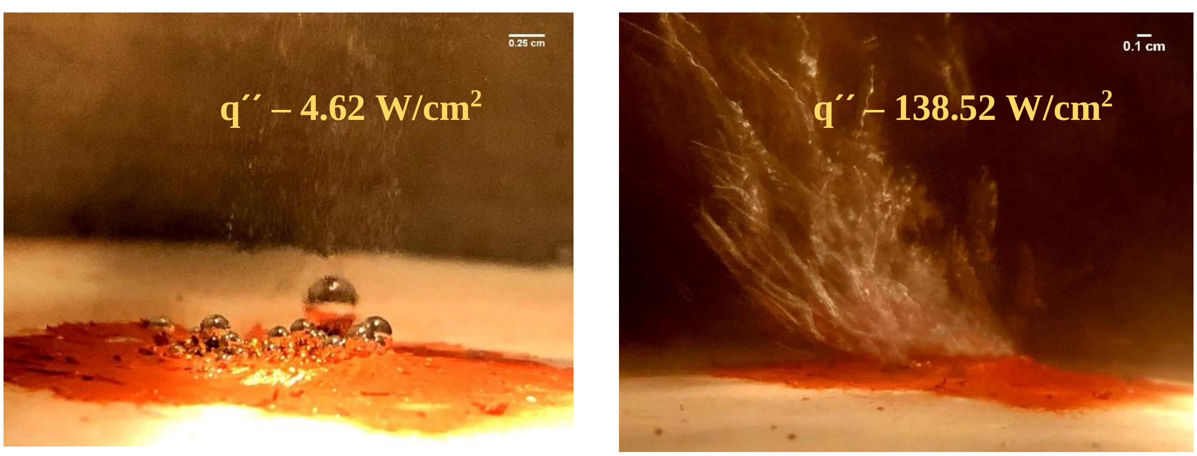

Figure 6.3 Compared boiling images for (a) polished copper surface (b) 250 µm and (c) 550 µm at two different heat fluxes.

The boiling on the wick surfaces occurs through vapor jet columns at high heat fluxes as shown in the boiling images Fig 6.3. This indicates that the wick may offer a controlled liquid-vapor flow driven by capillary pressure which may cause a delay in surface dry out.

The bubble departure size further increases for the 550 μm particles due to the large cavity size which is shown in Fig 6.3. A larger cavity size nucleates the bubble at a low onset for low heat fluxes that cause to a high HTC. As the heat flux increases, the bubble size may saturate and cause inter-bubble dynamics which can cause jet formation at the interface. A similar trend is found on a Teflon coated surface.

The CHF enhancement is difficult to explain with the bubble dynamics due to rapid vapor formation at high heat fluxes. Considering Zuber's model, the CHF was explained with the distance spacing between the vapor masses known as the Rayliegh-Taylor wavelength in Chapter 5. In order to understand the CHF enhancement with the microstructure, it is very important to understand the capillary limit supplied by the porous wick with different particle sizes. In pool-boiling, the nucleate boiling reaches a limit when the maximum heat flux is achieved and the working fluid evaporates very quickly leading to system towards the maximum limit. In wick structure, the capillary pressure plays a significant role in the liquid flow through the wick. If the capillary pressure in the wick goes to a beyond the maximum limit called the critical pressure, choking may occur before reaching the maximum heat flux. Based on this mechanism, the capillary pressure P_c, can be defined by Young-Laplace equation is expressed in Eq. (7.1)

$$P_c = \frac{2\sigma}{r_c} \qquad (7.1)$$

Where, $\boldsymbol{\Delta}$P is the pressure difference between the liquid fluids, σ is the surface tension, r_c is the critical radius of the cavity size.

Eq 7.1 indicates that the amount of capillary pressure in the wick directly relates to the pores/cavity size. The excess pressure due to capillary-driven force may result in the tendency of liquid to either penetrate into the porous matrix or remain separate from it.

The liquid velocity is determined using the continuity equation,

$$\dot{m} = \rho A_c v \qquad (7.2)$$

Where, $\dot{m}$ is the mass flow rate, ρ is the density of the liquid, A_c is capillary surface area, and v is the velocity of the liquid.

From Darcy's law, the pressure drop is defined as,

$$\frac{\Delta P}{L_m} = \frac{\mu v}{\kappa} \qquad (7.3)$$

Where, ΔP is the pressure difference between the liquid fluids, μ is the dynamic viscosity of the liquid, v is the liquid velocity, and κ is the permeability.

The permeability is expressed mathematically,

$$\kappa = \frac{\varepsilon^3 {d_p}^2}{180\,(1-\varepsilon)^2} \qquad (7.4)$$

Where, κ is the permeability, d_p is the particle diameter, ε is the porosity.

The heat transfer rate, Q is related to the mass flow rate and latent heat is expressed by,

$$Q = \dot{m}\, \Delta h_{lg} \qquad (7.5)$$

Where, $\dot{m}$ is the mass flow rate, and Δh_{lg} is the enthalpy of the liquid-vapor.

Equating Eq 7.1, 7.2, 7.3 and 7.4, for monolayer the governing equation changes to,

$$q_{CHF} = \frac{2\sigma}{r_c} X \frac{\kappa}{\mu} X \frac{\rho A_c}{L_m} \Delta h_{lv} \qquad (7.6)$$

The CHF can be predicted from equation 7.6 which depends on the geometrical parameters. The CHF depends on the capillary pressure, geometry parameter, the liquid meniscus and the fluid properties. From Eq 7.6, it is noticed that the CHF directly dependent on the capillary area that can impact the wicking volumetric flow rate through the porous wick. Hu et al. [79] provided an extended wicking-based CHF model for the micro-pillar arrays which depends on the volumetric wicking rate. Similarly, the present model suggests that for CHF modeling it is important to optimize the cavity size for maximizing the capillary pressure. In order to calculate the optimum cavity size, the particle packaging also plays a crucial role which can be seen in Fig 6.4. The side and top views showing different types of particle arrangement are shown in Fig 6.4.

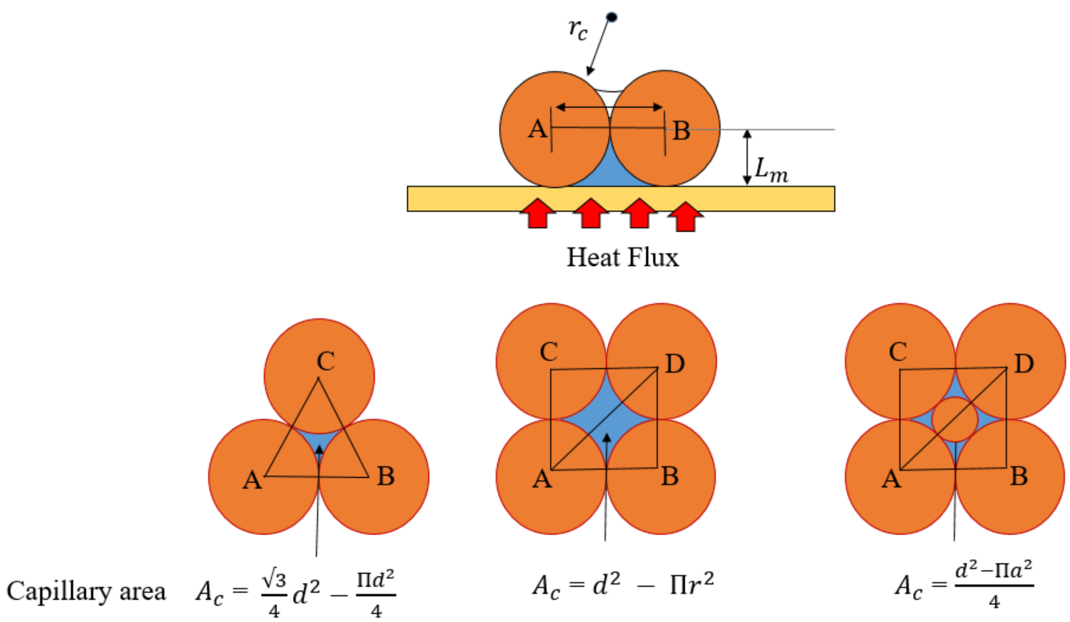

Figure 6.4 The side and top views of the cavity for various particle packaging arrangements. r_c, L_m, A_c represent the critical radius, meniscus length and the capillary area respectively.

Thus shows that the capillary pressure is inversely proportional to the critical radius. It suggests that the capillary pressure increases significantly with reduced particle size. For example at ambient condition, the capillary pressure varies from 1178, 589, 214 kPa for the 100, 200, and 550 µm particle size. The capillary pressure decreases with the particle size. However, in boiling a two-phase-change occurs at the interface though the vapor bubbles. Smaller particles may activate nucleation sites at low heat fluxes due to the smaller cavity size. But, that can also lead to vapor trapping in between the cavities and choking of the capillary flow path, resulting in less vapor bubbles escape from the heated surface. In addition, a bigger cavity size is also not favorable for the boiling performance enhancement due to the low capillary pressure and the larger bubble departure size.

6.5 Effect of Sintered Copper Particle Size and the Wick Layer on the Boiling Performance at High-pressures

The results for the high-pressure pool-boiling are described in the following sections. The boiling tests are performed to explore the phase-change heat transfer on the wick surfaces of different particles size. The effect of the layer on the boiling performance at high-pressures is discussed. The results are compared with the boiling results of the polished copper surface. The boiling mechanism and the possible reasons for the boiling enhancement with the wick layers are described in the discussion section.

6.5.1 100 μm single and multilayer

Pool-boiling curves for the copper surface and a single-layer 100 μm particle wick are compared in Fig 6.5. The tests are performed for DI water at three different pressures. The open symbols refer to the plain copper surface, while the dotted symbols refer to results for the wick surface. Measured critical heat fluxes for all the surfaces are marked with the right headed arrows. The pressure effect on the boiling performance enhancement on the polished copper surface is shown in Fig 7 [64]. The wick also affects the boiling performance, which was explained in the previous section. The boiling performance is further enhanced at high-pressures. The sintered wick exhibits better boiling performance with lower wall superheat for low heat fluxes as shown in Fig 6.5. A lower wall superheat can be related to the enhanced surface area with the wick particles, the cavity size, and the supplied capillary pressure by the wick. The measured critical heat flux is observed to be 184.34, 199.64, and 208.36 W/cm^2 at 0 psig (0 kPa), 15 psig (103.4 kPa), and 30 psig (206.8 kPa).

In comparison to the plain copper surface, the CHF is enhanced by 64.38%, 68.8%, and 59.89% for 0 psig (0 kPa), 15 psig (103.4 kPa), and 30 psig (206.8 kPa) respectively. Fig 6.6 demonstrates the heat transfer performance for the 100 μm sintered wick. For example, at 100W/cm^2, the HTC is 2.5X times than the polished copper surface at 0 psig (0 kPa). The sintered wick offers 2X times enhancement with the pressure.

The boiling performance is enhanced further with the multilayer wick, as shown in Fig. 6.7, and 6.8. The observed CHF is 218.78, 221. 34, and 225.14 W/cm^2 at 0, 15, and 30 psig, respectively. In comparison to the single-layer wick, the CHF is enhanced by 18.68%, 9.98%, and 7.45% at 0 psig (0 kPa), 15 psig (103.4 kPa), and 30 psig (206.8 kPa) respectively. On the other hand, the CHF is improved by 95.09%, 87.21%, and 72.89% at 0 psig (0 kPa), 15 psig (103.4 kPa), and 30 psig (206.8 kPa) respectively compared to the polished copper surface. The multilayer outperforms the boiling performance over a single-layer wick. The difference in the CHF enhancement can relate to hydrodynamic behavior. It is interesting to note that the multilayer wicks perform best in comparison to the single-layer wick, as shown in Fig. 6.8. The HTC is 5X times and 4X times for the multiplayer wick than the polished copper surface at 0 psig (0 kPa) and 30 psig (206.8 kPa), respectively.

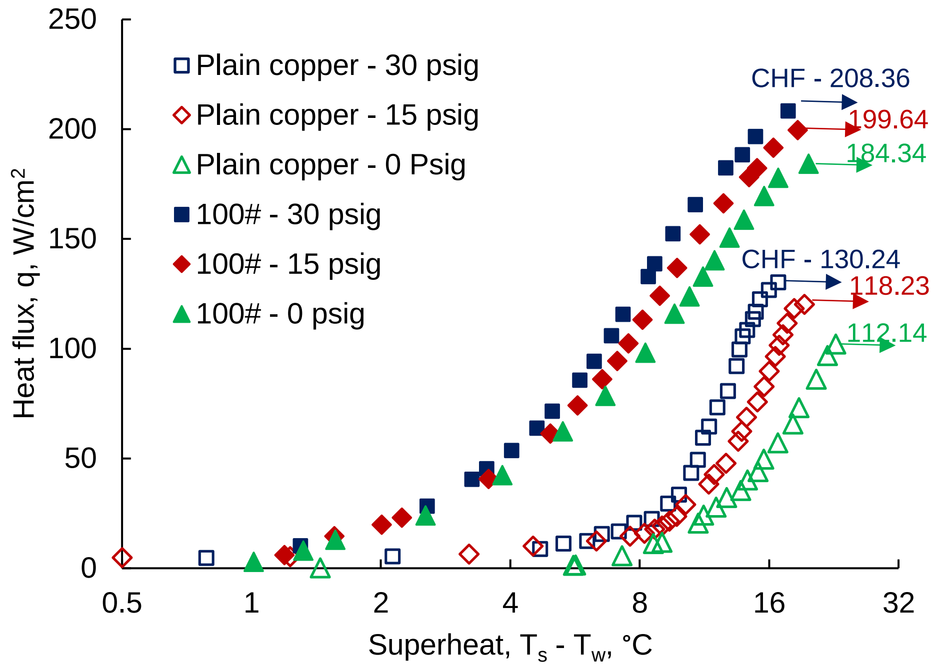

Figure 6.5 The boiling curve for 100 micron single-layer wick at different high-pressures

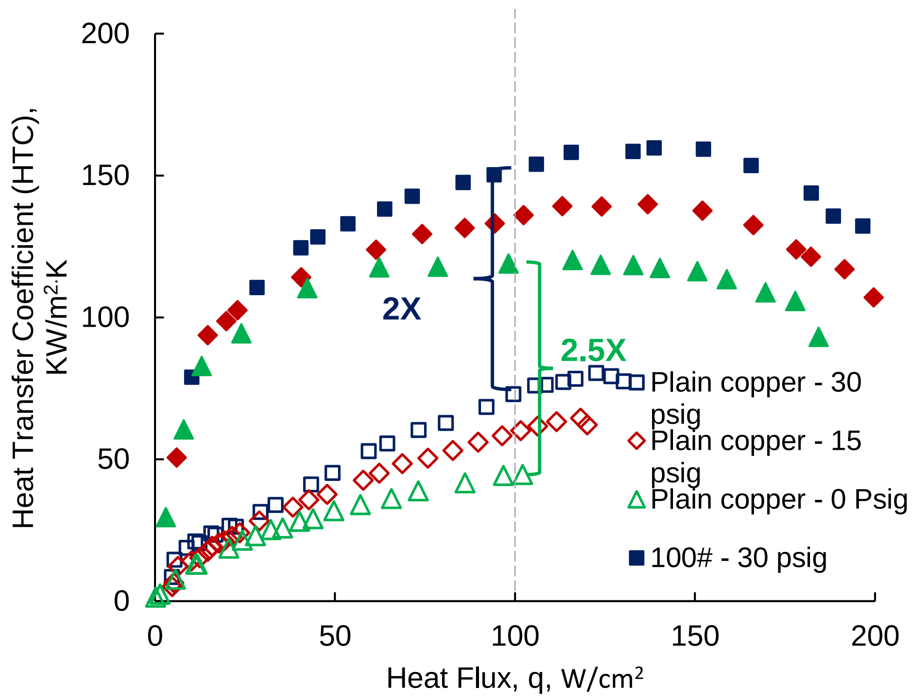

Figure 6.6 The heat transfer performance curve for 100 micron single-layer wick at different high-pressures

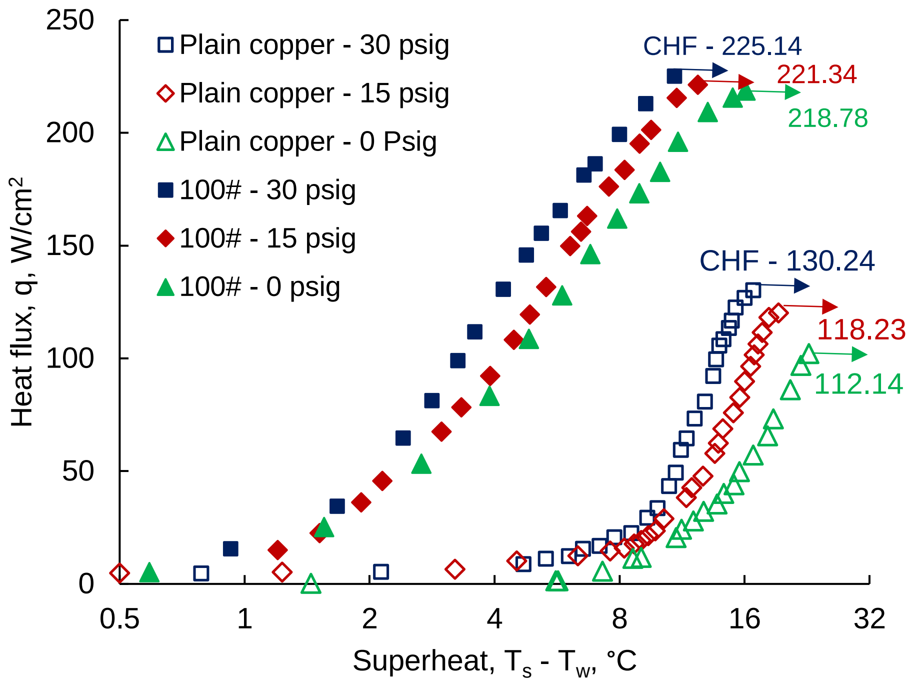

Figure 6.7 The boiling curve for 100 micron multilayer wick at different high-pressures

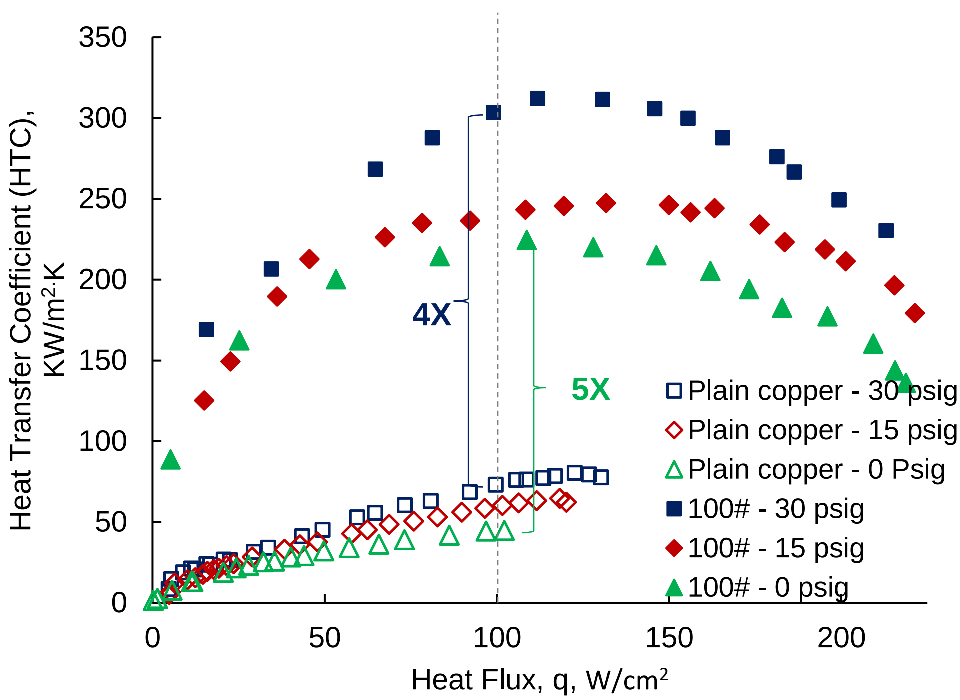

Figure 6.8 The heat transfer performance curve for 100 micron multilayer wick at different high-pressures

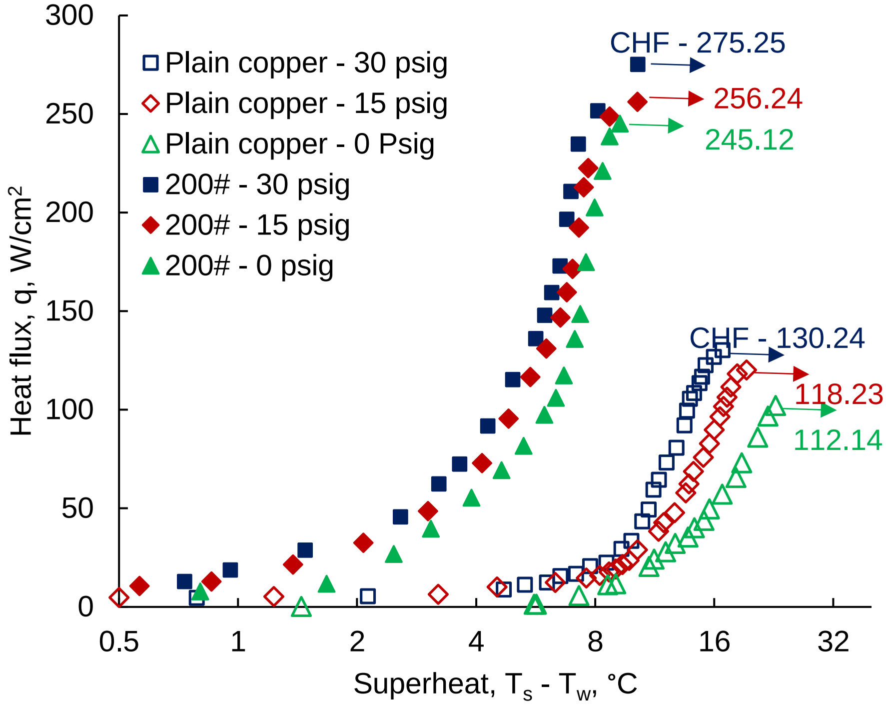

Figure 6.9 The boiling curve for 200 micron three layer wick at different high-pressures

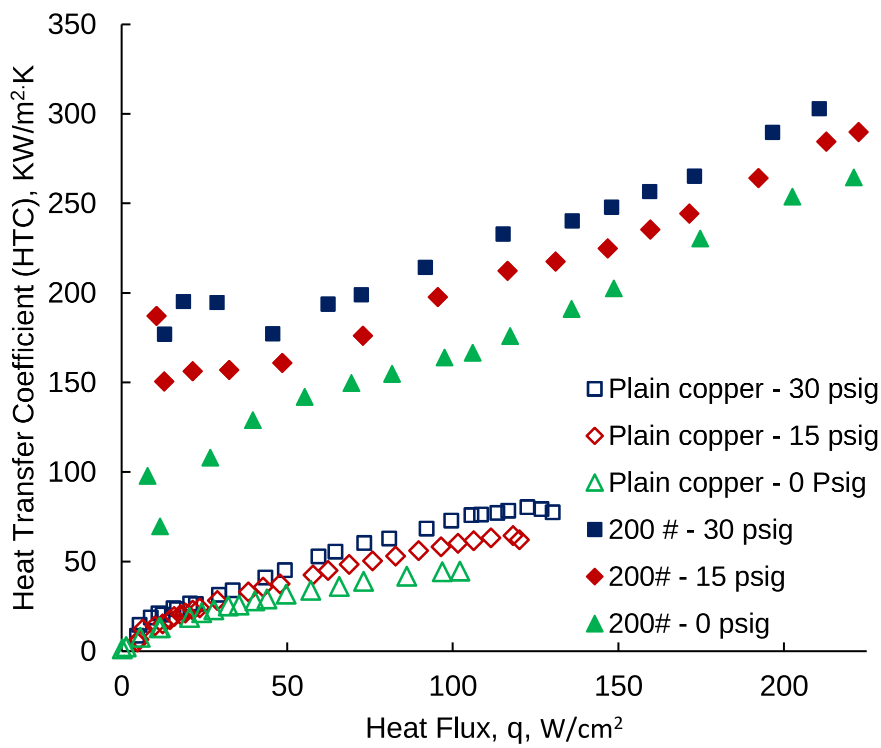

Figure 6.10 The heat transfer performance curve for 100 micron single-layer wick at different high-pressures

The boiling test was also performed for the 200 μm size multilayer wick, as shown in Fig 6.9 and 6.10. The boiling curves are for the 100 and 200 μm multilayers at high-pressures are different. The 200 μm multilayer offers enhancement with all the heat fluxes, while the 100 μm sintered particle the boiling performance maximizes at a specific heat flux, and then the performance starts deteriorating. The difference in the mechanism can be related to the wick layer thickness and how the capillary flow path improves within the layers.

6.5.2 Discussion

The multilayer wick offers a combination of high heat dissipation from a large heated area along with a low wall superheat. Many studies have reported that multilayer wick provides several benefits in the capillary-fed boiling [50][51][74] [75] [76] [77] [78]. It is reported in the past studies, a thick wick (of thickness-to-particle diameter ratio ranging from 4 to 5) with multilayers of sintered particles can dissipate high powers however exhibits large thermal resistances due to vapor clogging in the wick pore spaces during boiling [75]. The present analysis suggests that the pressure has the potential to provide separate flow pathways of liquid-vapor flow from the wicks. As the boiling curves for multilayer wick of different particle sizes shows, boiling performance improves significantly at high-pressures. The mechanism of high-pressure capillary fed boiling is shown in Fig 6.11. The red and green arteries represent the liquid and vapor flow from the wick. Indeed, pressure affects the boiling performance due to changes in the thermophysical properties of water and bubble dynamics. The pressure activates the nucleation sites at a low superheat [64]. It also impacts the bubble departure diameter and the nucleation site densities. A similar effect is observed in the bubble dynamics of high-pressure capillary fed boiling for the multilayer wick. Due to surface modification, the multilayer wicks provide more cavities in the wick. However many studies have reported a low heat dissipation due to thermal resistance for multilayer wicks due to vapor clogging. Smaller particles wick provides less permeability that hinders the vapor escape for the wick. In the present studies, we have made the following observations in the boiling behavior as compared to the ambient pressure:

1. Increased nucleation sites
2. Smaller departure diameter with a high-frequency rate
3. Boiling through jet columns

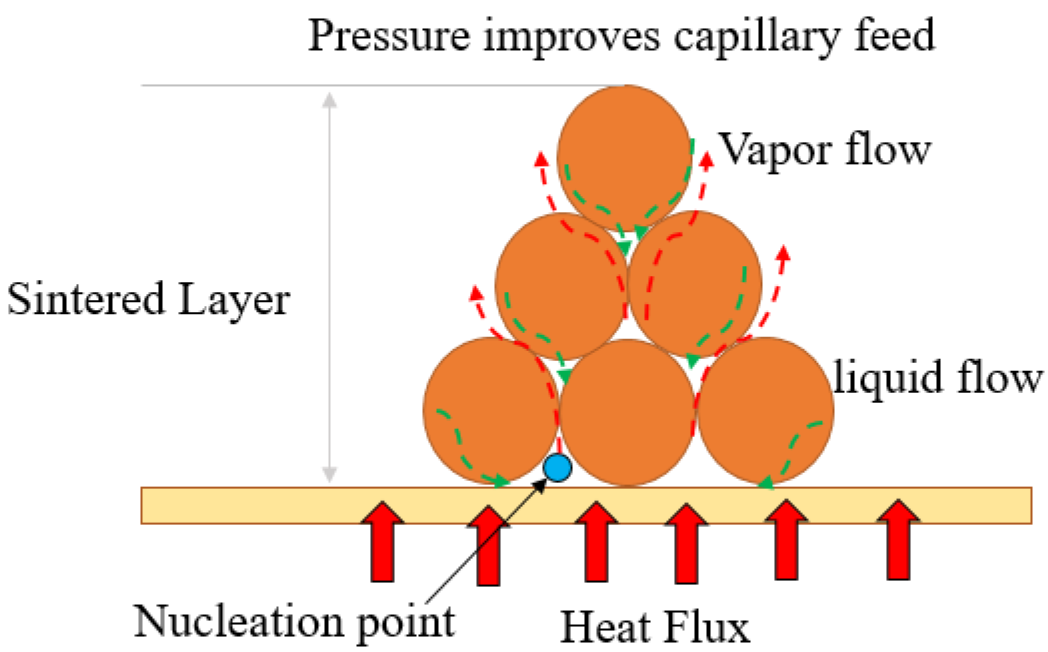

Figure 6.11 The mechanism of high-pressure capillary fed nucleate boiling.

The increased number of active nucleation sites in the multilayer wick can be related to the pressure and the surface features provided by the multilayer wicks. Also, the pressure may open the cavity mouths at a low superheat that can help in activating more nucleation sites. It is also possible that pressure may impact the vapor flow path underneath the wick particles to prevent vapor choking underneath the wicks improving the capillary flow length of liquid-vapor between the particles, regardless of the cavity size. Therefore, the multilayer wick amplifies the pool-boiling performance by offering a liquid-vapor flow separation from the particles that delays the surface dry out.

Chapter 7 - Conclusions and Future Work

7.1 Summary

The performance of high-pressure pool-boiling heat transfer and its mechanisms are discussed and critically analyzed for the different engineered surfaces:

In chapter 2, the pool-boiling setup is demonstrated with the test procedure. The experimental work is designed based on the previous work [65]. The design fabrication of the plain copper substrates is also discussed in detail. The methods for the uncertainty and error measurements are also presented. In the high-pressure pool-boiling experimental set up the back pressure regulator valve plays an important role in maintaining pressure inside the boiling chamber. The working principle of the back pressure regulator valve is also explained in the chapter. This chapter will help in building a high-pressure pool-boiling experimental setup and running boiling tests for future experimental work.

Chapter 3 provides a systematic study of high-pressure pool-boiling on a plain copper surface for water. The hydrodynamic behavior of primary bubbles at high-pressure is studied and analyzed using visualization technique. The impact of pressure on the bubble departure size, detachment frequencies, and nucleation site densities is studied. High-pressure boiling has also shown a different bubble dynamic behavior. The performance of high-pressure pool-boiling heat transfer is discussed. The boiling data and heat transfer coefficient values are compared and validated with different predicted theories. The heat transfer coefficient value is measured and analyzed at different heat fluxes. A significant change is noticed at the high heat fluxes compared to the low heat fluxes. The maximum heat transfer enhancement is found to be 175% at 60 psig (413.7 kPa). The results suggest that pressure enhances heat transfer. The CHF is also calculated and compared with the predicted theories. The trend for the CHF at high-pressures is found similar to the

Kandlikar's predicted theory. The CHF enhancement with the pressures is explained with the macro layer theory.

The combined effects of pressure and wettability on the performance of pool-boiling heat transfer is studied in chapter 4. The size of active nucleation sites, bubble departure diameter, bubble release frequency and the nucleation site density are studied with the existing models for different pressures. As we increase the pressure, the size of the nucleating bubble decreases and the bubble release frequency increases due to change in the thermophysical properties of water. A similar behavior is found for the plain surface. The effect of wettability is also investigated. The change in the wettability gives a benefit in the bubble incipient wall superheat. The wall superheat decreases by 35% and 45% at 30 and 45 psig, respectively. At 50W/cm^2 of heat flux, the heat transfer improves by 100% at 45 psig. At low heat flux, the Teflon© coated surface exhibits the maximum enhancement. However, at a high heat fluxes, 100W/cm^2, the HTC is reduced by 50%. The result in the HTC enhancement at low heat flux for the Teflon© can be related to the bubble departure size and active nucleation sites densities.

In chapter 5, the high-pressure pool-boiling performance is studied for the monolayer sintered copper powder wick surface using water as a working fluid. The wick structure was fabricated using a multi-step sintering process with 200 μm copper particles. The wick improves the surface wettability due to the cavities present in the wicks. The heat transfer performance is compared to the plain copper surface. The results found that the critical heat flux for the monolayer wick surface is 1.75 times higher than that of the plain surface at 0 psig (0 kPa). However, the critical heat flux is only 1.1 times higher than that of 30 psig (206.8 kPa) for the wick surface. The heat transfer performance enhancement is related to the possible decrease in the hydrodynamic instability and the capillary effect in rewetting the surface. It is found that pressure has a significant impact on the modulation wavelength. It reduces by 4.67% for the pressures ranging from 0 psig (0 kPa) – 30 psig (206.8 kPa) and controls the liquid-vapor phase separation at the solid-liquid interface with a bubble pinning effect. The wick surface also decreases the wall superheat by three orders of magnitude at 50W/cm^2. The maximum heat transfer coefficient, 252.46 W/cm^2 K is found at 100 W/cm^2 of heat flux for 30 psig (206.8 kPa). The high-pressure boiling result shows that the heat transfer coefficient is enhanced by 100% as compared to 0 kPa. The surface modification increases the HTC by three orders of magnitude with respect to the plain copper surface. However, the pressure further amplifies the performance by four times compared to the plain copper surface. The HTC enhancement is related to the increased number of nucleation sites, enhanced effective thermal conductivity, and increased evaporation surface area. Overall, the surface modification and the pressure amplify the heat transfer performance and dissipate a large amount of heat passively at a low thermal resistance, thus enhancing CHF and the HTC.

The effect of different sizes of sintered particle wicks on the boiling performance at high-pressures is studied. The design fabrication of the sintered wick layer is also discussed in Chapter 6. The pool-boiling results of monolayer wick of different particle sizes are compared with the polished copper surface. The results demonstrate that the 250 μm sintered particles perform best among the particle sizes studied. Particle sizes less than 250 μm enhance the nucleate boiling heat transfer at the low heat fluxes with a low wall superheat due to small cavity sizes and increased active nucleation sites. However, the CHF for the smaller particle size decreases because of the low thermal resistance due to vapor clogging: Particle size greater than 250 μm performs the worst. The HTC curve for the bigger particle exhibits a similar behavior of a hydrophobic surface. It provides high thermal efficiency at the low heat fluxes due to large cavity sizes (larger bubble departure diameter) and a low wall superheat. The boiling performance decreases further as the heat flux increases. This chapter also demonstrates a model to validate the experimental results. The high-pressure boiling results are also discussed for the monolayer and multilayer wicks. The possible reason for the enhancement due to the pressure effect is presented. The mechanism of high-pressure capillary fed boiling is also discussed in this chapter. It is suggested that the pressure opens the cavity mouths and improves the vapor flow path underneath the wick particles, which prevents the vapor choking underneath the wicks that may enhance the capillary flow length of liquid-vapor between the particles regardless of cavity size/permeability.

7.2 Suggested Future Work

In the introduction section, it is highlighted that the two-phase cooling has been receiving considerable interest in advanced thermal management. Indeed, two-phase heat transfer is difficult to understand due to complicated heat transfer mechanisms of conduction, convection, radiation, and evaporation. The present work will bring attention to pool-boiling heat transfer enhancement at high-pressures. The following action will provide a future direction to the technology advancement of two-phase cooling technology:

1. Development of an analytical model for the CHF of high-pressure pool-boiling heat transfer

In chapter 3, the experimental results are compared with the existing models. None of the models capture the CHF and HTC enhancement mechanism with high-pressure. Moreover, the present study demonstrates different hydrodynamic behavior. More experimental data is required to understand the bubble dynamics at high-pressures during boiling heat transfer. A new mechanistic modeling is needed to explain the CHF enhancement mechanism.

2. Numerical modeling of high-pressure pool-boiling behavior

It is well understood that performing a numerical simulation for boiling is a challenging task for the two-phase heat transfer. More numerical modeling is needed for solving mass, momentum, and energy equations to understand the boiling behavior with surface modifications.

3. High-pressure Pool-boiling on varying wettability

In the present study, high-pressure pool-boiling heat transfer enhancement is performed for a Teflon coated hydrophobic surface. In the past, low surface energy like Teflon coating surface has been ignored for the boiling applications. Teflon coated surfaces can be utilized in small power dissipation electronic cooling applications. The effect of coating thickness layer on the boiling performance can be explored in the future.

4. Flow visualization and Thermography study of nucleating bubbles

In nucleate boiling heat transfer bubble dynamics play an essential role in the heat transfer enhancement. At high-pressure, the bubble departs faster from the heated surface than at atmospheric pressure. High-speed flow visualization and thermography would help us to capture the vapor bubbles and understand the thermal stratification at the nucleation points. This study will provide a better understanding of bubble dynamics with surface modifications.

5. Analytical modeling for capturing the CHF mechanism for sintered wicks

Several experimental studies have been performed to model the CHF mechanism for the capillary fed boiling for different sizes of sintered particles. In the present study, it is also seen that high-pressure pool-boiling exhibits different boiling behavior. A qualitative explanation has been provided to explain heat transfer enhancement. However, it is desirable to model the bubble dynamics to better understand the effect of the coating layer on the bubble incipience characteristics. The present study also provides mechanistic modeling based on the particle size and induced capillary pressure supplied by the wicks. The CHF depends on various parameters like critical radius, capillary flow length, and the capillary area. It is desirable to define all these parameters accurately to explain the high-pressure capillary fed boiling mechanism.

References

1. https://www.eia.gov/todayinenergy/detail.php?id=39092
2. Garimella, S. V.; Persoons, T.; Weibel, J. A.; and Gektin, V., "Electronics Thermal Management in Information and Communications Technologies: Challenges and Future Directions" (2017). CTRC Research Publications. Paper 321. http://dx.doi.org/10.1109/TCPMT.2016.2603600
3. F. Chandler, "NASA Technolgy Roadmaps," NASA, 2015 2015.
4. B. M. T. Swanson, F. Chandler, W. Bruce, C. Dinsmore, C. Kostyk, "NASA Technology Roadmaps, TA14: Thermal Management Systems," NASA, 2015.
5. K. H. M. Kliss, F. Chandler, R. M. Bagdlgian, J. Fishman, A. Jeevarajan, et al., "ASA Technology Roadmaps, TA6: Human Health, Life Support, and Habitation Systems," 2015
6. Tuckerman, D. B., & Pease, R. F. W. (1981). High-performance heat sinking for VLSI. *IEEE Electron device letters*, *2*(5), 126-129.
7. Bowers, M. B., & Mudawar, I. (1994). Two-phase electronic cooling using mini-channel and micro-channel heat sinks: Part 2—Flow rate and pressure drop constraints.
8. Marcinichen, J. B., Olivier, J. A., & Thome, J. R. (2012). On-chip two-phase cooling of datacenters: Cooling system and energy recovery evaluation. *Applied Thermal Engineering*, *41*, 36-51.
9. Karimi, G., & Li, X. (2013). Thermal management of lithium-ion batteries for electric vehicles. *International Journal of Energy Research*, *37*(1), 13-24.
10. Lim, D. H., & Kim, S. C. (2014). Thermal performance of oil spray cooling system for in-wheel motor in electric vehicles. *Applied Thermal Engineering*, *63*(2), 577-587.

11. Price, D. C., Weber, R. M., Schwartz, G. J., McDaniel, J., & Jose'L, L. (1999). *U.S. Patent No. 5,960,861*. Washington, DC: U.S. Patent and Trademark Office.
12. Campbell, L. A., Chu, R. C., David, M. P., Ellsworth Jr, M. J., Iyengar, M. K., & Simons, R. E. (2013). *U.S. Patent No. 8,619,425*. Washington, DC: U.S. Patent and Trademark Office.
13. Campbell, L. A., Chu, R. C., David, M. P., Ellsworth, M. J., Iyengar, M. K., Simons, R. E., & Singh, P. (2014). *U.S. Patent No. 8,806,749*. Washington, DC: U.S. Patent and Trademark Office.
14. Carey V.P., (1992), "Liquid-Vapor Phase Change Phenomena", London, Taylor and Francis.
15. Barber, J., Brutin, D., & Tadrist, L. (2011). A review on boiling heat transfer enhancement with nanofluids. *Nanoscale research letters*, *6*(1), 280.
16. Phan, H. T., Caney, N., Marty, P., Colasson, S., & Gavillet, J. (2009). Surface wettability control by nanocoating: the effects on pool-boiling heat transfer and nucleation mechanism. *International Journal of Heat and Mass Transfer*, *52*(23-24), 5459-5471.
17. Sakashita, H., & Ono, A. (2009). Boiling behaviors and critical heat flux on a horizontal plate in saturated pool-boiling of water at high-pressures. *International Journal of Heat and Mass Transfer*, *52*(3-4), 744-750.
18. Garimella, S. V., Persoons, T., Weibel, J. A., & Gektin, V. (2016). Electronics thermal management in information and communications technologies: Challenges and future directions. *IEEE Transactions on Components, Packaging and Manufacturing Technology*, *7*(8), 1191-1205.

19. Bergles, A. E. (2002). ExHFT for fourth generation heat transfer technology. *Experimental Thermal and Fluid Science*, *26*(2-4), 335-344.

20. Bergles, A. E. (1999). Enhanced heat transfer: endless frontier, or mature and routine. *Journal of Enhanced Heat Transfer*, *6*(2-4).

21. M. Kang, Effect of surface roughness on pool-boiling heat transfer, Int. J. Heat Mass Transfer. 43 (2000) 4073-4085.

22. Jones B.J, McHale JP, Garimella SV, The influence of surface roughness on nucleate pool-boiling heat transfer, ASME. J. Heat Transfer. (2009); 131(12).

23. H. Jo, S. Kim, H. Kim, J. Kim, M.H. Kim, Nucleate boiling performance on nano/microstructures with different wetting surfaces, Nanoscale research letters. 7 (2012) 242.

24. A. Das, P. Das, P. Saha, Performance of different structured surfaces in nucleate pool-boiling, Appl. Therm. Eng. 29 (2009) 3643-3653.

25. K. Chu, R. Enright, E.N. Wang, Structured surfaces for enhanced pool-boiling heat transfer, Appl. Phys. Lett. 100 (2012) 241603.

26. C. Marcel, A. Clausse, C. Frankiewicz, A. Betz, D. Attinger, Numerical investigation into the effect of surface wettability in pool-boiling heat transfer with a stochastic-automata model, Int. J. Heat Mass Transfer. 111 (2017) 657-665.

27. A.R. Betz, J. Jenkins, C. Kim, D. Attinger, Boiling heat transfer on superhydrophilic, superhydrophobic, and superbiphilic surfaces, International Journal of Heat and Mass Transfer. 57 (2013) 733-741.

28. A.R. Betz, J. Xu, H. Qiu, D. Attinger, Do surfaces with mixed hydrophilic and hydrophobic areas enhance pool-boiling? Appl. Phys. Lett. 97 (2010) 141909.

29. H. Jo, H.S. Park, M.H. Kim, Single bubble dynamics on hydrophobic–hydrophilic mixed surfaces, International Journal of Heat and Mass Transfer. 93 (2016) 554-565.
30. Y. Nam, Y.S. Ju, Bubble nucleation on hydrophobic islands provides evidence to anomalously high contact angles of nanobubbles, Appl. Phys. Lett. 93 (2008) 103115.
31. Y. Takata, S. Hidaka, M. Kohno, Enhanced nucleate boiling by superhydrophobic coating with checkered and spotted patterns, (2006) 240-244.
32. Y. Takata, S. Hidaka, M. Masuda, T. Ito, Pool-boiling on a superhydrophilic surface, Int. J. Energy Res. 27 (2003) 111-119.
33. V. Trisaksri, S. Wongwises, Nucleate pool-boiling heat transfer of TiO2–R141b nanofluids, International Journal of Heat and Mass Transfer. 52 (2009) 1582-1588.
34. H.T. Phan, N. Caney, P. Marty, S. Colasson, J. Gavillet, Surface wettability control by nanocoating: The effects on pool-boiling heat transfer and nucleation mechanism, International Journal of Heat and Mass Transfer. 52 (2009) 5459-5471.
35. Y. Nasersharifi, M. Kaviany, G. Hwang, Pool-boiling enhancement using multilevel modulated wick, Appl. Therm. Eng. 137 (2018) 268-276.
36. K. Rainey, S. You, S. Lee, Effect of pressure, subcooling, and dissolved gas on pool-boiling heat transfer from microporous surfaces in FC-72, Journal of Heat Transfer. 125 (2003) 75-83.
37. Wei, J. J., & Honda, H. Effects of fin geometry on boiling heat transfer from silicon chips with micro-pin-fins immersed in FC-72. *International journal of heat and mass transfer*, *46*(21) (2003), 4059-4070.

38. Rahman, M. M., Olceroglu, E., and McCarthy, M., 2014, "Role of Wickability on the Critical Heat Flux of Structured Superhydrophilic Surfaces," Langmuir : The ACS Journal of Surfaces and Colloids, **30**(37) pp. 11225-11234.

39. N. Li, A.R. Betz, Boiling Performance of Graphene Oxide Coated Copper Surfaces at High-pressures, Journal of Heat Transfer. 139 (2017) 111504.

40. H. Sakashita, Bubble growth rates and nucleation site densities in saturated pool-boiling of water at high-pressures, J Nucl Sci Technol. 48 (2011) 734-743.

41. G.H. Seo, G. Jeun, S.J. Kim, Pool-boiling heat transfer characteristics of zircaloy and SiC claddings in deionized water at low pressure, Exp. Therm. Fluid Sci. 64 (2015) 42-53.

42. F. Giraud, R. Rullière, C. Toublanc, M. Clausse, J. Bonjour, Subatmospheric pressure boiling on a single nucleation site in narrow vertical spaces, Int J Heat Fluid Flow. 58 (2016) 1-10.

43. W.R. McGillis, V.P. Carey, J.S. Fitch, W.R. Hamburgen, Pool-boiling enhancement techniques for water at low pressure, (1991) 64-72.

44. M.T. Cichelli, C.F. Bonilla, Heat transfer to liquids boiling under pressure, Transactions of the American Institute of Chemical Engineers. 41 (1945) 755-787.

45. Semeria, R. (1963). High-speed cinematography and pool-boiling under high-pressure. *La Houlle Blanche*, *6*, 679-687.

46. Bobrovich, G. I., & Mamontova, N. N. (1965). A study of the mechanism of nucleate boiling at high heat fluxes. *International Journal of Heat and Mass Transfer*, *8*(11), 1421-1424.

47. Nishikawa, K., Fujita, Y., Nawata, Y., & Hirahaya, K. (1970). Effect of pressure on nucleate boiling heat transfer of water. *Mem. Fac. Eng. Kyushu Univ*, *30*(2), 27-49.

48. Thome, J. R. (1990). *Enhanced boiling heat transfer* (No. BOOK). Hemisphere Pub. Corp.(Taylor & Francis).

49. Webb, R., & Wilson, A. D. (1993). L., 1994,". *Principles of enhanced heat transfer," John Wiley & Sons, New York*.

50. Nasersharifi, Y., Kaviany, M., & Hwang, G. (2018). Pool-boiling enhancement using multilevel modulated wick. *Applied Thermal Engineering*, *137*, 268-276.

51. Hwang, G. S., & Kaviany, M. (2006). Critical heat flux in thin, uniform particle coatings. *International journal of heat and mass transfer*, *49*(5-6), 844-849.

52. Jafari, D., Wits, W. W., & Geurts, B. J. (2018). Metal 3D-printed wick structures for heat pipe application: Capillary performance analysis. *Applied thermal engineering*, *143*, 403-414.

53. Kandlikar, S. G. (2013). Controlling bubble motion over heated surface through evaporation momentum force to enhance pool-boiling heat transfer. *Applied Physics Letters*, *102*(5), 051611.

54. Chang, J. Y., & You, S. M. (1997). Enhanced boiling heat transfer from microporous surfaces: effects of a coating composition and method. *International Journal of Heat and Mass Transfer*, *40*(18), 4449-4460.

55. Kim, J. H., Rainey, K. N., You, S. M., & Pak, J. Y. (2002). Mechanism of nucleate boiling heat transfer enhancement from microporous surfaces in saturated FC-72. *J. Heat Transfer*, *124*(3), 500-506.

56. N. Zuber, Hydrodynamic aspects of boiling heat transfer (thesis). (1959).

57. Byon, C., Choi, S., & Kim, S. J. (2013). Critical heat flux of bi-porous sintered copper coatings in FC-72. *International Journal of Heat and Mass Transfer*, *65*, 655-661.

58. Liter, S. G., & Kaviany, M. (2001). Pool-boiling CHF enhancement by modulated porous-layer coating: theory and experiment. *International Journal of Heat and Mass Transfer*, *44*(22), 4287-4311.

59. Polezhaev, Y. V. (1990). Modelling heat transfer with boiling on porous structures. *Thermal engineering*, *37*(12), 617-620.

60. Hsu.Y.Y. (1962) "On the size range of active nucleation cavities on a heating surface", Journal of heat transfer, 207-213.

61. W. Fritz, Maximum volume of vapor bubbles, PhysikZeitschr. 36 (1935) 379-384.

62. Mikic. B.B and Rohsenow W.M., (1969), "A new correlation of pool-boiling data including the effect of heating surface characteristics." Trans. ASME J. eat Mass Trans., 91:245-250.

63. Forster, K., and Grief. R. (1958), "Heat transfer to a boiling liquid mechanism and correlations", Progress report No.7, 58-70

64. Dahariya, Smreeti and Amy Rachel Betz. 2019. High-pressure pool-boiling: Mechanism for heat transfer enhancement and comparison to existing models. *International Journal of Heat and Mass Transfer* 141 (2019) 696 - 706.

65. D. Labuntsov, Study of the growth of bubbles during boiling of saturated water within a wide range of pressures by means of high-speed moving pictures, Teplofizika Vysokikh Temperatur. 2 (1964) 446-453.

66. G. Bobrovich, N. Mamontova, A study of the mechanism of nucleate boiling at high heat fluxes, Int. J. Heat Mass Transfer. 8 (1965) 1421-1424.

67. C. Guan, J.F. Klausner, R. Mei, A new mechanistic model for pool-boiling CHF on horizontal surfaces, International Journal of Heat and Mass Transfer. 54 (2011) 3960-3969.

68. D. Foster, Heat transfer to a boiling liquid-mechanism and correlation, Journal of Heat Transfer. 81 (1959) 43-53.

69. K. Stephan, M. Abdelsalam, Heat-transfer correlations for natural convection boiling, International Journal of Heat and Mass Transfer. 23 (1980) 73-87.

70. W.M. Rohsenow, A method of correlating heat transfer data for surface boiling of liquids. (1951).

71. V. Dhir, S. Liaw, Framework for a unified model for nucleate and transition pool-boiling, Journal of heat transfer. 111 (1989) 739-746.

72. S.G. Kandlikar, A theoretical model to predict pool-boiling CHF incorporating effects of contact angle and orientation, Journal of Heat Transfer. 123 (2001) 1071-1079.

73. Nanxi Li. High-pressure pool-boiling and physical insight of engineered surfaces. Thesis-(2017)

74. Dahariya, S., Pai, A. J., Hwang, G., & Betz, A. R. (2019). POOL-BOILING HEAT TRANSFER ENHANCEMENT USING SINTERED PARTICLE WICK STRUCTURE. In *ASTFE Digital Library*. Begel House Inc..

75. Sarangi, S., Weibel, J. A., & Garimella, S. V. (2015). Effect of particle size on surface-coating enhancement of pool-boiling heat transfer. *International Journal of Heat and Mass Transfer*, *81*, 103-113.

76. Liter, S. G. (2000). *Pool-boiling enhancement and liquid choking limits within and above a modulated porous-layer coating* (Doctoral dissertation).

77. Chang, J. Y., & You, S. M. (1997). Boiling heat transfer phenomena from microporous and porous surfaces in saturated FC-72. *International Journal of Heat and Mass Transfer*, *40*(18), 4437-4447.

78. Semenic, T., Lin, Y. Y., Catton, I., & Sarraf, D. B. (2008). Use of biporous wicks to remove high heat fluxes. *Applied Thermal Engineering*, *28*(4), 278-283.

79. Hu, H., Weibel, J. A., & Garimella, S. V. (2019). A coupled wicking and evaporation model for prediction of pool-boiling critical heat flux on structured surfaces. *International Journal of Heat and Mass Transfer*, *136*, 373-382.

List of Publications

1. **Dahariya S**, Patel N, Egbo M K, Hwang G, Betz A R (2019), "The effect of the particles size on the pool-boiling heat transfer enhancement " Advanced Physics Letter - (**in progress**)
2. **Dahariya S**, Patel N, Egbo M K, Hwang G, Betz A R (2019), "High-pressure pool-boiling heat transfer enhancement mechanism on sintered-particle wick" Frontiers of Mechanical Engineering - (**revision requested**)
3. **Dahariya S** and Betz A. R.(2019), Pool-boiling heat transfer enhancement using sintered particle wick structure, *ASTFE 2019 4th Thermal and Fluids Engineering Conference Las-Vegas* TFEC – 2019-27387 **- (published**).
4. **Dahariya S** and Betz A. R. (2019), An analytical model to determine the maximum allowable point source heating with minimal risk to phase-change of liquids in brain tissue , *ASTFE 2019 4th Thermal and Fluids Engineering Conference Las-Vegas* TFEC – 2019-27388 **- (published**).
5. **Dahariya S** and Betz A. R. (2019), High-pressure pool-boiling: Mechanisms for heat transfer enhancement & comparison to existing models, *International Journal of Heat and Mass Transfer (IJHMT)* DOI:141 (2019) 696–706697- (**published**).
6. **Dahariya S**, Betz A (2018), Theoretical and experimental analysis of increasing pressure during pool-boiling. ASME. International Conference on Nanochannels, Microchannels, and Minichannels*, ASME 2018 16th International Conference on Nanochannels, Microchannels, and Minichannels.* - DOI:10.1115/ICNMM2018-7673. - (**published**)
7. **Dahariya S** and Betz A. R.(2017), A theoretical model for the design of biphilic surfaces, *ASTFE 2017 2nd Thermal and Fluids Engineering Conference, Las-Vegas,USA*, ISSN 2379-1748.- (**published**)